EXPERIMENTAL INVESTIGATION ON SEISMIC PERFORMANCE OF UNREINFORCED MASONRY WALLS STRENGTHENED WITH LIGHTWEIGHT ENGINEERED CEMENTITIOUS COMPOSITES

Chukwuwike Mike Ogwumeh, B. Eng

Submitted in fulfillment of the requirements
for the degree of Master of Science
in Civil Engineering & Environmental Engineering

School of Engineering and Digital Sciences
Department of Civil & Environmental Engineering
Nazarbayev University

53 Kabanbay Batyr Avenue,
Astana, Kazakhstan, 010000

Supervisors: Jong Kim**,** Dichuan Zhang

April 2023

DECLARATION

I hereby declare that this manuscript, entitled "**Experimental Investigation on Seismic Performance of Unreinforced Masonry Walls Strengthened with Lightweight Engineered Cementitious Composites**," is the result of my work except for quotations and citations which have been duly acknowledged.

I also declare that, to the best of my knowledge and belief, it has not been previously or concurrently submitted, in whole or in part, for any other degree or diploma at Nazarbayev University or any other national or international institution.

(Signature of the author)

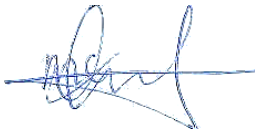

Name: Chukwuwike Mike Ogwumeh

Date: April 07, 2023

Abstract

Historically, Masonry buildings are known to be one of the most seismically vulnerable structures due to their low capacity to resist tensile stresses and lateral loads developed during seismic activity. Over two thousand non-earthquake-resistant masonry buildings were widely built in the Almaty region – Kazakhstan's most seismically dangerous area between the 1950s to 1980s. The Almaty region is known to have a long seismic cycle, indicating that stress repeatedly builds up over a long period and has a high potential for a rapid release of a hazardous earthquake in the future. Thus, the development of effective techniques such as retrofitting masonry structures with the application of engineered cementitious composites to improve the seismic performance of such buildings is essential.

Engineered cementitious composites (ECC) have been studied more for structural retrofitting applications, such as seismic retrofitting on unreinforced masonry (URM) walls because they exhibit a ductility strain hardening response under tension in contrast to conventional concrete. Literature shows that using normal-weight designed cementitious composite can greatly increase masonry walls' strength against cyclic in-plane horizontal loads. However, it has limited improvement in the deformation capacity and ductility of the wall, which is an important criterion for seismic resistance. This restriction might be due to the incompatibility between the wall and the composite in terms of strength and stiffness. It is suggested that lightweight engineered cementitious composites (LWECC), which have lower strength and stiffness and are more compatible with brick walls, can address the restriction.

To investigate the seismic performance of the URM walls retrofitted with LWECC through an experimental study, three URM walls with an aspect ratio of 0.55 were tested under cyclic in-plane loadings. The walls were chosen as 1/3 of an interior prototype load-bearing wall segment of a typical old non-earthquake-resistant four-story residential URM clay brick building found in Almaty region, Kazakhstan built between the year, 1957 to 1967. One wall was a URM wall without any form of retrofit as a reference specimen and the other two walls were retrofitted by troweling 15 mm thick layers of LWECC on both faces of the wall. The composites were chosen to have two different compressive strengths of 27.10 MPa and 11.13 MPa respectively, exhibiting tensile strength and tensile strain capacities of 3.75 MPa (1.48%) and 2.63 MPa (1.80%)

respectively. In-plane wall testing was conducted by applying a constant gravity load of 248 kN to induce an average compressive stress (σ_0) of 0.51 MPa, maintained to represent the axial stress on the prototype wall with 3-story wall load above then increasing cyclic lateral loads applied to the top left end of the wall until failure or 15% strength reduction was observed. The test walls were instrumented with five linear variable differential transformers (LVDTs) and four string potentiometers to measure the horizontal top displacements, all deformations, uplifts, and crack propagations experienced by each wall specimen.

Results from the in-plane wall testing showed that retrofitting the URM walls with the lightweight composites, although exhibiting a limited increase in the lateral load-resistant capacity of the walls by average values of 7.21% for 27.10 MPa LWECC retrofitted wall and 10.14% for 11.13 MPa LWECC retrofitted wall, there were significant improvements in the ultimate displacement and wall ductility capacities. Retrofitting of the wall with 24.10 MPa LWECC caused an average increase of 58.44% and 151.91% in the ultimate displacement and wall ductility capacities respectively and retrofitting of the wall with 11.13 MPa LWECC caused an average increase of 122.78% and 151.18% in the ultimate displacement and wall ductility capacities respectively.

The findings show that this retrofitting method can significantly increase the ductility and displacement capacity of unreinforced masonry (URM) walls, resulting in a change from brittle failure to a more ductile mode of failure while maintaining wall integrity under significant lateral deformations. Furthermore, it was deduced that the usage of a lighter composite material produces improved ductility, hence boosting the efficiency of the strengthening strategy. In particular, the lightweight composite material's improved ductility significantly raises brick walls' ductility and displacement capacity.

Acknowledgments

Foremost, I am grateful to the “Almighty God” for seeing me through this research and my masters’ study.

I would like to express my sincere gratitude to my advisors, Professor Jong R. Kim, and Associate Professor Dichuan Zhang for their continuous support, guidance, the impartation of immense knowledge, and patience throughout the research.

My sincere thanks also go to Zhanbolat and every member of my research team for helping with most laboratory work, especially in the construction of the walls, working most times at night on the weekends.

I also take the opportunity to express a deep sense of gratitude to my family for their constant support, words of encouragement, and prayers.

In conclusion, a special thank you to my lovely girlfriend Elizabeth, my close friends, and my classmates. Having great people who are success driven and optimistic, is a big motivation for me. You guys are the best! My wish is for us to become great and prominent individuals in the future.

This research was supported by the Nazarbayev University Research Fund under the Grant “Development of Lightweight Engineered Cementitious Composites for Multifunctional Seismic Retrofitting on Unreinforced Masonry Structures Using Industry Byproducts” (SEDS2021021). The author is grateful for this support. Any opinions, findings, conclusions, and/or recommendations expressed in this material are those of the author and do not necessarily reflect the views of Nazarbayev University.

Table Of Contents

Abstract ……..…….…… 2

Acknowledgments 4

Table Of Contents 5

List of Abbreviations & Symbols..... 7

List Of Figures …….. 9

List Of Tables …… 11

Chapter 1: Introduction 12

1.1 Overview 12

1.2 Masonry Structures under Seismic Load 13

1.3 Research Hypothesis 15

1.4 Purpose of the Project 15

1.5 Structure of the Thesis 15

Chapter 2: Literature Review 17

2.1 Experimentally Established Behavior of URM Walls 17

2.2 In-Plane Failures of Masonry Walls 18

2.3 Engineered Cementitious Composites 20

2.4 Lightweight Engineered Cementitious Composites 20

Chapter 3: Experimental Program 22

3.1 Testing Specimen 22

3.2 URM Wall Design Considerations and Scaling 22

3.3 Test setup and loading procedure 25

3.4 Material Properties 28

3.4.1 Brick Units 28

3.4.2 Mortar 30

3.2.3 Lightweight Engineered Cementitious Composite (LWECC) 32

3.5 Wall Instrumentation 39

Chapter 4: Results and Discussions 40

4.1 Force-displacement response 40

4.2 Displacement ductility capacity 47

4.3 Failure mode and damage development 48

4.4 Flexural failure 56

4.5 Shear deformation 62

4.6 Stiffness Degradation 63

4.7 Energy dissipation capacity 65

Chapter 5: Conclusions and Recommendations 67

5.1 Conclusions 67

5.2 Recommendations for further research 69

Bibliography/References 70

Appendices 74

Appendix A 74

List of Abbreviations & Symbols

URM	Unreinforced Masonry
ECC	Engineered Cementitious Composites
LWECC	Lightweight Engineered Cementitious Composites
LVDT	Linear Variable Differential Transformers
TRM	Textile-reinforced Mortar
FRP	Fiber Reinforced Polymer
FEMA	Federal Emergency Management Agency
URW	Unreinforced Wall Specimen
RW-1	Reinforced Wall Specimen 1
RW-2	Reinforced Wall Specimen 2
RPC	Reactive Powder Concrete
OPC	Ordinary Portland Cement
S15	Glass Micro-hollow Bubble
HPMC	Hydroxypropyl Methylcellulose
PVA	Polyvinyl Alcohol
σ_0	Average compressive stress
v_{me}	Sliding shear strength of the bed joint
A_n	Net-area of wall mortared section
f_{dt}	Lower bound of masonry diagonal tension strength
β	Shear stiffness reduction factor
f_a	Upper bound of vertical axial compressive stress
P	Anticipated vertical axial compressive force for each load combination
l_w	Wall's length
h_w	Wall's height
t_w	Wall's thickness

f_m	Lower bound of the masonry wall compressive strength
f_b	Compressive strength of the brick units
A	Surface area of the brick
$f_{c\ mortar}$	Mean compressive strength of the mortar cubes
$f_{c\ LWECC}$	Average compressive strength of LWECC specimens
F_{max}	Maximum lateral force
F_u	Wall's ultimate shear resistance
Δ_u	Ultimate displacement capacity
δ_u	Ultimate drift capacity
k_e	Effective stiffness
μ	Displacement ductility
M_R	Moment resistance
θ	Wall and toe rotations
U	Wall uplift
τ	Shear stress
${\gamma_i}^2$	Shear strain
k_{s_i}	Secant stiffness at each loading cycle

List Of Figures

Figure 1.1: Typical failure mechanisms of URM structure ……..…….…… 14

Figure 2.1: Typical failure mechanisms of URM walls subjected to in-plane load: (a) Shear sliding failure, (b) Shear diagonal failure, (c) Flexural failure ……..…… 19

Figure 3.1: Floor plan of prototype building ……..…… 23

Figure 3.2: Pattern of wall construction …… 24

Figure 3.3: Pictures showing the process of applying LWECC retrofit layers over wall specimens ……...……... 24

Figure 3.4: Dimensions of wall specimens: (a) Un-retrofitted masonry wall (URW); (b) RF-1 LWECC retrofitted wall (RW-1); (c) RF-5 LWECC retrofitted wall (RW-2) ……..…. 25

Figure 3.4: Setup for In-plane cyclic load Test ……..… 26

Figure 3.5: Photo of the test set-up ……... 26

Figure 3.6: Loading Protocol …… 27

Figure 3.7: Displacement time history for wall specimens: (a) URW; (b) RW-1; (C) RW-2 ….. 28

Figure 3.8: Compression test conducted on brick units ……..… 29

Figure 3.9: Pictures showing the compressive strength test conducted on mortar samples ….…. 30

Figure 3.10: Average compressive strength fc mortar of mortar on day of wall testing ……..…. 31

Figure 3.11: Sand gradation …….. 32

Figure 3.12: Schematic diagram of dog-bone samples …….. 35

Figure 3.13: Dog-bone samples cast during retrofitting of wall specimens …….……. 35

Figure 3.14: Cylinder samples cast during retrofitting of wall specimens …… 35

Figure 3.15: LWECC uniaxial compressive strength testing …… 36

Figure 3.16: Compression Stress-Strain curves for Cylinder samples: (a) RF-1; (b) RF-5 …….. 36

Figure 3.17: Direct tensile strength testing on dog-bone samples ……..…….. 37

Figure 3.18: Tension Stress-Strain curves for dog-bone samples: (a) RF-1; (b) RF-5 ……..… 38

Figure 3.19(a): Properties of LWECC: (a) Density; (b) Compressive strength …… 38

Figure 3.19(b): Properties of LWECC: (a) tensile strength; (b) Strain Capacity ……..… 38

Figure 3.20: Instrumentation setup for wall specimens before conducting of wall test ……..... 39

Figure 4.1: Hysteretic curves of the wall specimens: (a) URW; (b) RW-1; (c) RW-2 ……. 41

Figure 4.2: URW hysteresis loop stages ……..... 42

Figure 4.3: RW-1 hysteresis loop stages ……... 43

Figure 4.4: RW-2 hysteresis loop stages ……...… 45

Figure 4.5: (a) Backbone curve of wall specimens; (b) Idealization of backbone curve …….. 46

Figure 4.6: Failure mode of URW ……. 49

Figure 4.7: Damage progression for URW specimen ……...……. 50

Figure 4.8: Failure mode of RW-1 ……...……. 52

Figure 4.9: Failure mode of RW-2 ……...……. 52

Figure 4.10: Damage progression for RW-1 specimen …….…… 53

Figure 4.11: Damage progression for RW-2 specimen ……...….. 54

Figure 4.12: Wall uplifts-time graphs of wall specimens: (a) URW; (b) RW-1; (c) RW-2 …… 57

Figure 4.13: Toes uplifts-time graphs of wall specimens: (a) URW; (b) RW-1; (c) RW-2 …… 59

Figure 4.14: Moment vs. rotation graphs for wall specimens: (a) URW; (b) RW-1; (c) RW-2 . 60

Figure 4.15: Displacement vs. rotation graphs for specimens: (a) URW; (b) RW-1; (c) RW-2 . 61

Figure 4.16: Shear stress vs. shear deformation graph: (a) URW; (b) RW-1; (c) RW-2 ……..… 63

Figure 4.17: (a) Stiffness curves of wall specimens; (b) Relative secant stiffness curves of wall specimens ……..… 64

Figure 4.18: (a) Schematic diagram on the determination of dissipated energy; (b) Cumulative energy dissipation curves of wall specimens ……. 66

List Of Tables

Table 3.1: Testing program ……..….. 22

Table 3.2: Loading Sequence …… 27

Table 3.3: Compressive strength of clay bricks ……..… 29

Table 3.4: Average compressive strength of mortar for wall layers …….. 31

Table 3.5: Mix proportions of LWECC ……..… 32

Table 3.6: Properties of S15 ……..……. 33

Table 3.7: Properties of PVA fiber …… 33

Table 3.8: Summary of materials properties for LWECC ……..…… 34

Table 3.9: Summary of LWECC mixing process …….. 34

Table 4.1: In-plane wall responses parameters for wall specimens ……...… 48

Chapter 1: Introduction

1.1 Overview

Masonry is a heterogeneous composite material composed of brick elements held together by mortar. Before the advent of more modern building materials such as concrete and steel, masonry was the principal building material [1]. Most structures built before the 19th century and still surviving are built with masonry [2]. Unreinforced masonry (URM) construction is a prominent building technique preferred all around the world. Since the majority of ancient and historical buildings were load-bearing constructions, reconstruction is not a suitable technique due to the large number of buildings created with URM brick walls [3]. Due to narrow spans and obsolete architectural patterns, most of the old brick constructions cannot meet living requirements as the economy develops. Seismic retrofitting is necessary for URM walls either because of the modernization of design codes or because of the magnification impact of masonry walls on floor acceleration or if cracking and minimal damage have occurred because of prior seismic activities [4]. As reported by S. M. Renuka et. al., this stresses the need for the evaluation of relevant structural measures for strengthening these structures [5]. To reinforce the masonry constructions, the reinforcing material should have a sufficient tensile capacity to resist extreme loads.

A significant number of inquiries have been conducted in the past few decades to discover strengthening procedures that will increase masonry performance to improve their seismic performance. To improve the seismic resistance of a building, a fundamental goal is to enhance the in-plane response of structural elements such as masonry walls, because these structural elements are often vital for maintaining structural reliability [6].

Several externally bonded overlay materials such as textile-reinforced mortar (TRM) have been used to retrofit brick URM wall components [7], [8] and masonry wallettes [9] to enhance the in-plane seismic performance of URM walls. Different retrofit techniques such as the installation of new structural elements, external post-tensioning, steel bracing, steel plate bonding, Fiber Reinforced Polymer (FRP) sheets [10]–[12], shotcrete [13], Engineered Cementitious Composite (ECC), and many more have been utilized with some degree of effectiveness to boost the performance of URM walls. However, ECC has proven to possess superior thermal characteristics as compared to other materials [10].

ECC shotcrete, a cement composite filled with synthetic fiber is another form of retrofitting technology that is applied by spraying the composite with pressure. When strained in tension, the composite exhibits a strain-hardening property through the development of numerous microcracks connected by stresses conveyed by various types of fibers linking the microcracks. ECC stands as the best material for seismic retrofitting due to its strain-hardening property, which increases the ductility and strength of an existing structure [14]. Soleimani-Dashtaki et al. conducted shaking-table tests on URM walls reinforced with spray-able eco-friendly ECC to assess the horizontal load-carrying capacity of the URM walls retrofitted on a single side and both faces of the walls [15]. The findings revealed that retrofitting the wall only on one side is adequate for low-rise buildings to endure significant earthquakes, whereas it is preferable to reinforce the walls on both sides for high-rise buildings sustaining enormous wall loads.

This study focuses on the behavior of URM walls retrofitted on both faces with LWECC. The use of ECC has previously been proven to be effective in enhancing the seismic performance of different masonry walls (such as walls made from cavity fillers such as precast panels or concrete blocks). Though, restricted studies have been conducted on its application on load-bearing masonry walls subjected to lateral loads. The use of normal-weight ECC is proven to significantly improve the shear load strength but limited improvement in the wall's ductility. This could be due to normal-weight ECC possessing higher stiffness than plane masonry walls. Lightweight engineered cementitious composite (LWECC) with multifunctional properties of lightweight, low thermal conductivity, and high sound absorption ability is hypothesized to substantially improve masonry walls' ductility and displacement capacity.

1.2 Masonry Structures under Seismic Load

The use of URM structures can be found in every region of the world, especially in developing countries but they exhibit poor performance to seismic load, causing the loss of numerous lives and properties [16], [17]. Due to this seismic inadequacy, URM structures are most liable to experience serious damage or even collapse in the occurrence of an earthquake [18]. This inadequacy can be attributed to the material characteristics of URM structures, which include low ductility, poor tensile strength, poor shear strength, and poor energy dissipation capacity [17], [18].

The evaluation of masonry structures' safety in seismic regions has recently received significant attention due to its limited resistance to seismic stresses. Earthquakes have regularly shaken Kazakhstan's south and southeast areas as one of the world's greatest natural dangers, and seismic activity within the region can be described as frequent and catastrophic [19]. One-third of the structures in the Almaty region which is located in a high seismic region are URM structures characterized for being susceptible to damage at the occurrence of lateral loads caused by an earthquake, and a significant portion being brick masonry buildings built 30-50 years ago without any form of seismic engineered design and are expected to have brittle response under earthquakes [19]. Consequently, it is critical to enhance the seismic performance of existing masonry constructions to limit damages and eliminate hazards to lives and properties, especially in a densely populated city like Almaty.

When an earthquake occurs, the masonry disintegrates and the floors lose stability, causing the building to collapse. Also, the masonry load-bearing wall's aspect ratio may exhibit double diagonal shear cracking due to severe bending and shearing. The X-shaped diagonal cracking is a typical result of how poorly, URM walls perform under shear, and its new triangular parts might lose stability, causing the walls to collapse. Bearing in mind the tri-dimensional nature of seismic waves, the actual failure of URM walls results from a combination of the two main failure modes of URM walls, in-plane and out-of-plane failure modes which are shown in Figure 1.1 [13]. It has been established that inertia forces parallel to the wall plane are a critical factor in the degradation of the shear strength of URM structures, which results in in-plane damages [20]. As a result, in-plan retrofitting of URM walls must be taken into consideration as a crucial component of a strengthening strategy.

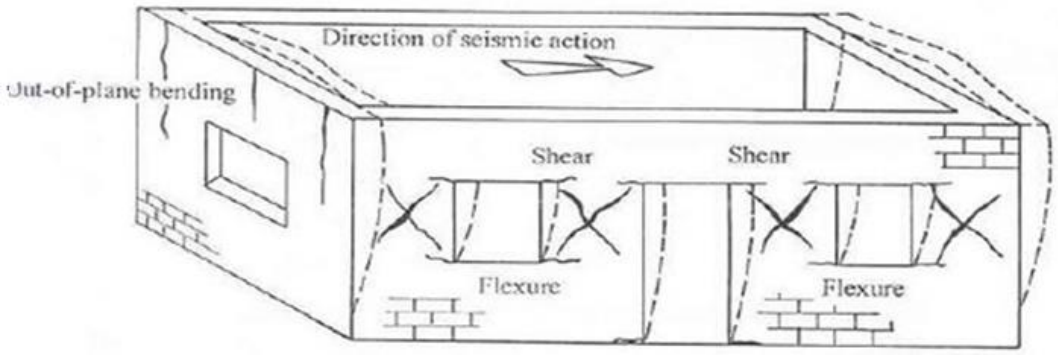

Figure 1.1: Typical failure mechanisms of URM structure

ECC would be a viable choice as a retrofitting material for URM walls. The application of ECC over masonry walls is akin to the plastering of mortar and can endure high temperatures in contrast to other retrofitting materials, such as FRP [21]. ECC is an extremely ductile material with a tensile strain hardening capacity reaching 3%, classifying it as a high-performance cementitious composite with elevated ductility and the capability to bend instead of rupture under extreme tensile loading situations.

1.3 Research Hypothesis

The use of LWECC in retrofitting URM walls is anticipated to improve the wall's seismic performance by enhancing its deformation capacity, lateral strength, and ductility compared to URM walls subjected to seismic activity.

1.4 Purpose of the Project

The major aim of this thesis is to evaluate the seismic behavior of walls made of URM with and without LWECC retrofitting for the enhancement of both the strength and ductility of URM structures. The objectives are to:

- Examine the structural response of URM walls exposed to in-plane cyclic loadings.
- Investigate the structural response of URM walls strengthened with LWECC when subjected to in-plane cyclic loadings.
- Identify the effect of LWECC strength on the effectiveness of seismic strengthening of URM walls.

1.5 Structure of the Thesis

The thesis comprises six chapters. The first chapter introduces the key features of masonry walls and their behavior under seismic load, the need for wall retrofitting, and the purpose, goals, and current gaps that can be studied in this project.

The second chapter provides background information about related topics. First, experimental and analytically based integrated research on strengthening URM walls are briefly described. The in-plane seismic performance of URM walls strengthened through experimental research is incorporated. Lastly, the existing methods of seismic retrofitting of URM walls are

described, highlighting detailed information about ECC materials. The difference between normal-weight and LWECC and the improvements provided by LWECC concludes the chapter.

Chapter three focuses on the main experimental investigation covering the testing program, type and properties of materials used in the construction and retrofitting of wall specimens, the construction and retrofitting of walls specimens, and the large-scale cyclic in-plane wall testing on wall specimens (un-retrofitted masonry wall specimen, URW, and retrofitted wall specimens, RW-1 & RW-2 with different strengths of LWECC).

Chapter four illustrates results obtained within the course of the performance-based experimental investigation and discusses the main findings highlighting the effects of LWECC on the failure modes, shear resistance, stiffness, deformation capacity, and energy dissipation capacity of URM walls.

In Chapter five, conclusions and design suggestions are provided based on the findings of the experimental investigation.

Chapter 2: Literature Review

This chapter reviews several research that considers the effectiveness of incorporating lightweight engineered cementitious materials (LWECC) in strengthening URM walls. Not much research on URM walls strengthened with lightweight engineered cementitious materials has been extensively conducted. This section briefly reviews earlier studies on the retrofitting materials used on masonry walls, the performance of URM walls under in-plane lateral loads, and the modeling and study of URM walls reinforced and unreinforced with retrofitting material.

2.1 Experimentally Established Behavior of URM Walls

A masonry structure is a non-homogeneous composite structure that consists of bricks filled with mortar within their joints. Depending on the brick unit type and in-filled mortar at the joints, both elements have dissimilar strengths and deformation properties. To achieve a proper outcome for load-bearing walls, only the right balance of mortar and brick types can produce effective results. It is noted that a number of factors, including the quality of the construction, the characteristics of the masonry units, and the mortar joints' age and thickness, impact the compressive strength of a masonry wall [22]. The quality of the workmanship has a considerable bearing on the strength value of the brickwork. Experimental research has shown that masonry prisms under uniaxial compression perpendicular to the bed joint produce tri-axial compression stress in the mortar. Under tri-axial compression, mortar behavior depends on confining stresses and mortar type. Maximum crushing stress-strain behavior increases with increasing confining stresses. Also, lower-strength mortars exhibit greater ductility than higher-strength mortars [1].

The behavior of masonry walls exposed to a combination of horizontal and vertical stresses will vary depending on its geometry (aspect ratio), the properties of the elements, wall boundary conditions, and reinforcement if any [23]. Additionally, the behavior is influenced by the level of precompression (the ratio of the working stresses in the wall caused by gravity loads to the compressive strength of the masonry) and the direction of the horizontal loads (in-plane or out-of-plane). Therefore, a variety of failure scenarios could occur.

2.2 In-Plane Failures of Masonry Walls

The major properties that determine the in-plane capacity of a masonry wall are the relative strength of the masonry brick units and the mortar. Numerous circumstances for the in-plane failure of URM walls are attributable to the combined effects of axial load and bending, and the mode of construction; where the type of failure is majorly controlled by the amount of axial load [22], [24].

If the axial stresses on the wall are low with poor-quality mortar, seismic forces may trigger part of the wall to slide along one of the bed joints [25]. According to the quality of mortar and condition of the masonry units, diagonally shaped cracks may either follow the bed and head joints or pass through the masonry units, or they may partially follow both joints and partially pass through the masonry units [23].

The different in-plane failure modes of URM walls exposed to horizontal load are shown in Figure 2.1 and according to FEMA 306 [26], they include:

(a) Shear sliding failure occurs along the head or bed joint because of low nominal loads and/or minimal friction coefficients, which may be a result of inadequate mortar quality.
(b) Shear diagonal failure occurs when the major tensile stresses that arise in the masonry wall due to a combination of vertical and lateral loads exceed the tensile strength of masonry elements and are characterized by rapid strength reduction.
(c) Flexural failure which can be divided into toe crushing involving crushing of the compressed toes of the URM wall and rocking failure involving the uplifting of the wall at one or both of its toes. This occurs when the wall's shear resistance is still sufficient in comparison to the shear demands.

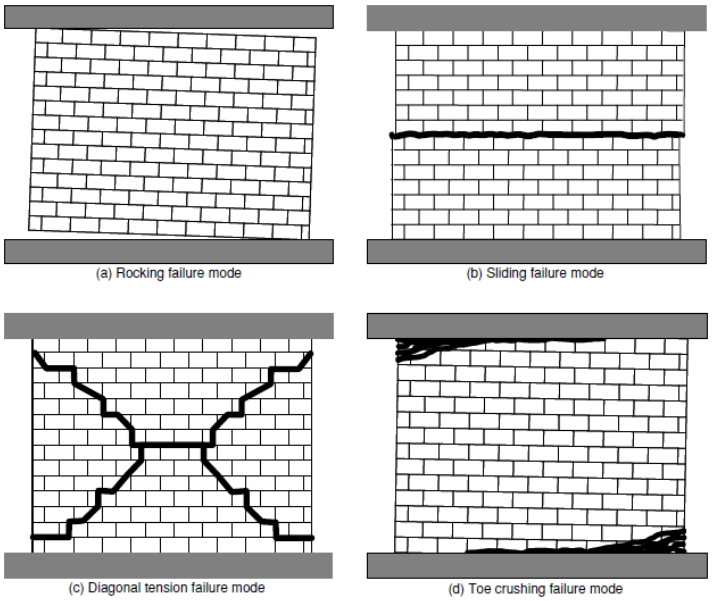

Figure 2.1: Typical failure mechanisms of URM walls subjected to in-plane load: (a) Rocking failure; (b) Shear sliding failure, (c) Shear diagonal failure, (c) Toe-crushing failure

The anticipated lateral strength of URM walls is based on the assumed strength resulting from each of the failure modes in accordance with Equations 1.1-1.4, with the URM wall lateral strength taken as the least of the values given by the four equations [26].

(a) Sliding shear strength (in N): $F_s = \nu_{me} A_n$ (1.1)

(b) Diagonal tension shear strength (in N): $F_{dt} = f_{dt} A_n (\beta) \sqrt{1 + \frac{f_a}{f_{dt}}}$ (1.2)

(c) Toe crushing strength (in N): $F_{tc} = \alpha P \left(\frac{l_w}{h_w}\right)\left(1 - \frac{f_a}{0.7 f_m}\right)$ (1.3)

(d) Rocking strength (in N): $F_r = 0.9 \alpha P \left(\frac{l_w}{h_w}\right)$ (1.4)

Where ν_{me} is the assumed sliding shear strength of the bed joint in MPa; A_n is the net-area of the wall mortared section in mm^2; f_{dt} is the lower bound of the masonry diagonal tension strength in MPa, taken to be $0.05 f_m$; β is taken as 0.67 for $(l_w/h_w) < 0.67$, (l_w/h_w) when $0.67 \leq (l_w/h_w) \leq 1.0$ and 1.0 when $(l_w/h_w) > 1.0$; f_a is the upper bound of the vertical axial compressive stress in MPa; α is taken as 0.5 for a fixed-free cantilever wall or 1.0 for a fixed-fixed wall; P is the anticipated vertical axial compressive force for each load combinations, measured in Newtons; l_w and h_w respectively represent the length and height of the URM wall in mm; and f_m is the lower bound of the masonry wall compressive strength in MPa.

2.3 Engineered Cementitious Composites

ECC is a typical synthetic fiber-reinforced cementitious composite that when under tension exhibits strain-hardening behavior and when subjected to compression, has adequate toughness properties [17]. It is also a highly developed composite material with multiple cracking, high ductility, tensile strength, and self-healing more than standard concrete. Li [27] further defined engineered cementitious composites as specifically designed high-performance fiber-reinforced cementitious composites with substantial tensile ductility and a modest fiber volume percentage (typical 2%).

In recent years, various research is being carried out on ECC as a means of strengthening masonry walls (infill and URM), and this can be attributed to ease in construction with short construction time, low labor sensitivity, and ability to adjust its mixture to achieve a desirable strain hardening tensile property [18], [28]. In general, these mixtures typically contain cement, fly-ash, water, fine aggregate, and, if necessary, superplasticizer and a viscosity modifying agent. Some research has examined the consequences of employing this retrofitting method. The results show that ECCs can significantly improve the behavior of these structures by providing high tensile strength and ductility to the structural element [18]. Research has been done recently that focuses on the use of ECCs in earthquake-resistant URM buildings because of their tensile-strain hardening response and high damage tolerance. Previous experimental research on the seismic performance of a solid clay bricks URM wall with single and doubled-sided ECC retrofit showed an increase in the maximum lateral strength of the wall by 9% and 18% respectively and increase in ductility by 15% and 49% respectively [17]. Another research showed that trowelling ECC coating on both surfaces of double-wythe brick walls increases its maximum lateral strength by 61%-99% but a very low increase in the displacement capacity by just 3.21%-19.00% [18].

2.4 Lightweight Engineered Cementitious Composites

Experimental research on the use of ECC as a means of enhancing seismic performance has been conducted previously using small-scale wallattes, and large-scale masonry wall specimens, investigating the use of normal weight ECC which increases the strength of URM walls but with negligible effect on overall ductility [29]–[31]. High ductility and exceptional crack

control of LWECC coating can enhance the cracking resistance of the structure, therefore enhancing its durability and extending the service life.

Several lightweight technologies have been successfully utilized for the development of LWECC, such as glass micro-hollow bubble [32], [33], air-entrainment admixture [34], [35], nature lightweight perlite [35], presoaked expanded perlite aggregate [36], [37], and fly ash cenospheres [38], [39]. Another study investigating four different lightweight technologies for the LWECC (expanded perlite sand, entrained air, polymeric beads, and hollow glass bubbles) concluded that glass micro-hollow bubbles were most effective, possessing superior tensile strain hardening ratios with reduced unit weight [35].

It has been proven from previous studies that LWECC possesses improved tensile ductility with only a slight reduction in strength capacity. One study by Wang and Li [33] found that LWECC samples exhibit high tensile ductility while retaining desirable compressive and tensile strengths. Another study by Jin and Li [40] showed that by converting large fractures in concrete layer into numerous microcracks in an applied LWECC layer deprived of any delamination, LWECC coating outperforms the monotonic concrete system in terms of ductility. These point to the possibility of using LWECC to enhance the ductile performance of URM walls when subjected to shear stresses, such as those caused by seismic activity. However, its application in the seismic strengthening of masonry walls is yet to be studied.

Chapter 3: Experimental Program

3.1 Testing Specimen

In this experimental program, three masonry wall specimens (URW, RW-1, and RW-2) were fabricated for large-scale In-plane wall testing. URW specimen represented the control wall specimen of a URM wall with no form of retrofit while the other two wall specimens (RW-1 and RW-2) represented masonry walls with 15mm thick LWECC retrofit of different strengths on both surfaces of the walls proposed to enhance the seismic performance of the walls. Table 1 show gives an overview of the experimental program used in conducting the wall testing on the masonry wall specimens. Comparison of RW-1 and RW-2 test results with that of URW aided in the investigation of the influences of the different strengths of LWECC retrofit on the overall seismic performance of URM walls.

Table 3.1: Testing program

Wall Specimens	Specimen dimensions l_w x h_w x t_w (mm)	Strengthening Pattern	Thickness of overlay
URW	2010 x 1100 x 245	Un-strengthened	None
RW-1	2010 x 1100 x 245	*LWECC (RF-1) on both sides	15mm per side
RW-2	2005 x 1090 x 245	*LWECC (RF-5) on both sides	15mm per side

* LWECC = LWECC

3.2 URM Wall Design Considerations and Scaling

For the design of the URM wall, a prototype building was selected to represent a typical non-earthquake-resistant four-story residential masonry building found in Almaty, Kazakhstan built within the year, 1957 to 1967. The wall specimen represents an interior load-bearing URM wall without any openings on the first story of the four-story building wall, build on a solid precast reinforced concrete foundation blocks 500 mm thick and monolithic concrete as found in old URM buildings within the region. The dimensions of the structure and building information were provided by KazNIISA, a Kazakh Research and Design Institute of Construction and Architecture. Figure 1. shows the architectural ground floor plan and the part of the URM wall which was chosen

to be modeled as the wall specimen to be evaluated. To fit within the testing steel frame in the lab, the URM-wall model was reduced to 1/3 of its full scale.

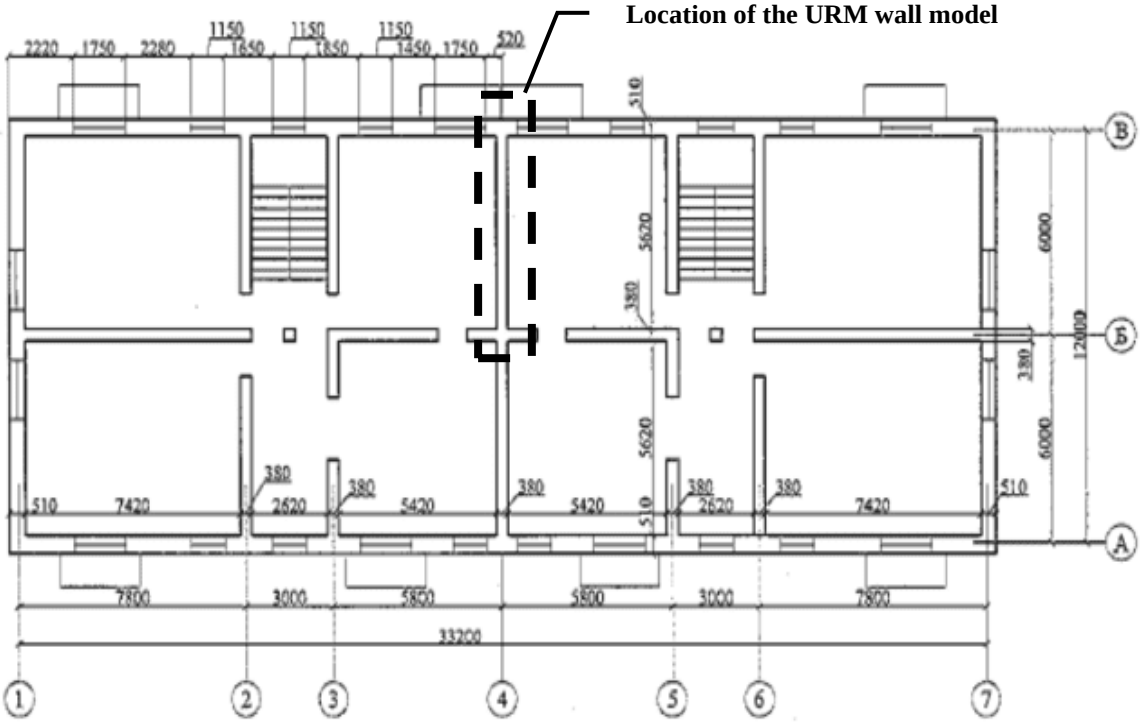

Figure 3.1: Floor plan of prototype building

Three URM specimen walls with target dimensions of 2m length & 1.2m height at 33.33% scale of the original prototype wall (6m length & 3m height) were built in the laboratory on a 700 mm thick reinforced concrete foundation (see Figure 3.5). All specimens were built to have a thickness of 245mm (against 380mm of the original prototype) and assembled in the English bond configuration, generally being used at Almaty from the time of construction of the prototype masonry building (Figure 3.2). The walls were built having a continuous bond with both the bed and head joints filled to have 10 mm mortar thickness. Before conducting the wall testing, all wall specimens were cured for 28 days after all construction processes were completed, including applying LWECC retrofits for retrofitted walls.

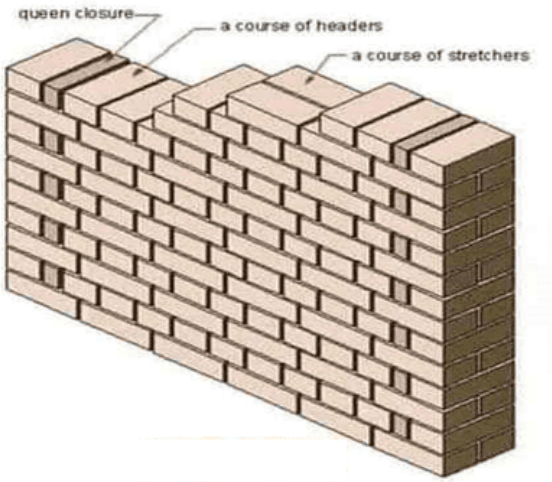

Figure 3.2: Pattern of wall construction

Retrofitting of RW-1 and RW-2 was done using LWECC RF-1 and RF-5, respectively. The LWECC was directly applied on the wall specimens by trowelling the composites on a moistened brick wall face to ensure effective bonding between the wall surfaces and the LWECC, forming 15mm thick layers on both surfaces of the walls (see Figure 3.3). The curing process was done by a daily sprinkling of water on the surface for 28 days leading to testing. Detailed properties of construction materials are presented in Section 3.4.

Figure 3.3: Pictures showing the process of applying LWECC retrofit layers over wall specimens

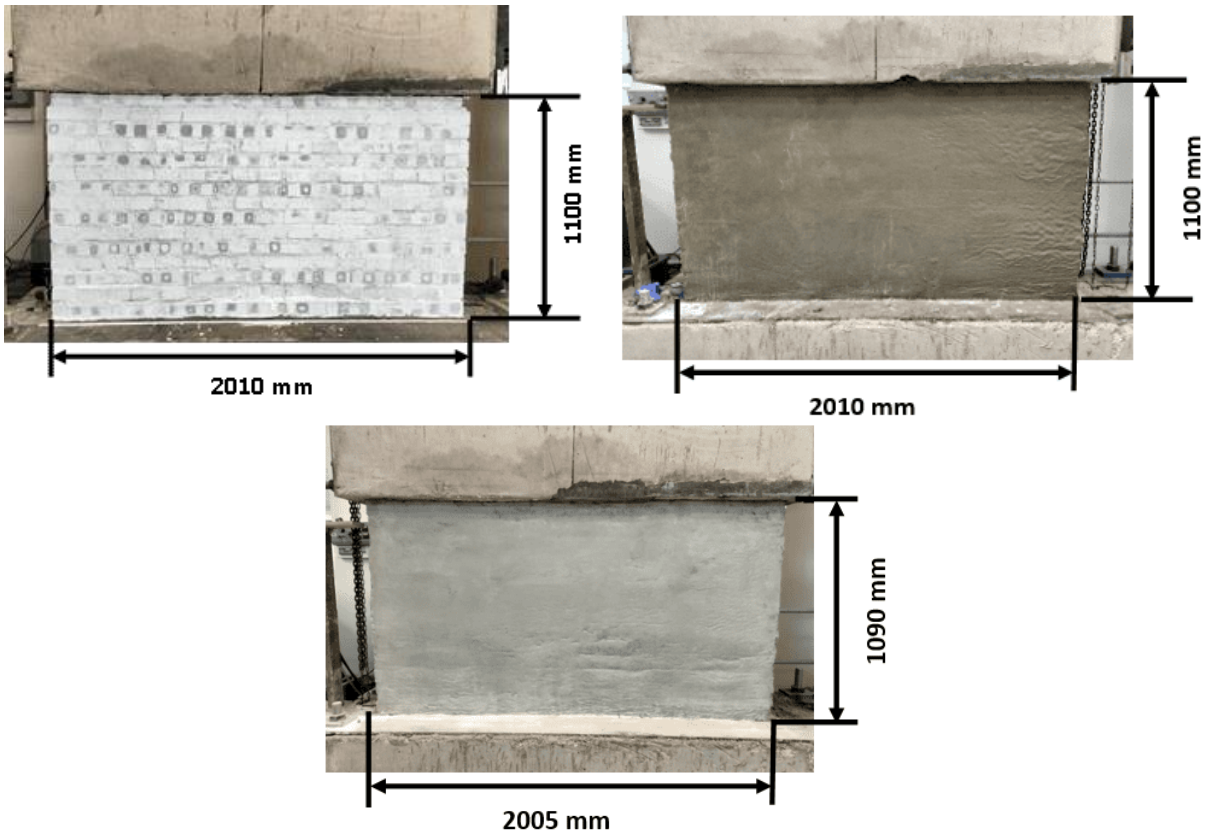

Figure 3.4: Dimensions of wall specimens: (a) Unretrofitted masonry wall (URW); (b) RF-1 LWECC retrofitted wall (RW-1); (c) RF-5 LWECC retrofitted wall (RW-2)

3.3 Test setup and loading procedure

Large-scale In-plane masonry wall testing was carried out on all three wall specimens in the Engineering and Construction Laboratory (block C4) at Nazarbayev University, Astana, Kazakhstan according to the test setup shown in Figure 3.5. The foundation beams for the walls were fastened to the laboratory's strong floor utilizing four high-strength post-tensioned steel bars with high-strength reactive powder concrete (RPC) positioned at the footing level of both sides reacting against small reaction steel frames secured to the solid floor. These RPCs (see Figure 3.5) served as horizontal antiskid, preventing the foundation from sliding during testing.

The test was conducted by applying cyclic lateral loadings to the walls with a total constant vertical load (gravity loads) of 248kN. The vertical electrohydraulic-controlled actuator was utilized in applying a vertical load on each wall specimen to a force of 227kN. The combined weight of the concrete and steel beams placed on the wall is 21 kN. To avoid stress concentration, the steel beam was used to distribute the axial load from the vertical actuator uniformly on the cap

beam with the aid of sand bedding placed between the steel and concrete beams. The influence of friction and any possible out-of-plane movement of the loading beams was minimized by fixing steel rollers in between the vertical actuator and the rigid steel frame. The constant axial load which induced an approximate average compressive stress (σ_0) of 0.51MPa was maintained, representing the axial stress on the prototype wall with 3-story above. Cyclic lateral force was applied to the top left end of the wall through the concrete cap beam by the horizontal electrohydraulic controlled actuator with 1000 kN capacity in pushing and 600 kN capacity in pulling.

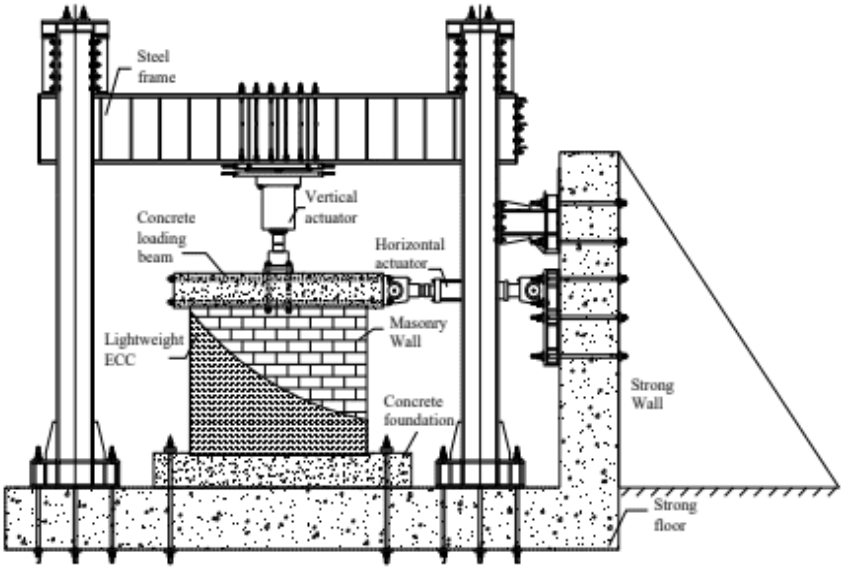

Figure 3.4: Setup for In-plane cyclic load Test

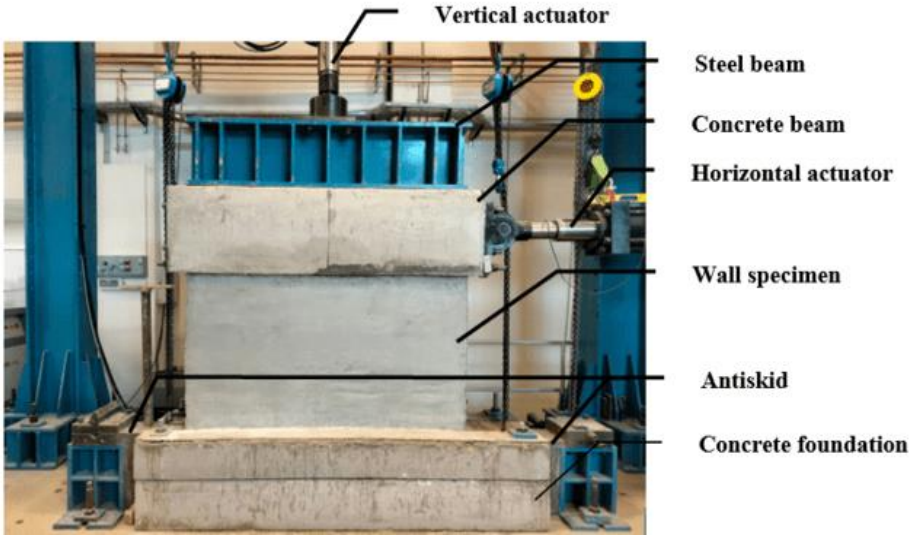

Figure 3.5: Photo of the test set-up

Figure 3.6 shows the cyclic quasi-static loading protocol used in evaluating all specimens. Using the horizontal actuator, the wall specimens were initially subjected to one cycle of lateral load moving under computer load-controlled steps at a loading rate of 1 kN/sec, loaded to 40 kN. The procedure was then switched to computer displacement-controlled steps, subjecting the specimens first to one cycle per displacement step at a loading rate of 1 mm /min up to ±2 mm and three cycles per displacement step at a loading rate of 2 mm /min until failure.

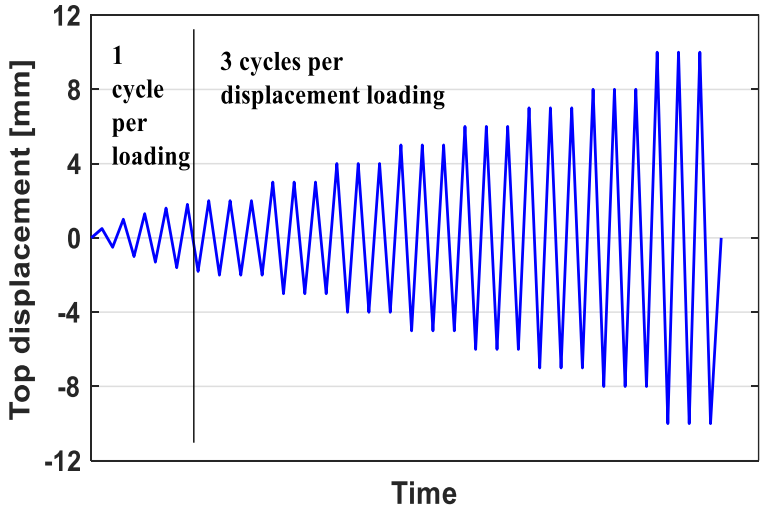

Figure 3.6: Loading Protocol

Table 3.2: Loading Sequence

Pattern	Step	Number of Cycles	Cyclic Displacement (mm)
1	1	1	*40 kN
2	2	1	1
	3	1	1.3
	4	1	1.6
	5	1	1.8
3	6	3	2
	7	3	3
	8	3	4
	9	3	5
	10	3	6
	11	3	7
	12	3	8
		3	Additional increments of 2 mm (until failure)

Figure 3.7 show the displacement time histories of all wall specimens relative to the data points taken for the completion of each cycle, also indicating the pausing periods during the test for the recording of obtained result data.

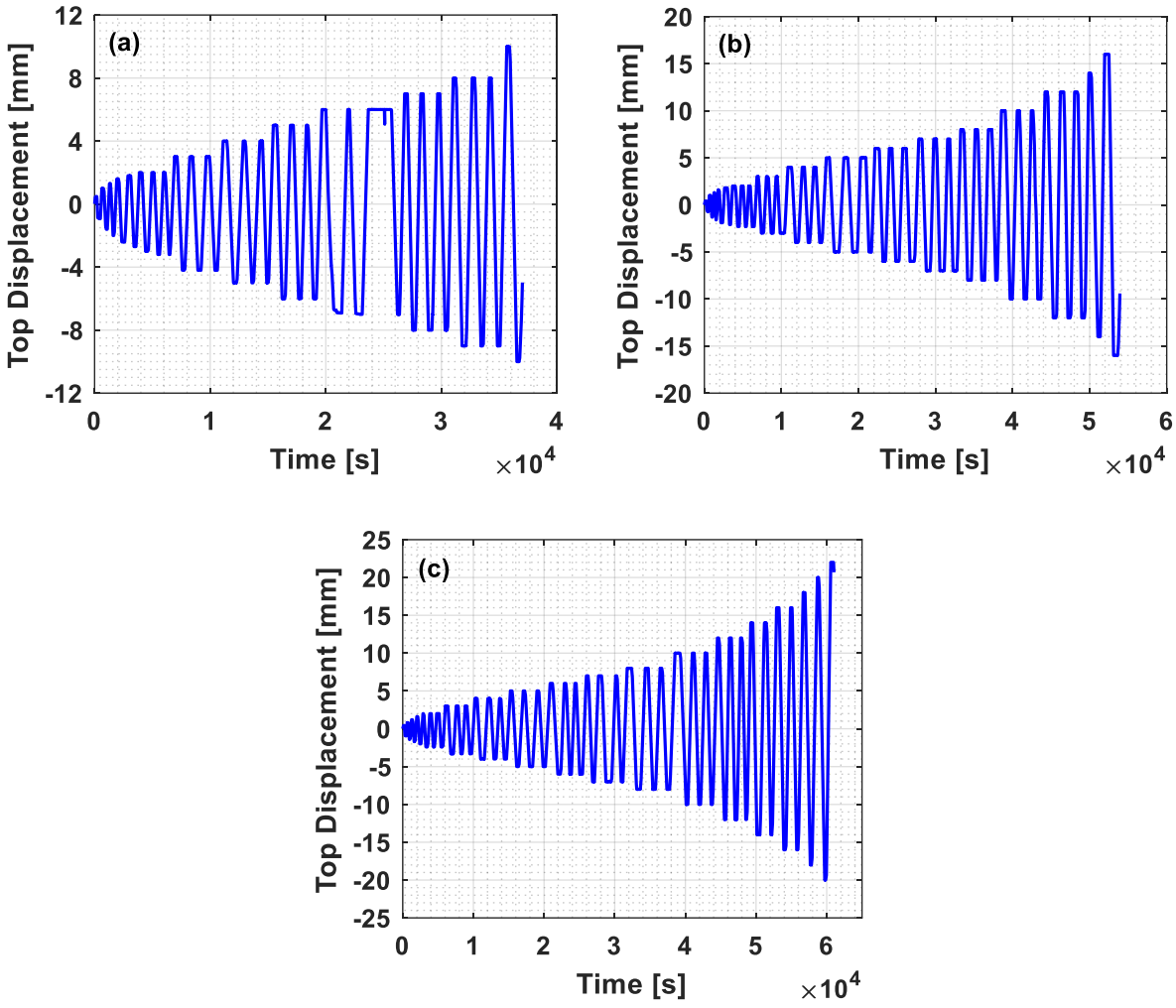

Figure 3.7: Displacement time history for wall specimens: (a) URW; (b) RW-1; (C) RW-2

3.4 Material Properties

3.4.1 Brick Units

According to the Kazakhstan Industry Standard used in the construction of URM buildings in the Almaty region of Kazakhstan, solid clay brick units of 245 mm ×117.5 mm × 60 mm (length × thickness x height) dimensions were used in the construction of the URM wall specimens. The compressive strength of the units (f_b) was determined by placing half length of the clay brick into

a UTM and conducting compression strength tests on five samples according to ASTM C67/C67M-21 [41]. The tests were conducted with rubber pads placed between the samples to ensure uniform transfer of load on the bricks and subjecting it to axial load until a point when no further increase in axial load is observed, as shown in Figure 3.8. The compressive strength was evaluated by dividing the maximum load at failure by the area of contact between the sample and machine testing plates. Five brick samples were tested, and their average strength was 11.39 MPa, with a standard deviation of 1.45 MPa (see Table 3.3).

Figure 3.8: Compression test conducted on brick units.

$$f_b = \frac{\mathrm{F}}{\mathrm{A}} \qquad (3.1.)$$

Where f_b represents the compressive strength of clay brick, F represents the peak load applied on each brick before crushing, and A is the surface area of the brick on which load is applied.

Table 3.3: Compressive strength of clay bricks

Sample	Dimension (mm)	Area (mm^2)	Peak load (kN)	Compressive Strength (f_b) (MPa)	Average compressive strength (f_b) (MPa)
1	117x123	14391	182.76	12.70	
2	117x123	14391	188.51	13.10	
3	117x123	14391	142.25	9.88	11.39
4	117x123	14391	147.48	10.25	
5	117x123	14391	158.29	11.00	

3.4.2 Mortar

Low-strength mortar of mix proportions 1: 3.75: 0.821 (cement: sand: water) by weight was used in the construction of the wall specimen. During wall construction, cube samples were taken for each layer of the wall, and standard 50 mm x 50 mm x 50 mm cube mortar samples were produced for testing, with 6 specimens produced from each mixture made for the construction of each wall specimen. These specimens were stored in ambient air conditions with dry curing done to closely mimic that of the mortar used in the wall construction. Testing of mortar samples was conducted after 28 days and on the day of wall testing using the concrete crushing machine at the concrete construction laboratory in the concrete construction laboratory. Figure 3.9 show the testing of mortar compressive strength being carried out in the laboratory.

The mean compressive strength, ($f_{c\ mortar}$) of the mortar cubes of each wall layer after 28 days and on the day of the wall testing are shown given in Table 3.4. The mean compressive strength of the mortar used in the construction of wall specimens (URW, RW-1, & RW-2) at the time of in-plane wall testing is 4.52 MPa, 5.61 MPa, and 5.41 MPa with coefficient of variation of 23.14%, 24.18%, and 22.64% respectively. The mortar strength results are given in Table 3.4 and Figure 3.10.

Figure 3.9: Pictures showing the compressive strength test conducted on mortar samples

Table 3.4: Average compressive strength of mortar for wall layers

Layer No.	URW		RW-1		RW-2	
	28 days	59 days	28 days	58 days	28 days	58 days
1L	62.04	62.04	7.61	7.61	2.56	2.66
2L	5.39	5.39	7.61	7.61	2.56	2.66
3L	3.45	3.45	7.61	7.61	3.67	5.79
4L	2.90	2.90	5.48	5.48	3.67	5.79
5L	5.28	5.28	5.48	5.48	3.67	5.79
6L	4.73	4.73	4.82	4.82	5.51	6.55
7L	4.24	4.24	4.82	4.82	5.51	6.55
8L	3.79	3.79	6.04	6.04	3.72	4.22
9L	3.79	3.79	6.04	6.04	3.72	4.22
10L	6.55	6.55	6.00	6.00	5.72	6.20
11L	6.55	6.55	6.00	6.00	5.72	6.20
12L	4.41	4.41	5.88	5.88	5.72	6.20
13L	4.41	4.41	5.88	5.88	6.84	5.22
14L	3.92	3.92	3.49	3.49	6.84	5.22
15L	3.92	3.92	3.49	3.49	5.07	5.25
16L	4.41	4.41	3.49	3.49	5.07	5.25

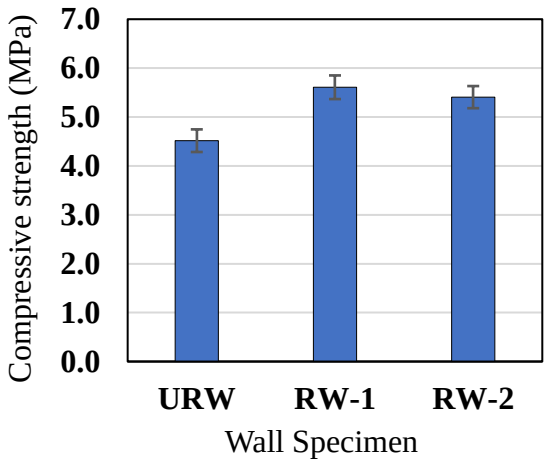

Figure 3.10: Average compressive strength $f_{c\ mortar}$ of mortar on day of wall testing

3.2.3 Lightweight Engineered Cementitious Composite (LWECC)

3.2.3.1 LWECC Design Mix Proportions

For retrofitting of masonry walls, two lightweight engineered cementitious composites (LWECC) mix designs were prepared for retrofitting of wall specimens RW-1 and RW-2, and the proportions are outlined in Table 3.5. The material mix proportions were selected based on mix designs presented by Wang and Li [35], and Zhu et al [42].

Table 3.5: Mix proportions of LWECC

Mix	OPC	Sand	S15	Water	PVA (% vol)	HPMC* (%)	SP* (%)
RF-1	1	0.165	0.60	0.40	2.0	0.15	1.0
RF-5	1	0.500	0.15	0.70	2.0	0.20	2.0

* % content of cement

A summary of material properties used in the preparation of LWECC can be found in Table 3.8. High-strength grade 500 Ordinary Portland Cement, OPC (CEM I 42.5) with a specific gravity of 3.15 is used as the cementitious material of the matrix. The sand used is standard silica sand with a specific gravity of 2.4 which is within the gradation limits of sand for mortar sand and according to the gradation chart in Figure 3.11 falls within the upper bound of the sand gradation (between G-Left and S-left).

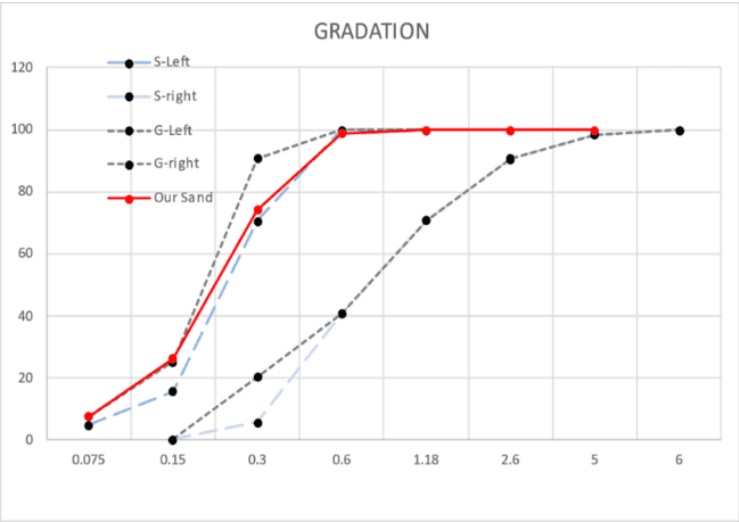

Figure 3.11: Sand gradation

Table 3.6 show the properties of the Glass Micro-hollow Bubble represented as S15, which was used in the partial replacement of sand as the aggregate of the LWECC to achieve the lightweight properties of the composite. High-range polycarboxylate-based superplasticizer (BASF Glenium ACE 80) is used as a water-reducing additive to increase the workability of the composite. To prevent segregation and bleeding of the wet mix prior to the addition of fiber and to ensure appropriate dispersion of fibers, industrial-grade hydroxypropyl methylcellulose (HPMC) is employed as a viscosity modifying agent.

Table 3.6: Properties of S15

		unit
Typical true specific gravity	0.15	
Thermal conductivity	0.055	(W/m.K)
Particle size range	25 - 90	(μm)
Median Particle size	55	(μm)
Isostatic crush strength	2.1	(MPa)

Table 3.7: Properties of PVA fiber

Length (mm)	Diameter (μm)	Tensile strength (MPa)	Young's modulus (GPa)	Elongation (%)	Density (kg/m^3)
12	40	1600	40	22.1	1300

Short Polyvinyl alcohol (PVA) fiber from Kuraray Co. Ltd, Japan which has a specific gravity of 1.3 and consists of 1.2% oil mass surface coating to reduce chemical bonding with the cementitious matrix was used in the reinforcing of the cementitious matrix to achieve the strain-hardening. The properties of the PVA fiber are shown in Table 3.7.

Table 3.8: Summary of materials properties for LWECC

Material	Type	Abbreviation	Density
Ordinary Portland Cement	CEM I 42.5H	OPC	1.5
Sand	Silica sand	S	2.4
Glass Bubble	Micro-hollow glass bubbles	S15	0.15
Water	-	W	1.00
Fiber	Polyvinyl alcohol fiber	PVA	1.30
Viscosity Modification Agent	Hydroxypropyl methylcellulose	HPMC	-
Superplasticizer	BASF Glenium ACE 80	SP	-

3.2.3.2`Mixing and Curing of LWECC

All mixtures were prepared in a pan mixer of 40 liters effective capacity. The mixing of the LWECC was done in 3 batches of 14 liters volumes for each side of the wall face. The mixing procedure involved mixing OPC with a mixture of SP and 50% of the required water for 1 min. Sand, S15, and HPMC were added and mixed for 3 mins to reach the proper fluidity of the matrix. The mixer was stopped with all samples scrapped from the sides of the mixer within 5 mins. Finally, fibers and the remaining amount of water were added into the mortar and further mixed for 9 mins to ensure good constituency and dispersion of the fiber. The fresh mixture was immediately trowelled onto the surfaces of the retrofitted wall to the required thickness of 15mm on each face with (100 mm diameter x 200 mm length) cylinder samples and 50 mm thick dog-bone samples (with dimensions shown in Figure 3.12) cast for conducting of compressive and tensile strength tests respectively. Table 3.9 shows the summary of the mixing process.

Table 3.9: Summary of LWECC mixing process

Steps	Mix ingredients for each step	Duration (S)
Step 1	OPC + 0.5W + SP	60
Step 2	Sand + S15 + HPMC	180
Step 3	Stop and scrape the sides of the mixing bowl	300
Step 4	0.5W + PVA	540

To closely attain the same properties between the LWECC samples and that trowelled on the masonry wall, the cylinder, and dog-bone samples were constantly moistened every day with

water sprayed on the LWECC samples and stored under normal room temperature until the day of testing. Figures 3.13 & 3.14 show both dog-bone and cylinder samples prepared for testing during the mixing of the LWECC for the retrofitting of RW-1 and RW-2.

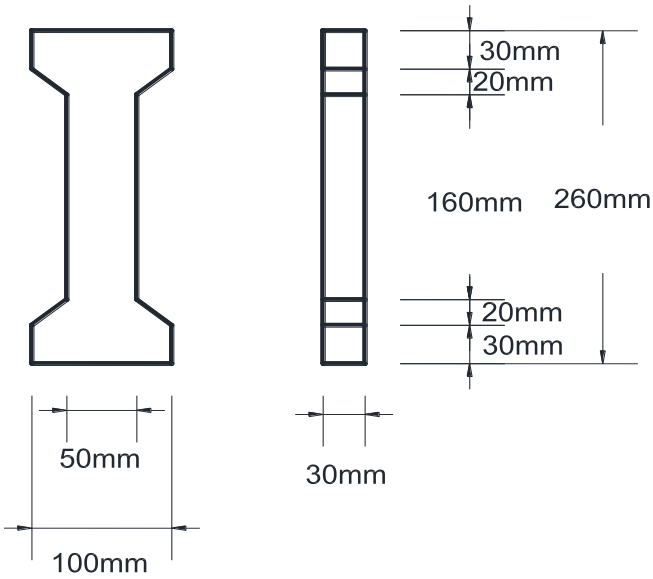

Figure 3.12: Schematic diagram of dog-bone samples

Figure 3.13: Dog-bone samples cast during retrofitting of wall specimens

Figure 3.14: Cylinder samples cast during retrofitting of wall specimens

3.2.3.3 Mechanical Properties of ECC

Compressive Strength Test

The compressive strength of the design mixes was measured using uniaxial compression tests on the cylinder samples, performed a day before wall testing to obtain the compressive strength of the composite at the time of the wall test. The tests were performed with a 1000kN hydraulic servo universal testing machine in accordance with the procedure described in ASTM C39/C39M-21 [43]. As shown in Figure 3.15, two linear variable differential transformers (LVDTs) were used to monitor the uniaxial deformation on both sides of each sample while testing. Displacement mode of load control was employed as the loading method with a loading rate of 1mm/min. The average compressive strength, $f_{c\,LWECC}$ obtained for the LWECC retrofits (RF-1 & RF-5) are 27.10 MPa, and 11.13 MPa with a coefficient of variation of 1.49% and 8.38% respectively, and is displayed in Figure 3.19. Figure 3.16 show the compression stress-strain curves for each mix.

Figure 3.15: LWECC uniaxial compressive strength testing

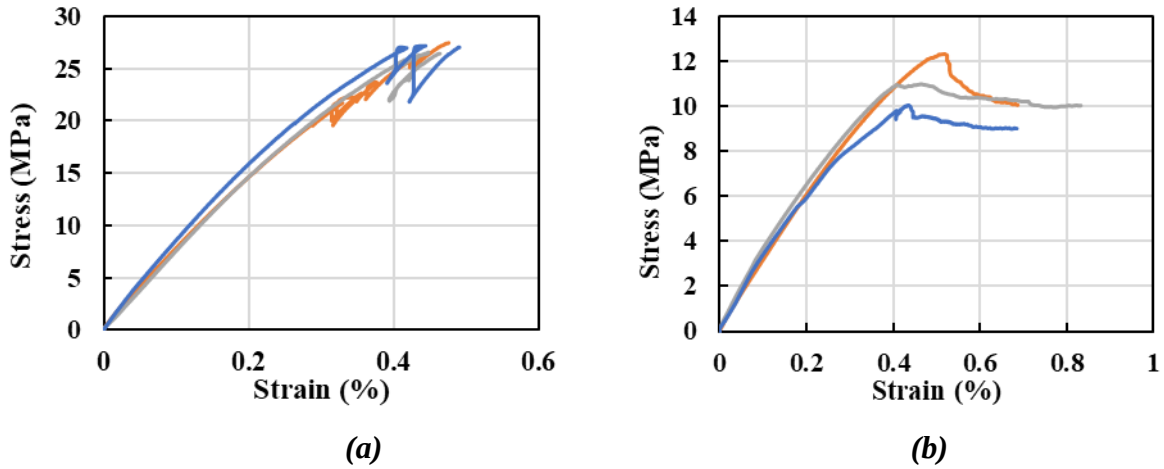

(a) ***(b)***

Figure 3.16: Compression Stress-Strain curves for Cylinder samples: (a) RF-1; (b) RF-5

Direct Tensile Test

To evaluate the tensile properties of the LWECC specimens, direct tensile tests were performed on three samples a day before wall testing to obtain the tensile strength of the composite at the time of the wall testing. Direct tensile testing was chosen to test for the composites' tensile strength so the strain-hardening behavior of the composite can also be obtained. The specimens were air-dried for 24 hours before testing to eliminate the influence of moisture during testing. The tensile tests were carried out using a displacement-controlled mode on a 1,000 kN hydraulic servo universal testing machine with a loading rate of 0.5 mm/min, with both ends of the extensometer exactly positioned at the top and lower border of the testing region depicted in Figure 3.17. The maximum tensile forces each sample could withstand were measured by the load cell while an extensometer of 100mm gauge length measured the tensile/axial strain of the dog-bone samples. The ends of the dog-bone samples were strengthened with instant hardening epoxy glue to avoid cracking outside the measured region.

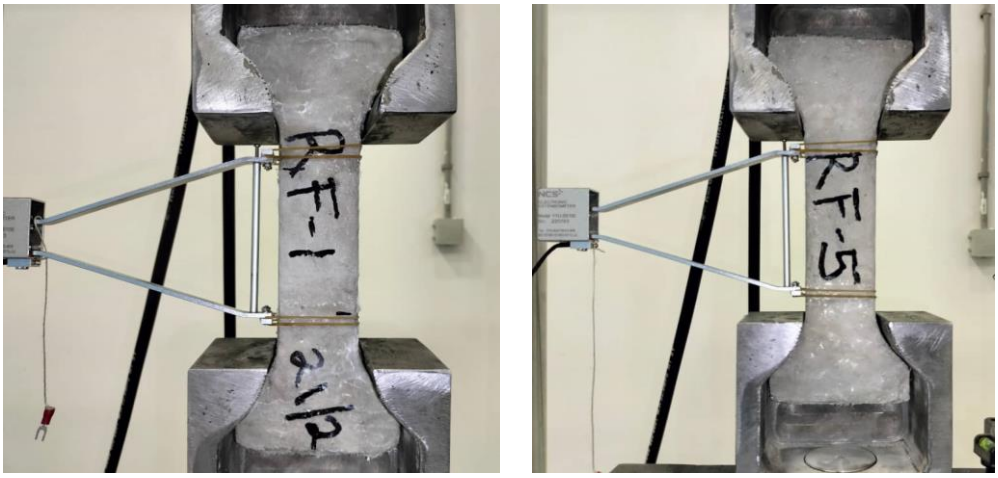

Figure 3.17: Direct tensile strength testing on dog-bone samples

The average tensile strengths of RF-1 & RF-5 are 3.75 MPa, and 2.63 MPa with a coefficient of variation of 6.00% and 14.32% respectively, and are presented in Figure 3.19. The tensile stress-strain curves for both LWECC mixes are presented in Figure 3.18, indicating high strain-hardening capacities with average ultimate tensile strain capacities (ε_{tu}) of 1.48% and 1.80% for RF-1 and RF-5 respectively.

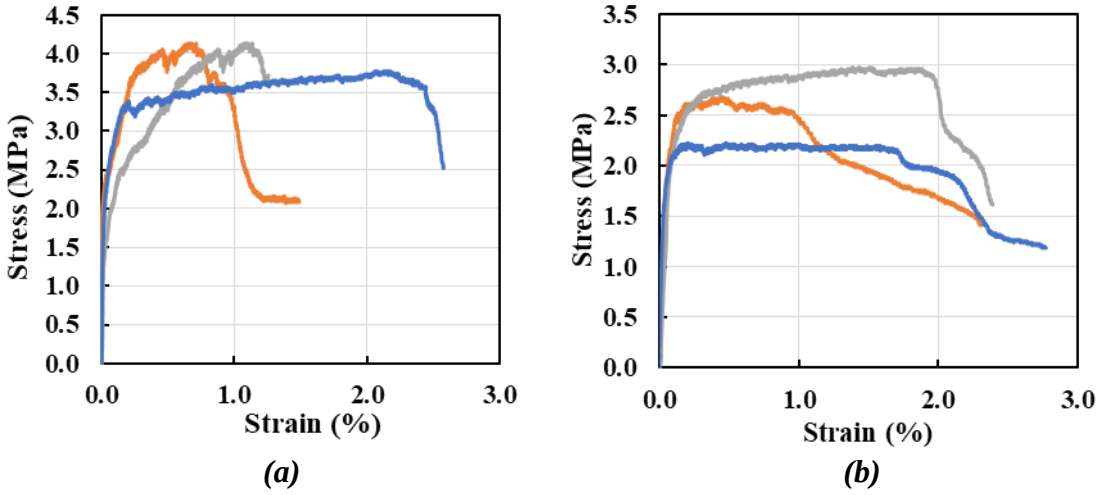

Figure 3.18: Tension Stress-Strain curves for dog-bone samples: (a) RF-1; (b) RF-5

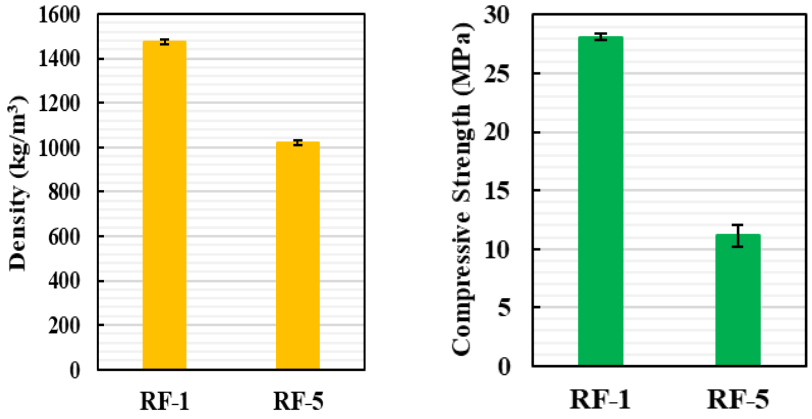

Figure 3.19(a): Properties of LWECC: (a) Density; (b) Compressive strength

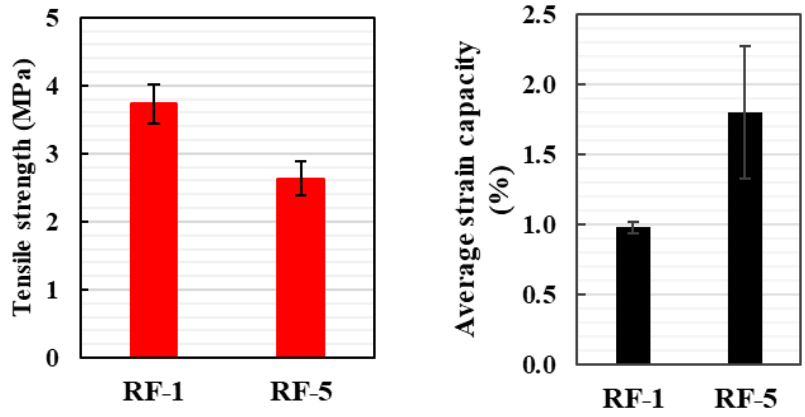

Figure 3.19(b): Properties of LWECC: (a) tensile strength; (b) Strain Capacity

3.5 Wall Instrumentation

The test walls were instrumented with five linear variable differential transformers (LVDTs) and four string potentiometers to measure the horizontal top displacements, all deformations, uplifts, and crack propagations experienced by each wall specimen. The locations of the test instrumentations are shown in Figure 3.20.

String potentiometers 1 & 2 were installed along both transverse sides of the wall to measure transverse deformations undergone by each wall during testing. String potentiometers 3 & 4 were installed at the wall sides from the top beam to the top of the foundation beam to quantify the uplifts at both sides of each wall specimen. LVDT 1 & 2 were installed near the wall edges 80 mm above the bed joints to measure uplifts at both ends of the wall toes induced by the rocking failure. LVDTs 3 & 4 were mounted at the ends of the foundation beams to monitor any possible sliding of the foundation beams during the wall test, and LVDT 5 was mounted at the top left end of the wall opposite to the horizontal actuator to measure the horizontal top displacement of each wall specimen.

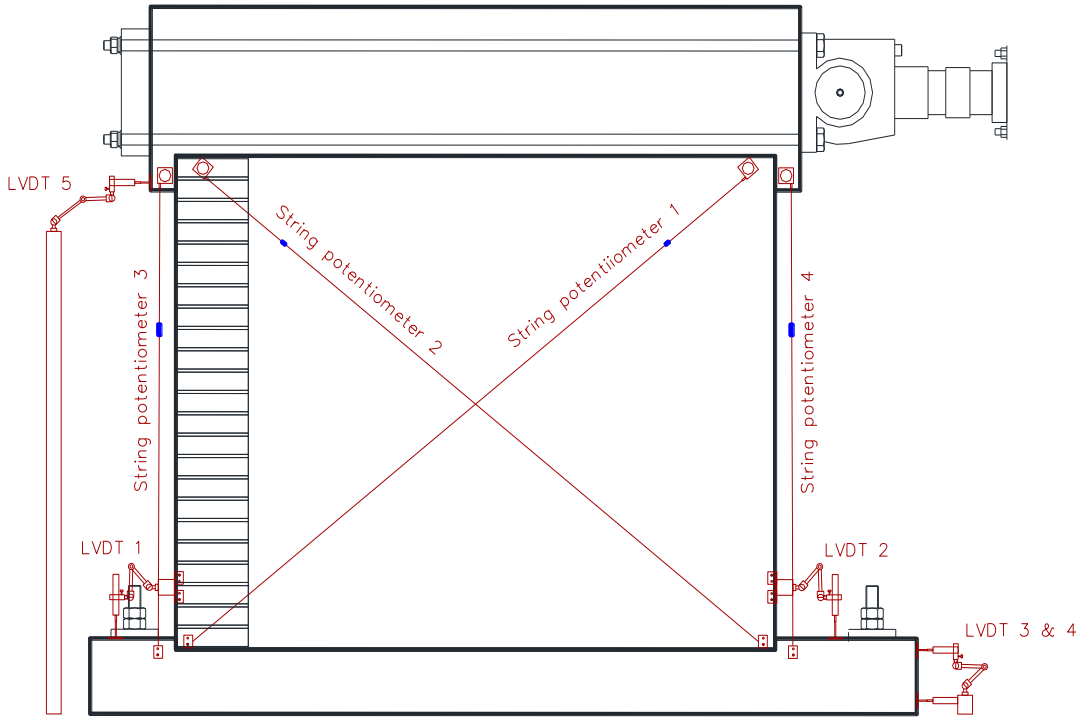

Figure 3.20: Instrumentation setup for wall specimens before conducting of wall test

Chapter 4: Results and Discussions

4.1 Force-displacement response

The lateral force-displacement response of tested wall specimens URW, RW-1, and RW-2 are illustrated in Figure 4.1 in the form of hysteresis loops. The hysteretic response of all wall specimens was approximately linearly elastic in behavior from the initial loading until the peak load. The shape of the hysteresis loop widened due to the occurrence of cracks within the walls.

After the peak lateral force, the shape of the loop curves for URW became quite wide, especially in the application of positive lateral force. This resulted from the presence of wall uplifts at both sides of the wall and toe crushing at the west end of the wall. There was also a sudden loss of lateral strength at the last cycle of 10mm displacement due to no more adequate shear resistance in the wall which resulted in the termination of the test for safety purposes. However, RW-1 and RW-2 were able to undergo more cycle loading after the occurrence of cracking and attainment of maximum lateral force resulting in the gradual widening and tilting of the hysteresis loop to the horizontal axis. When the LWECC retrofit stripes began experiencing shear cracking, the pattern of the hysteresis loops became similar to the pattern of the un-retrofitted wall specimen but was able to under more loading resulting in more cycles in the hysteresis loop. This was possible as there was no significant and/or sudden failure in the LWECC retrofit even after the attainment of the maximum lateral force which was expected due to the high displacement capacity of the LWECC stripes resulting in the termination of the test for RW-1 and RW-2 at 16 mm and 22 mm displacement loading respectively.

Figure 4.1 shows that URW was able to attain a maximum lateral force resistance of 237.9 kN and 272.03 kN on the positive and negative sides respectively. RW-1 was able to attain a maximum lateral force resistance of 258.51 kN and 281.42 kN on the positive and negative sides respectively, while wall RW-2 attained maximum lateral force resistance of 272.47 kN and 281.37 kN respectively. This shows an approximately symmetrical behavior in both the positive and negative directions for all wall specimens with an increase of 6.06% and 8.98% in the lateral force resistance for RW-1 and RW-2 respectively.

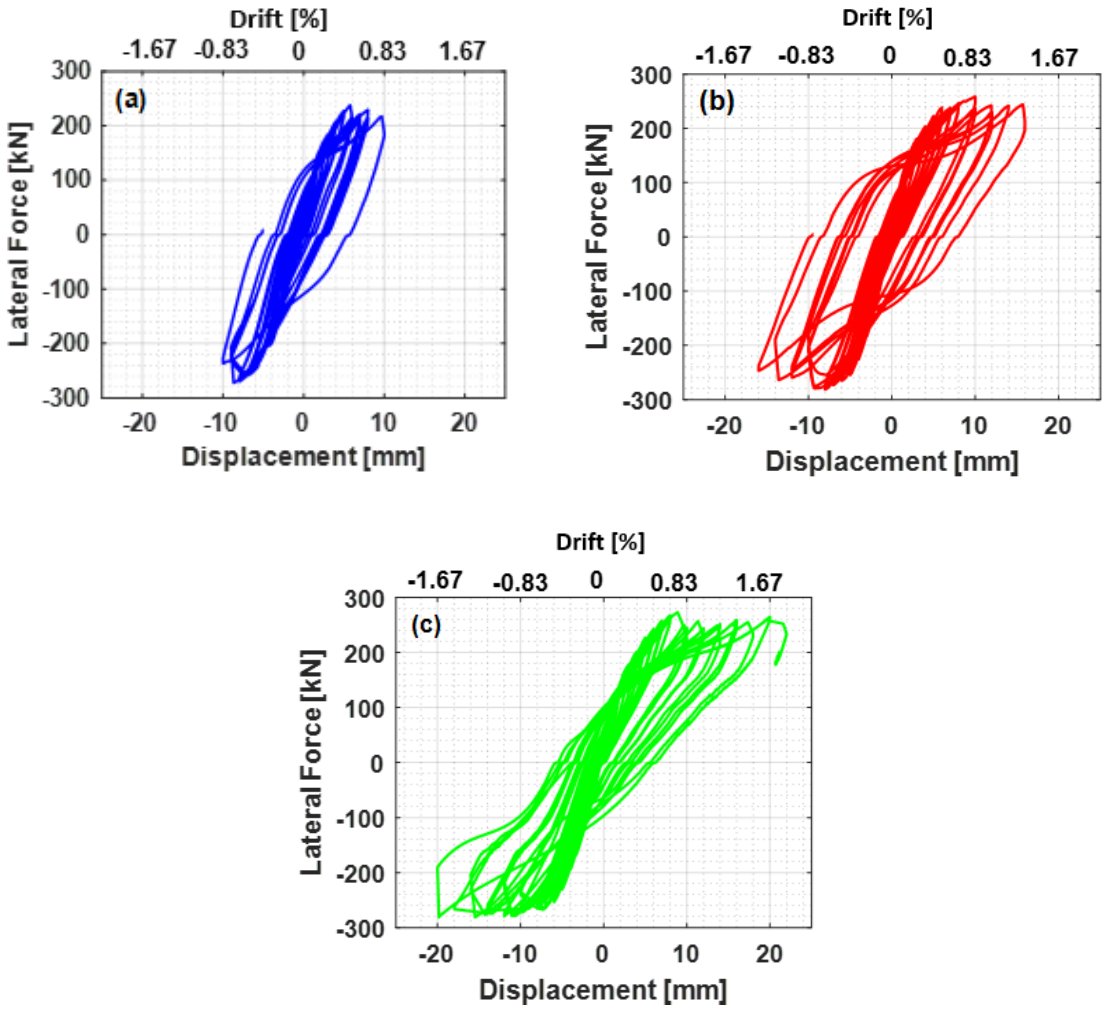

Figure 4.1: Hysteretic curves of the wall specimens: (a) URW; (b) RW-1; (c) RW-2

The hysteresis loop for each wall specimen is divided into stages of elasticity and presented in Figures 4.1-4.3, with pictures of the wall for positive and negative loading at the end of each elasticity stage shown. URW exhibited elastic behavior from initial loading until 0.25% drift, plastic behavior after 0.25% drift until 0.42% drift when the wall achieved maximum lateral load then large deformations exhibited by large hysteresis loops until ultimate failure at 0.83% drift. Similarly, RW-1 exhibited elastic behavior until 0.25% drift, but the LWECC retrofit (RF-1) extended the plastic region to 0.67% drift where it achieved maximum lateral load after which large hysteresis loops were observed indicating large deformations until ultimate failure at 1.35%drift. Retrofitting of specimen RW-2 with RF-5 retrofit resulted in the wall exhibiting elastic behavior until 0.67% drift when the wall achieved maximum lateral load before switching to

plastic behavior and exhibiting expanded hysteresis loops from 1.01% drift, which appeared to be narrow than previous walls until ultimate failure at 1.85% drift.

Figure 4.2: URW hysteresis loop stages

Stage 1: 0 – 3 mm displacement

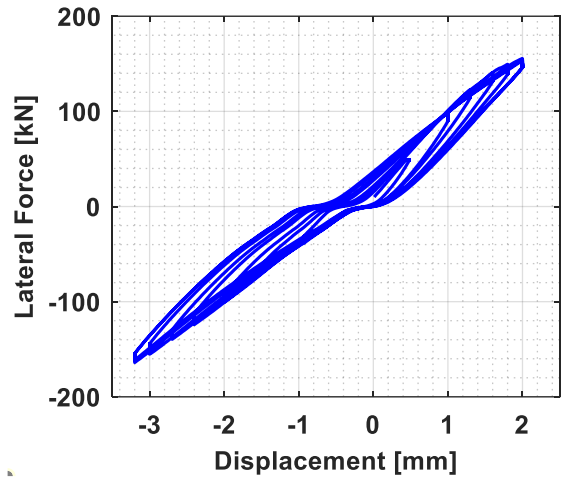

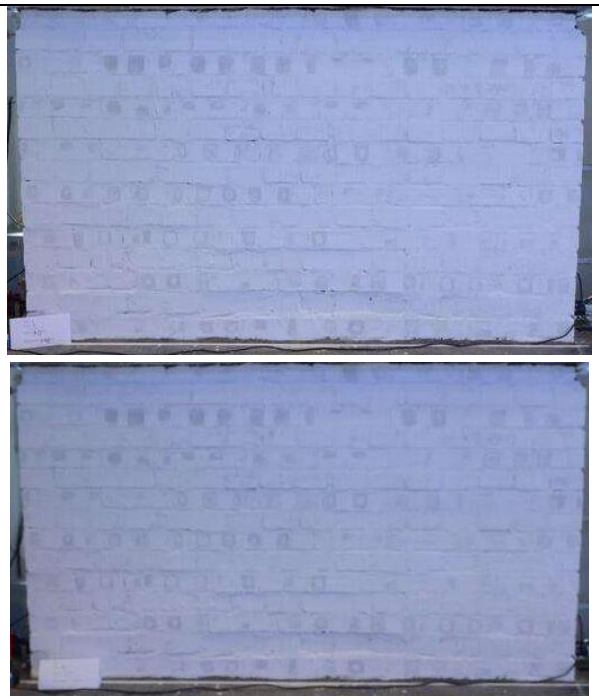

Stage 2: 3 – 6 mm displacement

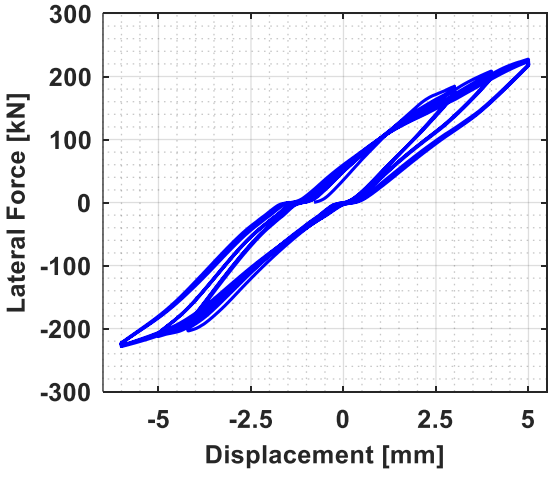

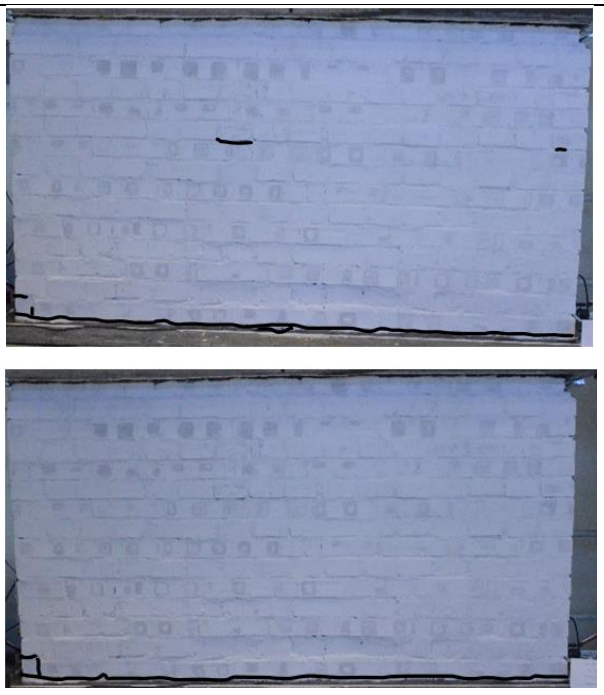

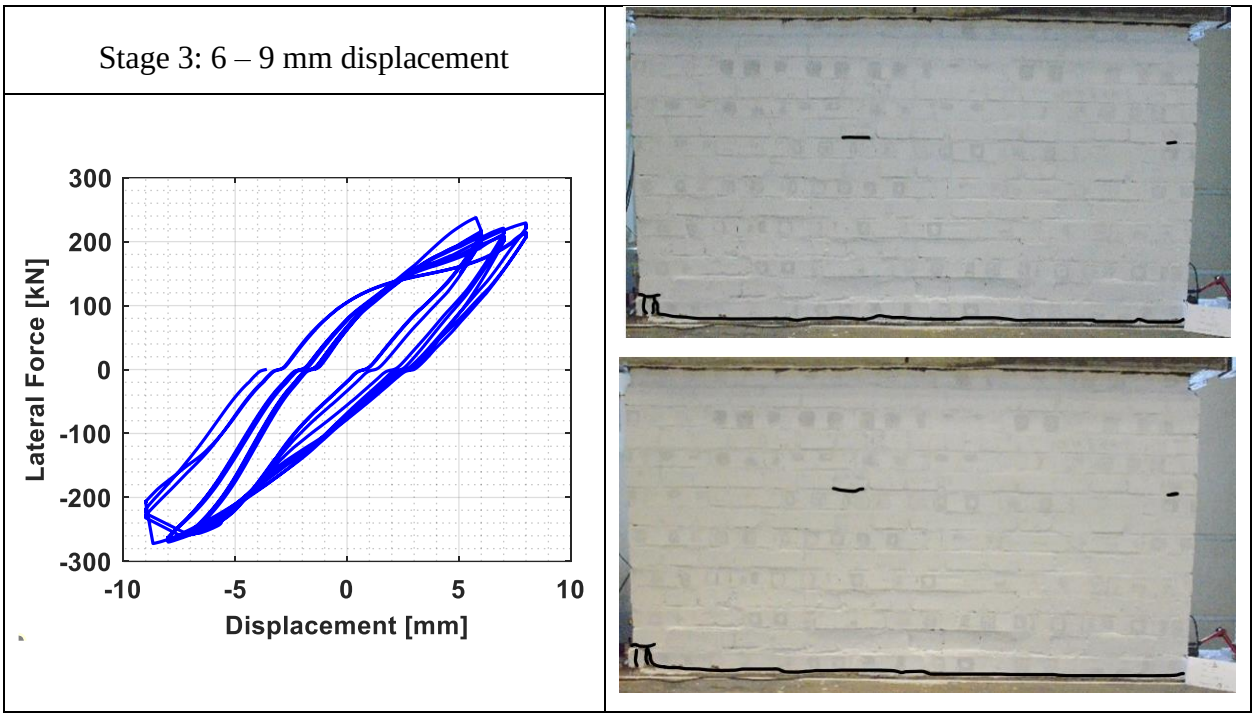

Figure 4.3: RW-1 hysteresis loop stages

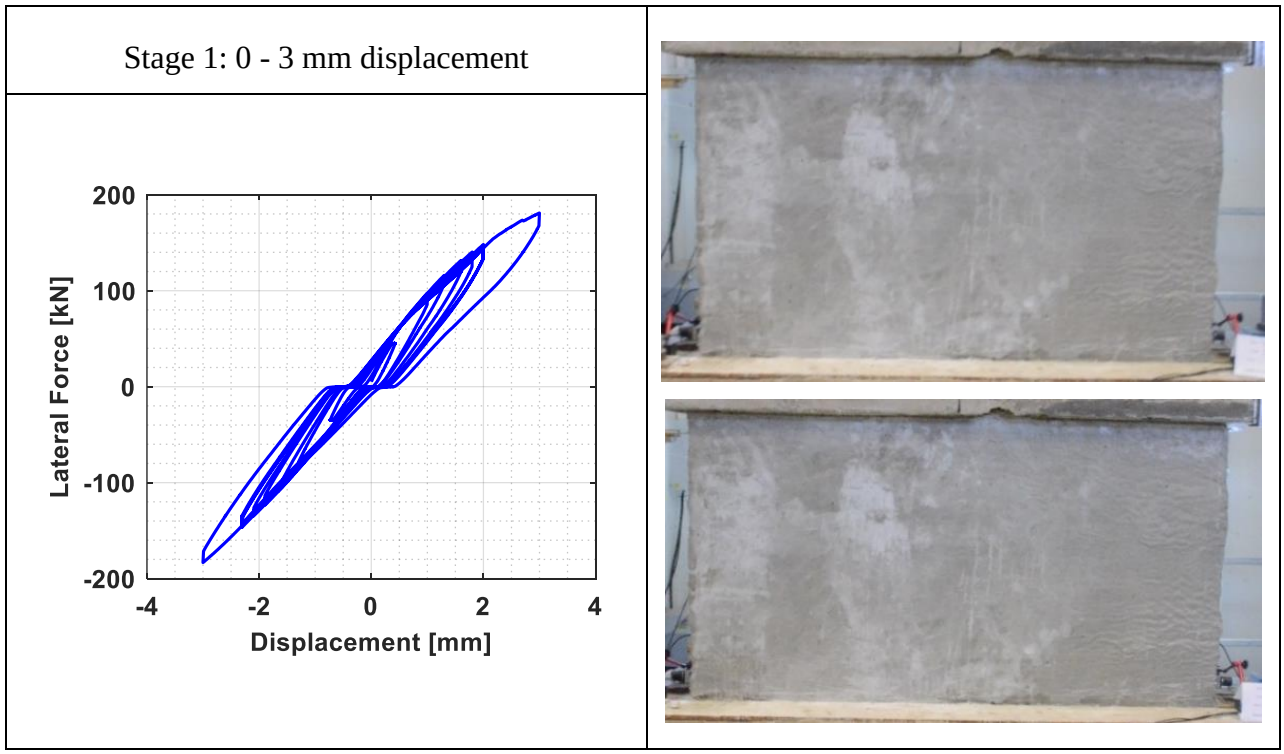

Stage 2: 3 -10 mm displacement

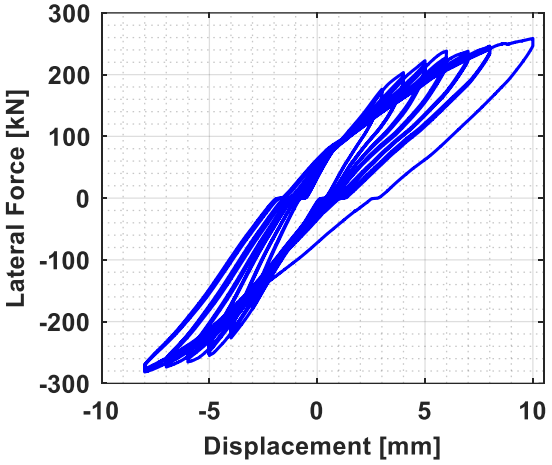

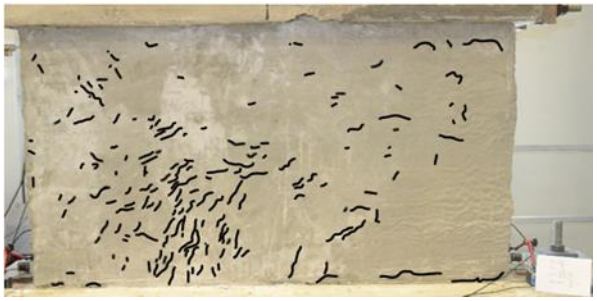

Stage 3: 10 -16 mm displacement

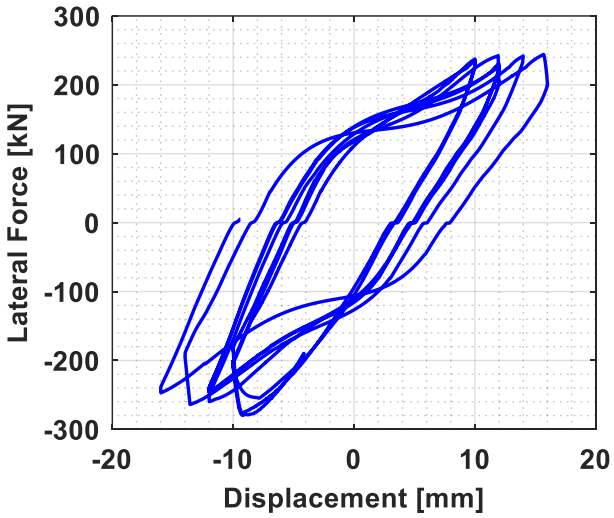

Figure 4.4: RW-2 hysteresis loop stages

Stage 1: 0 -8 mm displacement

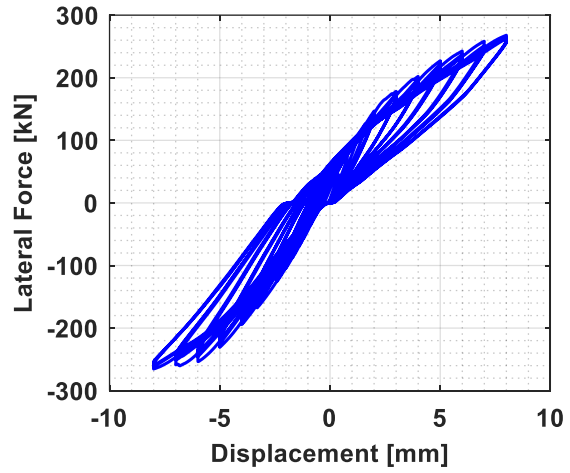

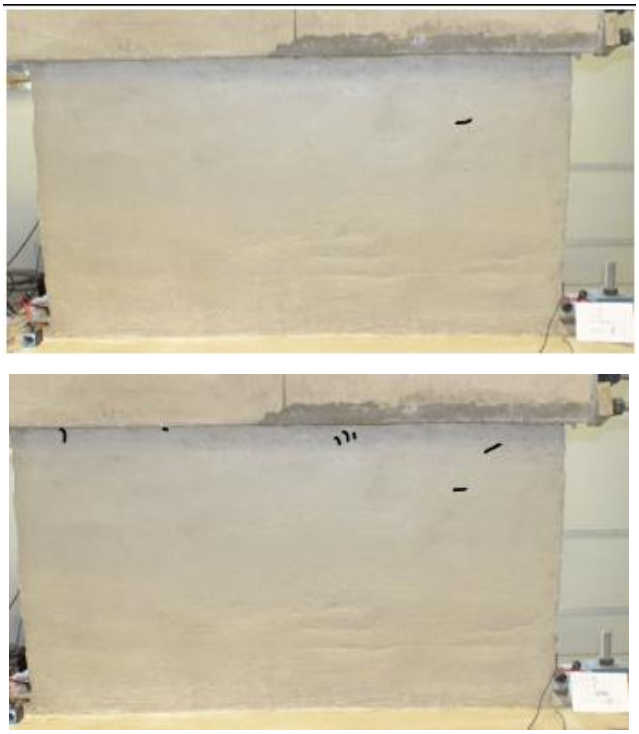

Stage 2: 8 -12 mm displacement

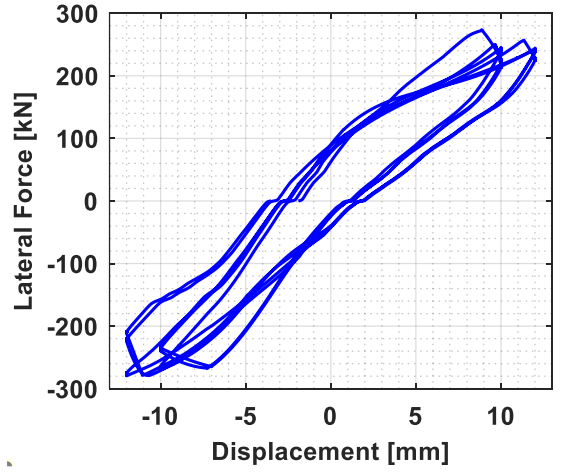

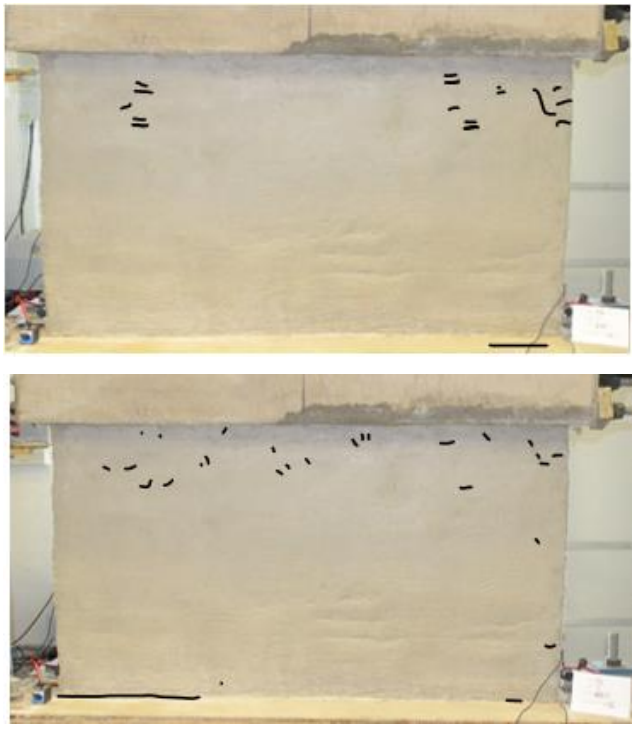

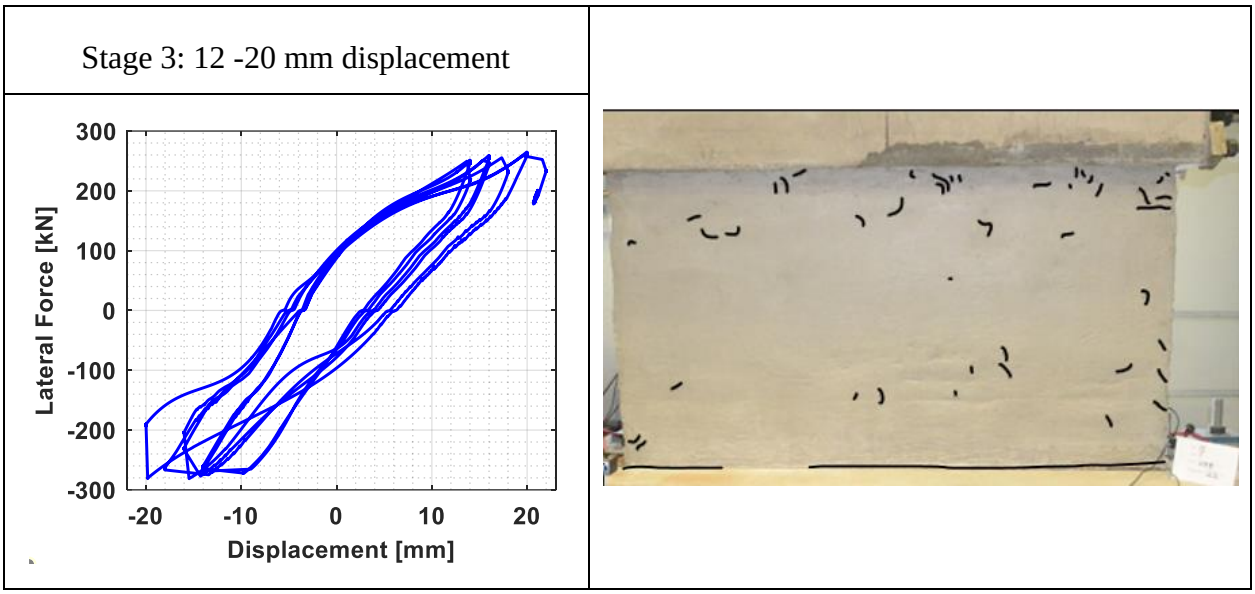

The lateral load–displacement responses for each wall specimen are presented in the form of backbone curves and are shown in Figure 4.5a. The backbone curves are derived from the hysteresis loops by connecting each point of maximum load for the force-controlled stage and the maximum displacement for the displacement-controlled stage during the first cycle of each loading step.

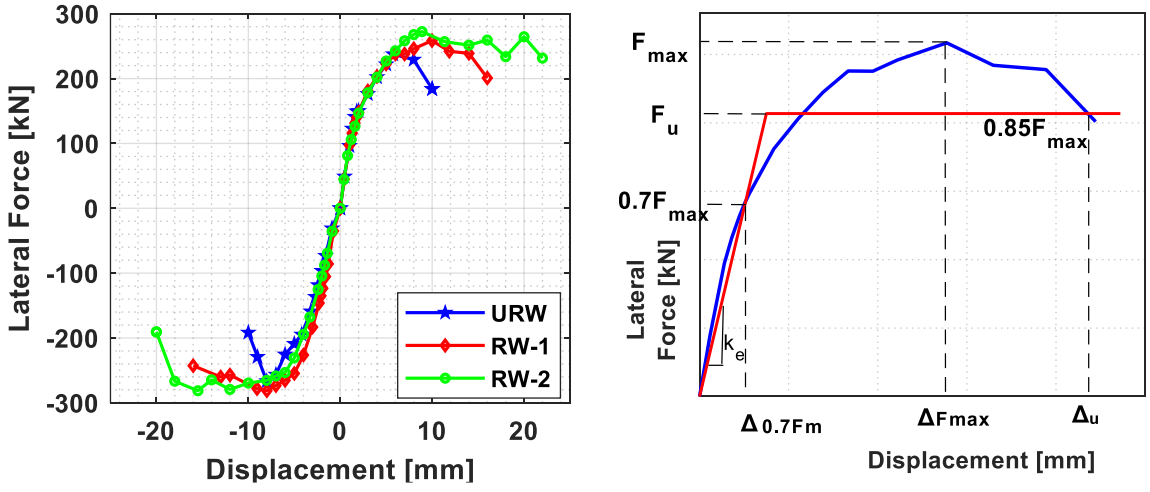

Figure 4.5: (a) Backbone curve of wall specimens; (b) Idealization of backbone curve

The in-plane wall response parameters were computed from the backbone curves and a brief of the calculated parameters is presented in Table 4.1. The response parameters are presented

for both the positive and negative cycles. The backbone curves were used to obtain parameters at key points along the backbone curves of the wall specimens and this key parameter is illustrated in an idealized curve shown in Figure 4.5b. The ultimate shear resistance F_u for each wall is determined at a lateral load corresponding to 85% of F_{max} (Equation 4.1), where F_{max} is the maximum load attained by the backbone curve. The walls' ultimate displacement capacity Δ_u was computed as the displacement corresponding to 15% F_{max} strength degradation (Equation 4.2). The ultimate drift capacity of each wall specimen is represented as the ratio between the ultimate displacement capacity and height of each wall specimen, expressed in percentage (Equation 4.3). The effective stiffness k_e denotes the experimental backbone curve's secant stiffness at the development of the first major cracks that alter the curve's slope. Different research in the past has proven that such cracks typically occur at approximately 60-80% of the shear strength [24], [44]. Therefore, the effective stiffness was determined from the secant of the experimental backbone curve at $0.7F_{max}$ according to Equation 4.4 and reported in Table 4.1.

$$F_u = 0.85F_{max} \tag{4.1}$$

$$\Delta_u = \Delta_{0.85F_{max}} \tag{4.2}$$

$$\delta_u = \frac{\Delta_u}{h_w} \tag{4.3}$$

$$k_e = \frac{0.7F_{max}}{\Delta_{0.7F_{max}}} \tag{4.4}$$

Where $0.85F_{max}$ corresponds to 85% of the maximum lateral force, $\Delta_{0.85F_{max}}$ is the displacement corresponding to 15% drop of the maximum lateral force on the backbone curve, h_w is the wall height, $0.7F_{max}$ correspond to 70% of the maximum lateral force from start of the backbone curve, and $\Delta_{0.85F_{max}}$ is the displacement corresponding to 15%drop in the maximum lateral force.

4.2 Displacement ductility capacity

The determination of the walls' displacement ductility factor is the ratio of the wall's final displacement over the yield/elastic displacement (Equations 4.5), in accordance with the method adopted by Mahmood and Ingham [10]. It allows for the description of a structural component beyond its elastic range.

$$\mu = \frac{\Delta_u}{\Delta_e} \quad (4.5)$$

where Δ_u is the ultimate displacement calculated for each wall specimen. Δ_e is the displacement required to reach the ultimate lateral force and is defined as the ratio of the ultimate shear resistance, $F_{u,}$ to the effective stiffness, k_e.

The ductility capacity varied significantly among all evaluated wall specimens (Table 4.1, with a high percentage increase in the retrofitted wall specimen to average values of 151.91% and 151.18% for RW-1 and RW-2 respectively. The high increase in displacement ductility value is an indication of the high efficiency of hand-trowelled cementitious composite in significantly improving the displacement capacity of URM walls, confirming the conclusion presented by Lin et al. about having higher ductility for hand-trowelled retrofit compared to when the shotcrete is sprayed [31].

Table 4.1: In-plane wall responses parameters for wall specimens

Wall Specimen		F_{max} (kN)	F_u (kN)	Δ_u (mm)	δ_u (%)	K_e (kN/mm)	Δ_e (mm)	μ [-]	% increase in F_u	% increase in Δ_u	% increase in K_e	% increase in μ
URW	+ve	237.90	201.94	9.20	0.77	63.36	3.19	2.89	-	-	-	-
	-ve	272.03	226.53	9.07	0.76	46.67	4.85	1.87	-	-	-	-
RW-1	+ve	258.51	219.73	15.01	1.25	94.49	2.33	6.46	8.81	63.12	49.15	123.58
	-ve	281.42	239.21	16.00	1.33	78.28	3.06	5.24	5.60	76.43	67.73	180.24
RW-2	+ve	272.47	231.60	22.00	1.85	76.59	3.02	7.28	14.69	139.06	20.89	151.99
	-ve	281.37	239.16	18.73	1.57	59.74	4.00	4.68	5.58	106.50	28.01	150.37

4.3 Failure mode and damage development

The full progression in crack patterns and damage development for all three wall specimens are shown in Appendix A. Generally, the wall specimens exhibited two flexural failure modes (toe-crushing and rocking). URW illustrated in Figure 4.6 URW experienced an initial rocking failure that extended across the entire length of the wall with the uplift occurring from the base at both ends of the wall until the cracks along the wall base met at the center. This led to crushing at

the toe towards the west of the wall specimen. At a large wall drift, in-plane sliding was observed around the toe which resulted in instability from out-of-plane movement (Figure 4.6c) due to the loss of constraint between the wall and its foundation.

Figure 4.7 show key points of damage development during the wall testing with flexural cracks appearing along both sides of the wall beds at 0.25% drift, the flexural crack progressed inwards to through the point when the wall experienced until 0.5% drift when the cracks had progressed to meet causing the wall to begin experiencing crushing at the left toe with some amount of out-of-plane sliding.

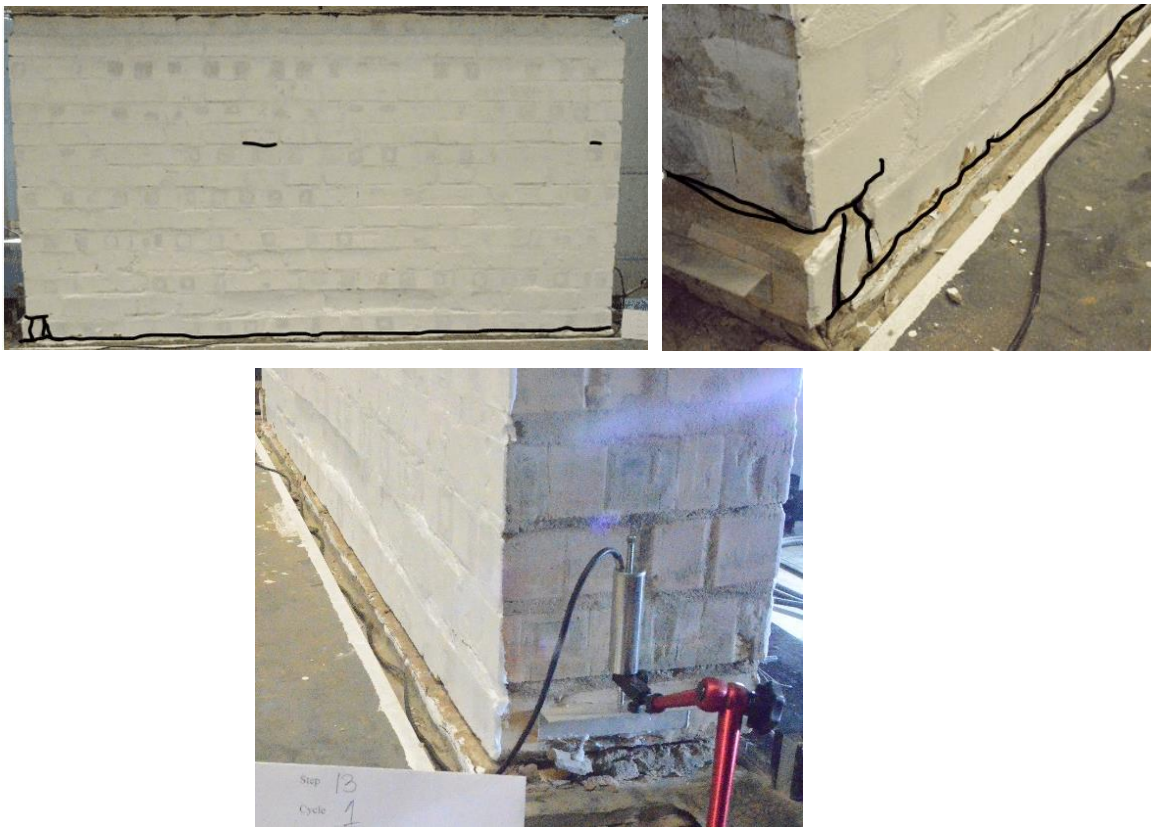

Figure 4.6: Failure mode of URW

Figure 4.7: Damage progression for URW specimen

<table>
<tr><th></th><th>Positive cycles</th><th>Negative cycles</th></tr>
<tr><td>Force:
40kN

0% drift</td><td colspan="2"> 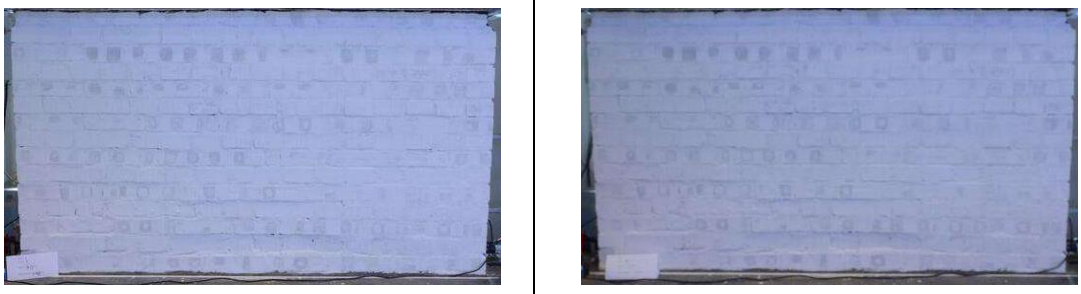 </td></tr>
<tr><td rowspan="2">Force:
193.25 kN
Drift:
0.25%</td><td> 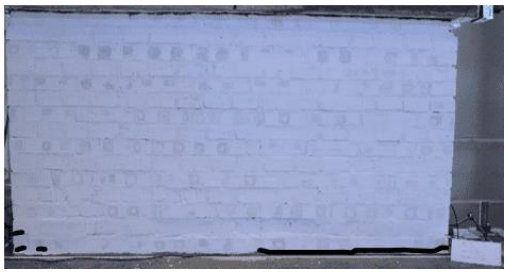 </td><td> 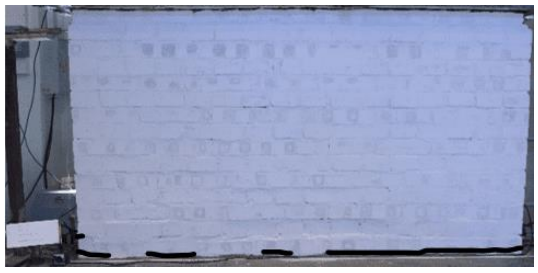 </td></tr>
<tr><td colspan="2"> 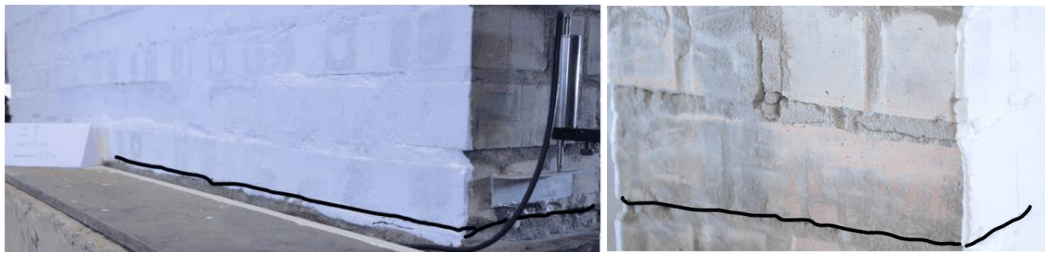 </td></tr>
<tr><td rowspan="2">Force:
227.8 kN

Drift:
0.42%</td><td> 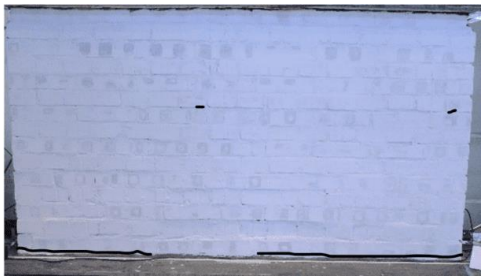 </td><td> 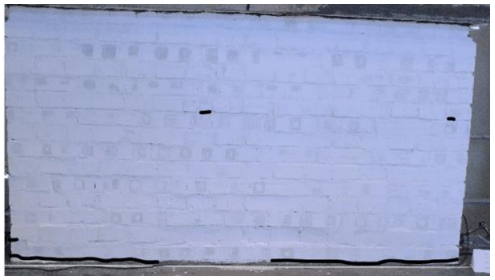 </td></tr>
<tr><td colspan="2"> </td></tr>
</table>

Force: 217.95 kN Drift: 0.50%	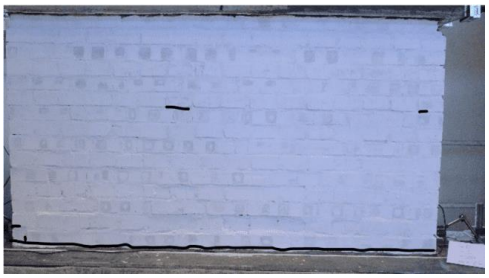	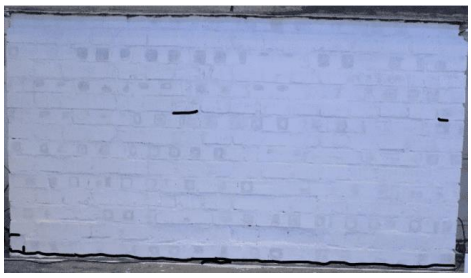
	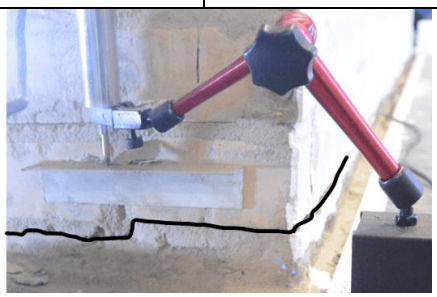	
Force: 207.5 Drift: 0.83%	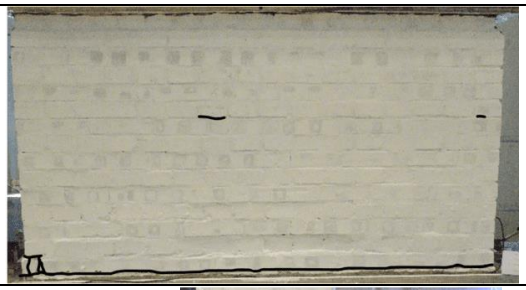	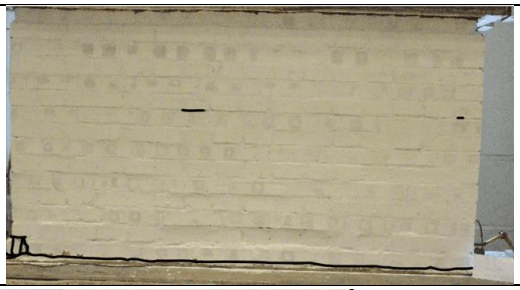

RW-1 experienced limited rocking behavior, crushing of toes on both sides of the wall, with spread-out damage cracks across the wall's body (Figure 4.8) but due to constraints provided by the LWECC retrofit, there was no out-of-plane moving by the wall. Flexural cracks were fully developed and distributed over the entire length of the wall with the specimens acting as a rigid body rotating about the toes. As the lateral load continually rose, both toes also continuously became crushed resulting in the instability of the wall.

RW-2 exhibited similar rocking behavior as the URW, followed by less severe toe damages at a much larger drift and few shear cracks across the wall (Figure 4.9). The presence of fewer

fully developed cracks distributed over the entire wall indicated the retrofit's weak capacity in resisting flexural stress resulting in rocking failure and same as with RW-1, the LWECC retrofit prevents an out-of-plane movement of the wall. This results from the low-strength, super lightweight RF-5 material having more seismic displacement capacity due to its lower stiffness and high tensile strain-hardening properties. The key stages in the progression of damage development for the retrofitted wall specimens corresponding to applied lateral force and drift capacity are shown in Figures 4.10 and 4.11.

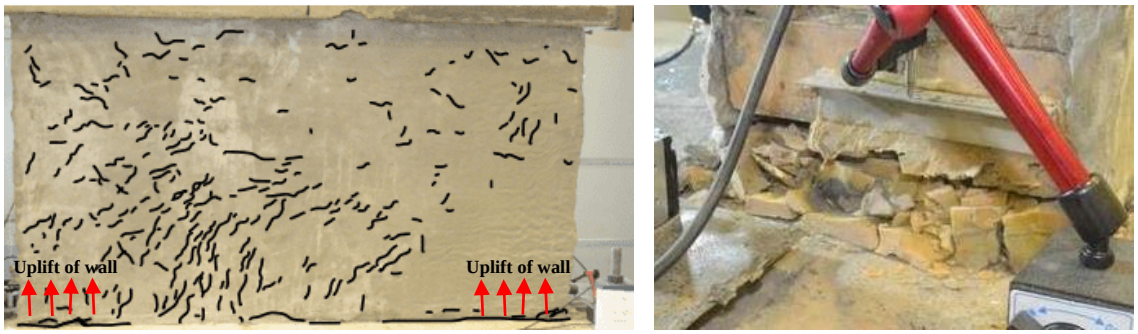

Figure 4.8: Failure mode of RW-1

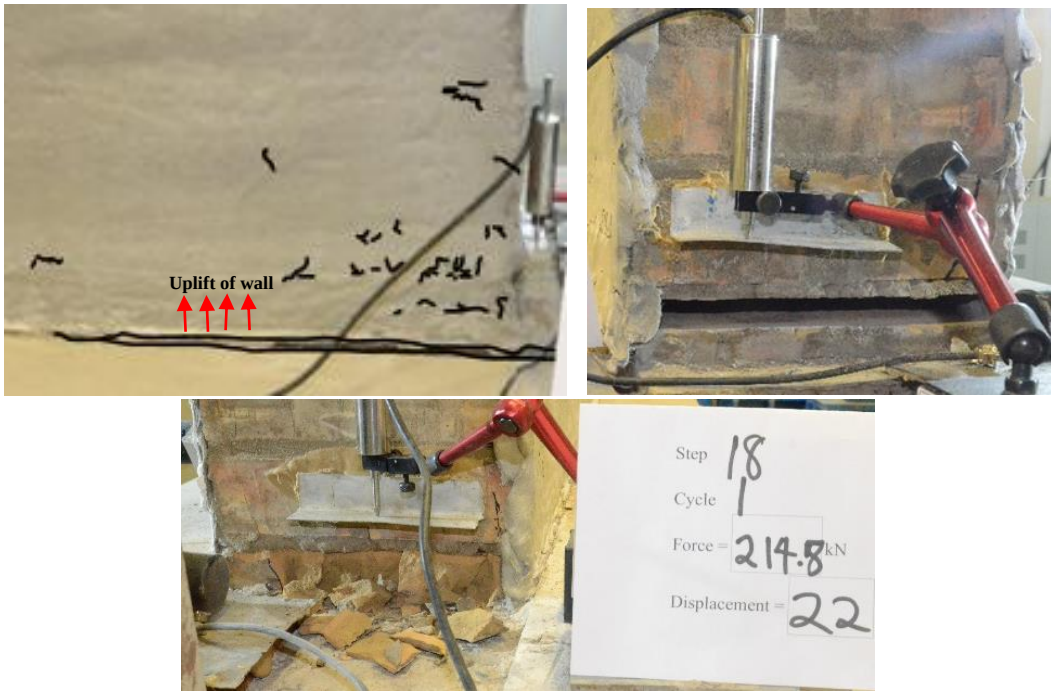

Figure 4.9: Failure mode of RW-2

Figure 4.10: Damage progression for RW-1 specimen

	Positive cycles	**Negative cycles**
Force: 40kN 0% drift		
Force: 214.70 kN Drift: 0.33%		
Force: 263.95 kN Drift: 0.67%	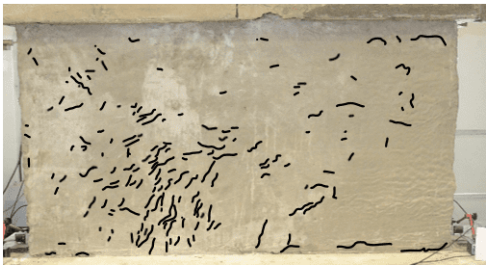	
Force: 232.90 kN Drift: 1.00%	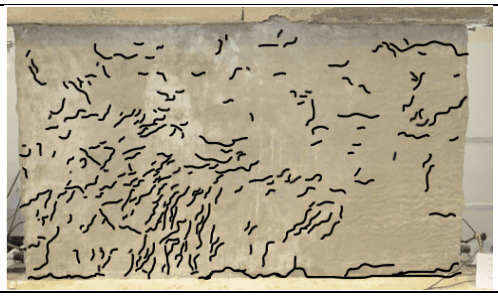 	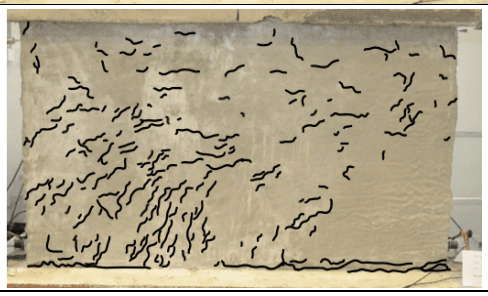

Force: 223.70 kN Drift: 1.33%		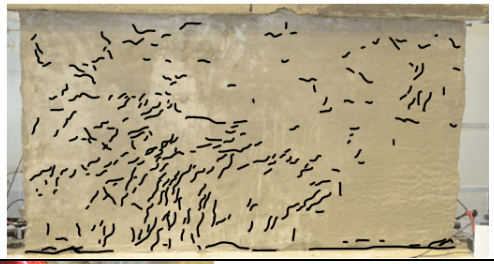

Figure 4.11: Damage progression for RW-2 specimen

	Positive cycles	**Negative cycles**
Force: 40kN 0% drift		
Force: 173.00 kN Drift: 0.26%	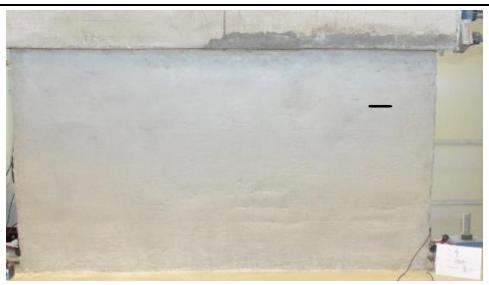	
	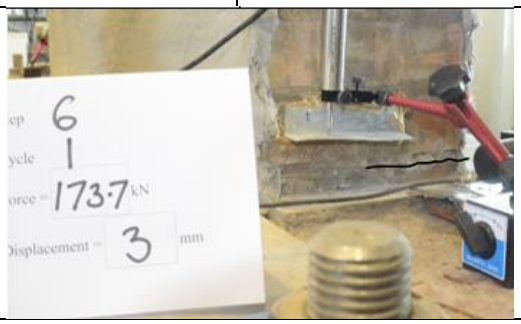	

Force: 228.95 kN Drift: 0.42%		
Force: 265.50 kN Drift: 0.67%	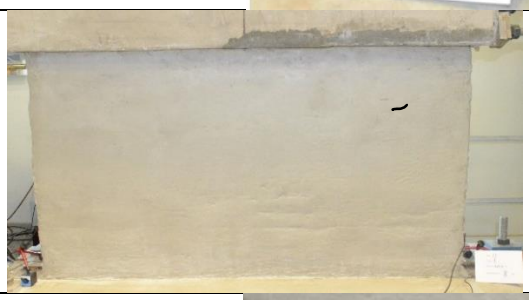	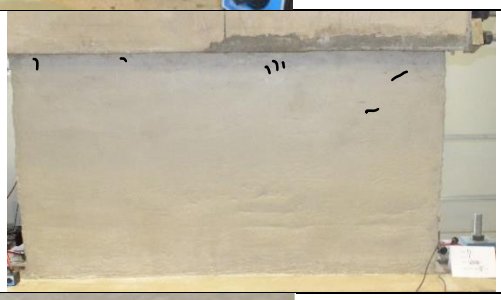
Force: 232.15 kN Drift: 1.34%		

<table>
<tr><td></td><td colspan="2">

</td></tr>
<tr><td rowspan="2">Force:
+214.8kN

Drift:
1.85%</td><td> </td><td rowspan="2">
</td></tr>
<tr><td> </td></tr>
<tr><td colspan="2">
</td></tr>
</table>

4.4 Flexural failure

Measurements from the string potentiometers 3 & 4 fixed at both sides of the wall specimens as displayed in Figure 3.20 from the instrumentation setup measured the uplifts (vertical displacements) experienced by the walls at both sides with uplift at the west and east side denoted as wall uplift$_1$ and wall uplift$_2$ respectively. Figure 4.12 illustrates the wall uplifts of URW, RW-1, and RW-2 respectively. URW was able to attain a maximum wall uplift of approximately 5 mm and 7.5 mm before the ultimate failure of the wall specimens for the negative and positive loading directions respectively. RW-1 and RW-2 attained wall uplifts of approximately 6 mm, 19.5 mm, and 11 mm, 18 mm for the negative and positive loading directions respectively.

(a)

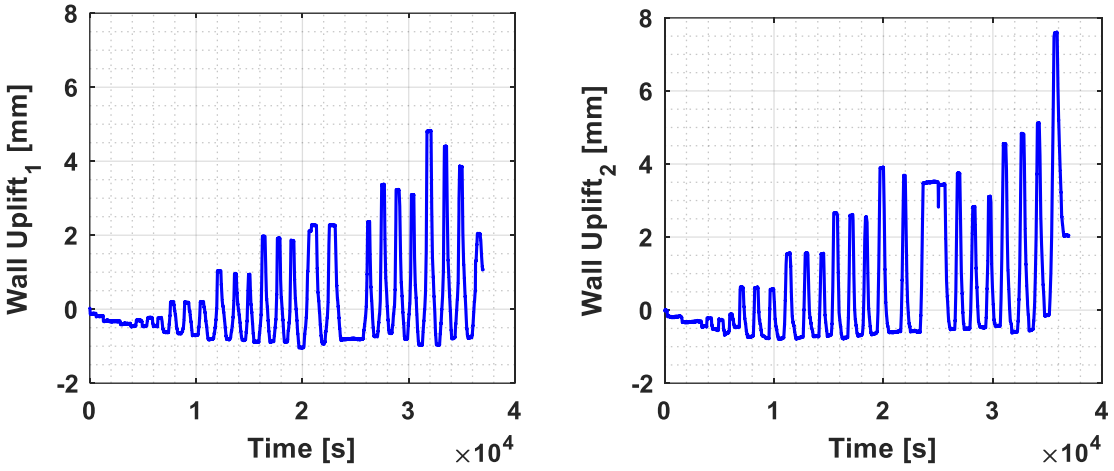

(b)

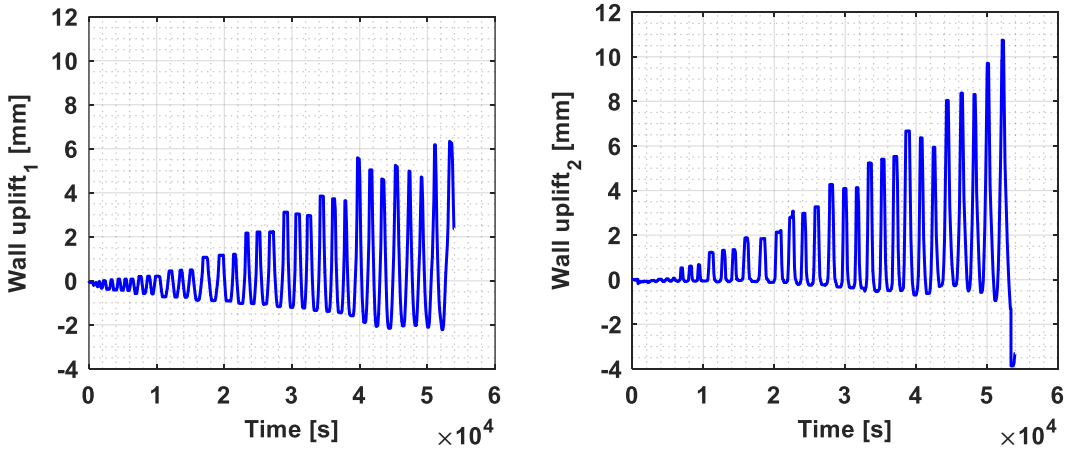

Note: Due to toe crushing which affected the LVDT at the wall toe, wall uplift for specimen RW-1 is only measured till 52000 secs

(c)

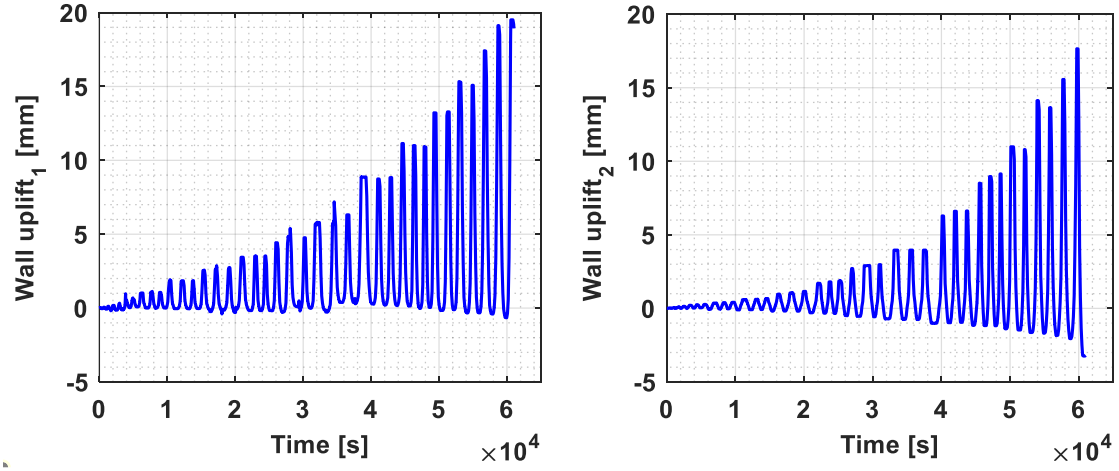

Figure 4.12: Wall uplifts-time graphs of wall specimens: (a) URW; (b) RW-1; (c) RW-2

Measurements from LVDTs 1 & 2 installed 80 mm above the bed joints of the wall specimens as shown in the instrumentation setup in Figure 3.20 measured the vertical uplifts at the wall toes with toes uplift at the west and east side denoted as Toe $uplift_1$ and Toe $uplift_2$ respectively. Figure 4.13 illustrates the toe uplifts of URW, RW-1, and RW-2 respectively. URW shows a negative uplift of 2 mm for toe $uplift_1$ indicating the presence of toe-crushing at the west part of the wall bed while toe $uplift_2$ shows a limited negative uplift signifying the non-occurrence of toe-crushing toward the east of the wall bed. RW-1 showed negative uplifts at both sides indicating the toe-crushing failure at both ends of the wall beds.

Using the uplifts results, the wall and toe rotations (θ) were determined following Equation 4.7 by dividing the difference between uplifts from both sides of each wall specimen by the length of the wall specimen. The rotation was calculated using both the wall and toe uplifts. The moment resistance M_R from the experiments was determined according to Equation 4.6 by multiplying the lateral force (F) applied to the wall specimen with the total height (h_w) of the wall specimen. All specimens were able to withstand approximately equal moments before failure, but RW-1 and RW-2 exhibited larger rotation capacities of an approximate average capacity of 100 % and 266.67 % respectively. This further confirms the ability of the LWECC retrofits used in the strengthening of the wall to improve the deformation capacity of URM walls.

$$M_R = F \times h_w \tag{4.6}$$

$$\theta = \frac{U_2 - U_1}{L} \tag{4.7}$$

Where, θ represents wall and toe rotations and U1 and U2 represent wall and toe uplifts at the west and east of the walls respectively, and L represents the length of wall specimens.

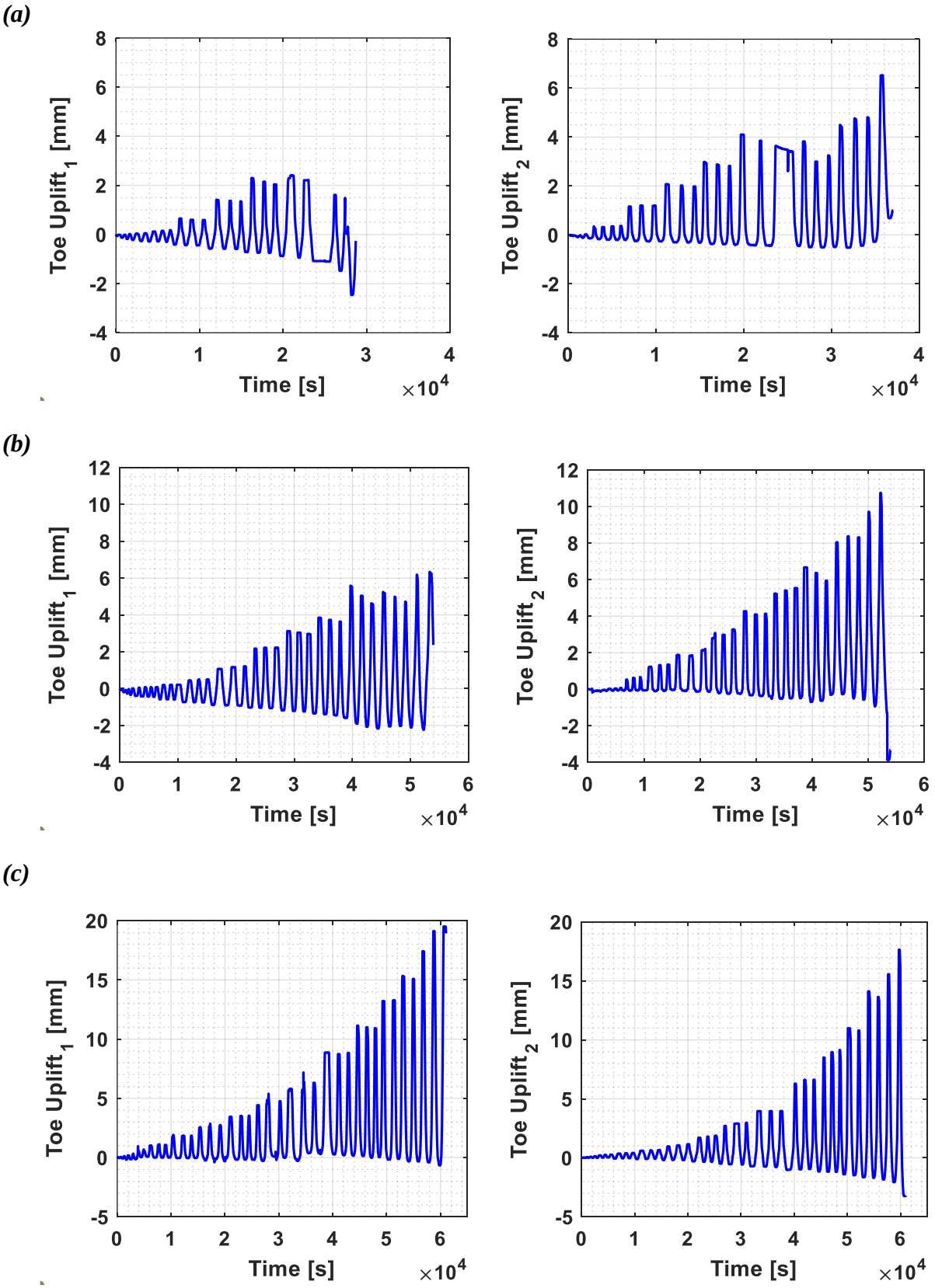

Figure 4.13: Toes uplifts-time graphs of wall specimens: (a) URW; (b) RW-1; (c) RW-2

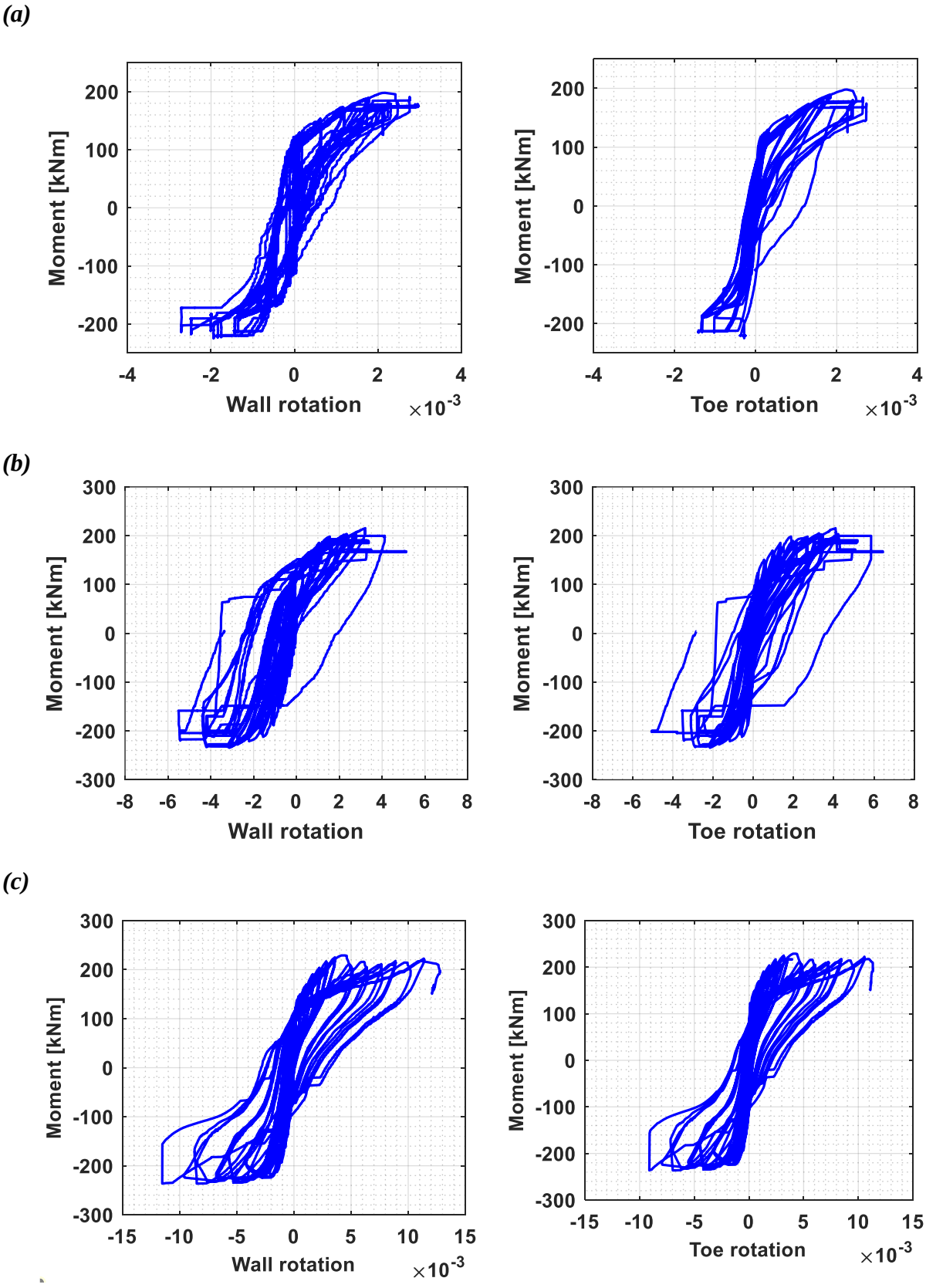

Figure 4.14: Moment vs. rotation graphs for wall specimens: (a) URW; (b) RW-1; (c) RW-2

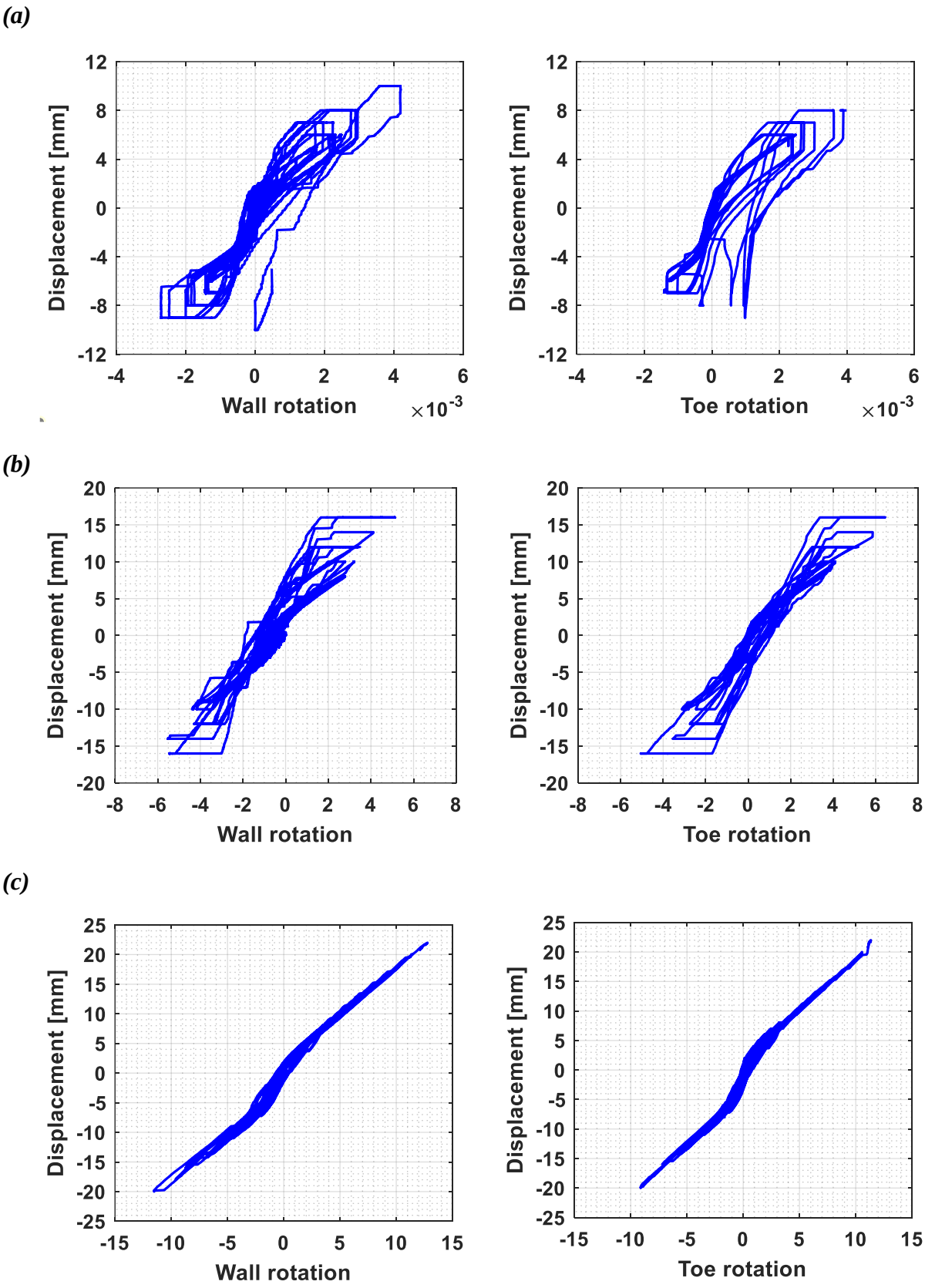

Figure 4.15: Displacement vs. rotation graphs for specimens: (a) URW; (b) RW-1; (c) RW-2

Figure 4.15 indicates the influence of the different failure modes experienced by the wall specimens. URW having large and sudden rotations after the displacement at which the wall experienced its maximum lateral load (6mm) indicates sudden failures resulting from large changes in the relative height of the wall at both sides due to lifts and toe crushing of the wall. Sudden drops in displacement are also observed, indicating the presence of sliding within the wall as was shown in section 4.3 with the wall moving out-of-plane. RW-1 (Figure 4.15b) showed large changes in the rotation due to the presence of rocking failure from wall uplifts and toe-crushing failure on both sides of the wall but the presence of the LWECC retrofit was able to prevent these failures till the point when 10mm displacement-loading was applied to the wall. RW-2 (Figure 4.15c) showed no sudden change in rotation at any applied displacement loading with a uniform displacement-rotation slope, indicating a pure rocking failure mode experienced by the wall. No sudden drop in displacement is observed at each rotation confirming that the retrofitting of the wall prevented any form of sliding of the wall.

RW-1 showed less rotation at each displacement compared to URM verifying the limited rocking behavior of the wall while RW-2 showed larger rotation verifying the concentrated rocking behavior of the wall.

4.5 Shear deformation

To probe for the shear deformation of the wall specimens, a graphical representation of the shear stress vs shear strain relationship is presented as shown in Figure 4.16. Shear stress, τ and shear strain, γ^2 experienced by the wall were calculated according to Equations 4.8 respectively. The calculation for the shear strain was done using information gotten from the string potentiometer 1 & 2 installed diagonally to the wall specimens.

$$\tau = \frac{F}{A_s} \tag{4.8a}$$

$$\gamma_i{}^2 = \alpha_i - \alpha_0 \tag{4.8b}$$

$$\alpha = \cos^{-1}\left(\frac{H^2 + W^2 - L^2}{2 \times H \times W}\right) \tag{4.8c}$$

Where F denotes the lateral force applied to the wall at the time of shear stress determination, A_s is the surface area of load application, H represents the difference in height

between the string potentiometers, W denotes the horizontal length of the string potentiometers, and L is the diagonal length of the string potentiometers. H, W, and L are all determined at each time of lateral load application representing the change in the deformation of the wall.

RW-1 showed more shear deformation compared to other walls due to the presence of diagonal shear stresses that created more spread-out shear cracks across the wall. RW-2 had more shear deformation compared to URM from a few shear cracks shown on the wall but less than RW-1 due to the rocking failure experienced by the wall.

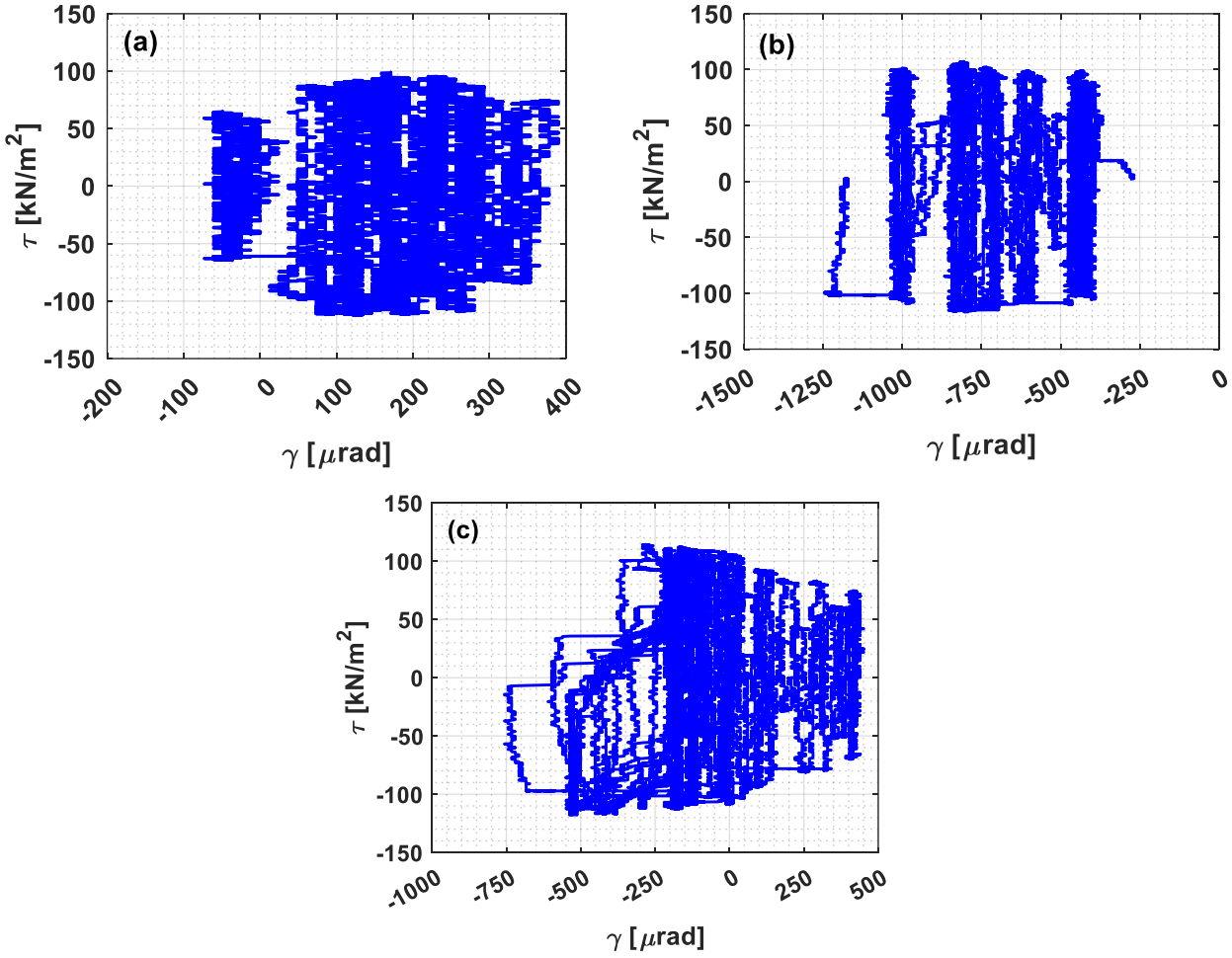

Figure 4.16: Shear stress vs. shear deformation graph: (a) URW; (b) RW-1; (c) RW-2

4.6 Stiffness Degradation

Stiffness degradation is a crucial measure needed for assessing masonry walls' cyclic response and seismic performance. Masonry is an inelastic structural material and does not exhibit

elastic behavior, even when subjected to minor deformations. However, the masonry walls' stiffness was practically defined as the slope of the first cycles of the hysteresis loop, calculated as the ratio of lateral loads to displacements.

With the degree of stiffness degradation dependent on the damage of the wall specimens, the secant stiffness k_{s_i} for each cycle of the wall specimens was estimated with the intention of analyzing the development of damage during loading. According to the relationship in Equation 4.9, the secant stiffness at each loading cycle, k_{s_i} was determined.

$$k_{s_i} = \frac{(|+F_i|+|-F_i|)}{(|+\Delta_i|+|-\Delta_i|)} \tag{4.9}$$

where $\pm F_i$ represents the positive and negative peak lateral force of the first cycle of the i_{th} loop and $\pm\Delta_i$ denotes the equivalent displacement under the i_{th} loop. The relative secant stiffness, calculated as the ratio of the secant stiffness to the initial secant stiffness was derived also using the lateral secant stiffness. Figure 4.17 shows the wall stiffness and relative secant stiffness at each displacement level.

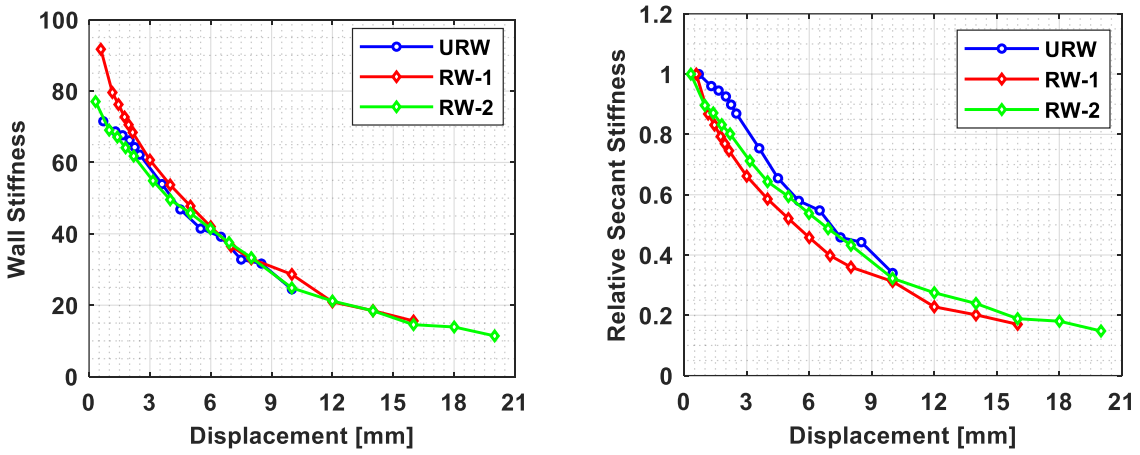

(a) ***(b)***

Figure 4.17: (a) Stiffness curves of wall specimens; (b) Relative secant stiffness curves of wall specimens

Figure 4.17a show higher stiffness for RW-1 and RW-2 than URW at their corresponding displacement with the retrofitted specimens being able to reach lower stiffness before failure. RW-1 had higher initial stiffness, increasing the wall's resistance to the flexural stresses generated at

the bottom of the walls, resulting in the creation of distributed shear stress across the wall. Figure 4.17b which represents the stiffness degradation of each wall specimen indicating that RW-1 and RW-2 had a lower reduction in stiffness at the same displacement, invariably causing an increase in the displacement capacity. The reduced rate of stiffness degradation for the retrofitted specimens resulted from the ductile properties of the applied LWECC overlays improving the strain capacities of the walls according to the stain capacities of its overlays.

Figure 4.17 showed that URW had lower initial stiffness with higher degradation of the stiffness which resulted in the sudden failure of the wall. The retrofitted wall specimens had higher initial stiffness with low stiffness degradation due to the application of LWECC which improved the ductility and displacement capacity before the ultimate failure of the wall even at lower stiffness. Despite RW-1 having higher initial stiffness due to the higher strength of its LWECC retrofit, RW-2 had lower stiffness degradation which resulted in the specimen having more displacement capacity than RW-1. It confirms the approach of retrofitting URM walls with LWECC is effective in preventing the sudden failure of URM walls even at extremely low stiffness, decelerating the rate of damage to the walls.

4.7 Energy dissipation capacity

The walls' ability to dissipate energy is an essential parameter in evaluating their seismic performance by calculating the cumulative energy dissipation in the first loop of each displacement loading cycle of the hysteresis curves. The energy dissipation is the ratio of the area enclosed by the hysteresis loop (E_D) loop created for each first cycle to the input energy (the horizontal distance moved by the horizontal actuator from the positive to the negative applied displacement) as shown in Figure 4.18a.

The cumulative dissipated energy of all wall specimens is shown in Figure 4.18b. All wall specimens displayed similar energy dissipation at the initial stage of cyclic loading before the occurrence of any form of failure. The control wall specimen displayed superior energy dissipation capacity at corresponding displacement to the retrofitted walls after the control wall attained peak lateral force while the retrofitted walls experienced lower energy dissipation compared to URW due to LWECC overlay absorbing part of the stresses witnessed by the walls.

This results from URM walls being able to dissipate more energy through the occurrence of significant damage caused by shear-induced failures like the rocking and toe-crushing failure which occurred in the control wall specimen, whereas the retrofitted wall specimens only generated slightly distributed damages across the walls which was limited to toe crushing and rocking failures for specimens RW-1 and RW-2 respectively.

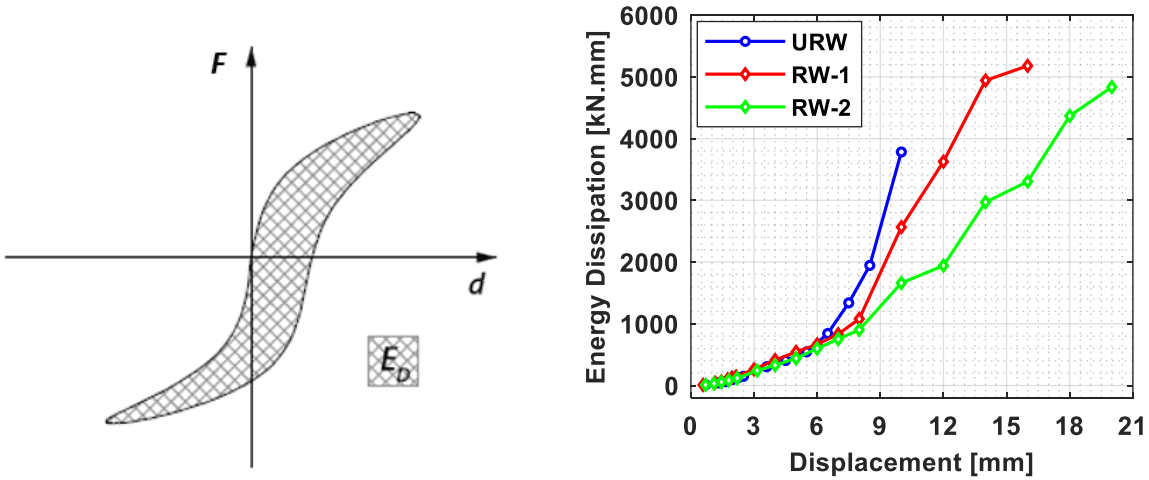

(a) *(b)*

Figure 4.18: (a) Schematic diagram on the determination of dissipated energy; (b) Cumulative energy dissipation curves of wall specimens

RW-1 showed more energy dissipation as compared to RW-2 due to the spread-out damage cracks observed across the wall's body. RW-2 showed the least energy dissipation resulting from rocking failure experienced by the wall with the wall rotating about its toes.

The cumulated energy dissipation of RW-2 was lower than that of RW-1 at the same displacement and increased much more slowly due to RW-1 having its damage spread out more evenly over the wall's body while RW-2 had concentrated rocking damage. This can be attributed to the combined rocking and toes-crushing failures of the RW-1 and the flexural-dominated rocking failure mode of the RW-2, resulting from RF-5 being able to absorb more shear force to achieve larger displacements before failure. These results suggested that the energy dissipation capacity of the specimens is related to the failure modes.

Chapter 5: Conclusions and Recommendations

5.1 Conclusions

Masonry buildings across history have been one of the most seismically vulnerable structures. Considering the severe damage from earthquakes, researchers are studying varying retrofitting techniques to prevent the negative consequences of seismic occurrences. This study presents the technique of retrofitting URM walls against seismic load through the trowelling of 15 mm thick layers of LWECC on both surfaces of the masonry when subjected to in-plane cyclic loads. Chapters 1 and 2 highlight how URM walls have poor performance to shear loads especially those created by seismic activities, and this can be significantly enhanced using appropriate retrofitting material and methods. Large consideration is placed on the use of LWECC layers for strengthening URM walls in a typical masonry residential building against in-plane actions resulting from earthquake loads to earthquake loads.

LWECC was chosen as a promising retrofitting composite due to its high tensile strain-hardening properties capable of significantly improving the ductile performance of URM walls due to its lower stiffness when compared to normal-weight engineered cementitious composite. An additional benefit of the use of LWECC is its multifunctional features which include lightweight, low thermal conductivity, and high sound absorption ability. The LWECC design used in this project was selected from the literature to include two mixes of high-strength and low-strength LWECC whose results were presented in Chapter 3. The LWECC was used to strengthen two URM walls subjected to in-plane cyclic tests and compared to a plane URM control wall. The behavior of a series of 0.55 aspect ratio masonry wall specimens retrofitted using one 15 mm thick LWECC layer on each of both faces of the wall specimens was investigated experimentally and presented in Chapter 4. The following findings are drawn from the retrofitting of the URM walls with the LWECC:

- The failure of the URW initiated with rocking, followed by damage at the toes. In-plane sliding was observed near the toe region at a large wall drift. This sliding also causes out-of-plane instability and failure of the wall.

- Trowelling of the LWECC on both faces of the URM wall prevented toe sliding and out-of-plane instability. Therefore, the wall can undergo more drift without significant strength reduction and becomes more ductile.
- When the strength of applied LWECC is as low as 11 MPa, the wall exhibited similar rocking behavior as the URW, followed by toe damages at a much larger drift.
- For the wall retrofitted with a higher strength (28MPa) LWECC, the rocking is limited by the higher tensile strength of the LWECC. More spread-out damage cracks were observed across the wall's body, which indicates a mixed diagonal shear and rocking behavior. Although this behavior has a lower deformation capacity of the wall, it shows much more plastic response and energy dissipation as compared to the wall retrofitted with the lower strength LWECC.
- The LWECC showed good bonding with the URM wall with the material fully bonded to the walls during and after the wall testing.
- The LWECC retrofitting was only applied to the wall surface without proper anchoring to the foundation since it was not feasible to realize. Therefore, the strength of the retrofitted walls has only a slight increase as compared to the URW.
- The LWECC reinforced wall specimens indicated a considerable increase in the ductility capacity ranging between 123.58% - 180.24% for RW-1 with the higher strength LWECC and 151.99% - 150.37% for RW-2 retrofitted with lower strength LWECC.
- The application of the LWECC overlay allowed for an average increase of 69.78% and 122.78% in the ultimate displacement capacity of the walls retrofitted with the higher and lower strength LWECC respectively. The increase in displacement capacity resulted from the walls being able to undergo more displacement-controlled loading before failure. For URW, it was able to attain its ultimate load capacity at an average displacement of 9.58 mm (0.8% drift). RW-1 reached an average displacement of 15.85 mm (1.32% drift) before ultimate failure. RW-2, experienced ultimate failure at an average displacement of 20.37 mm (1.7% drift).
- The increase in the ultimate lateral load-carrying capacity was less considerable, achieving an increase in wall shear capacity within 5.60% - 14.69% when each retrofitted masonry wall was strengthened with RF-1 and RF-5 LWECC samples.

- RW-1 and RW-2 respectively had increased initial wall stiffness compared to URW by average values of 58.44% and 24.45%. Relative stiffness degradation comparison among the wall specimens shows high degradation for the un-retrofitted wall confirming the brittle nature of URM walls while the application of LWECC (with good ductile properties) to the walls increased the ductility of the walls resulting in a reduced rate of stiffness degradation. The increased initial stiffness and reduced rate of stiffness degradation of the retrofitted wall specimens showed good effectiveness in improving the displacement and ductility capacities of the masonry walls.

Overall, the experimental results show that lightweight engineered cementitious composites can significantly enhance the ductility, deformation, and displacement capacity of the wall, resulting in better seismic performance.

5.2 Recommendations for further research

Consideration should be made to test for the performance of LWECC to shear-dominated failure modes such as diagonal shear failure by developing wall specimens with other aspect ratios and axial load combinations. Setup can be made to have adequate anchoring of the LWECC overly into the foundation to test for improved performance of the retrofit to resist flexural stresses at the wall's base, also improving the shear strength capacity. LWECC can also be considered as a seismic retrofitting material for other structural elements such as slabs and columns. Lastly, a study on the seismic performance of URM walls retrofitted with green LWECC developed from sustainable industrial byproducts is vital to also have an eco-friendlier retrofitting technique.

Bibliography/References

[1] K. Mosalam, L. Glascoe, and J. Bernier, “Mechanical Properties of Unreinforced Brick Masonry, Section1,” Lawrence Livermore National Lab.(LLNL), Livermore, CA (United States), 2009.

[2] J. A. Dauda, “Numerical and experimental investigation of unreinforced masonry wall retrofitted with timber panels,” 2020.

[3] G. Barbieri, L. Biolzi, M. Bocciarelli, L. Fregonese, and A. Frigeri, “Assessing the seismic vulnerability of a historical building,” *Engineering Structures*, vol. 57, pp. 523–535, Dec. 2013, doi: 10.1016/j.engstruct.2013.09.045.

[4] F. Wei, Y. Zhu, J. Yu, and Y. Wang, “Experimental study of seismic behaviour of renovated masonry structures after removing walls and seismic retrofitting,” *Journal of Building Engineering*, vol. 31, p. 101360, 2020, doi: https://doi.org/10.1016/j.jobe.2020.101360.

[5] S. M. Renuka and I. P. Mervin Sanjith, “Strengthening of Damaged Masonry Walls Using Engineered Cementitious Composites: Experimental and Numerical Analysis,” *Advances in Civil Engineering*, vol. 2022, p. 6343179, May 2022, doi: 10.1155/2022/6343179.

[6] L. Gambarotta and S. Lagomarsino, “Damage models for the seismic response of brick masonry shear walls. Part I: the mortar joint model and its applications,” *Earthquake engineering & structural dynamics*, vol. 26, no. 4, pp. 423–439, 1997.

[7] C. G. Papanicolaou, T. C. Triantafillou, K. Karlos, and M. Papathanasiou, “Textile-reinforced mortar (TRM) versus FRP as strengthening material of URM walls: in-plane cyclic loading,” *Materials and Structures*, vol. 40, no. 10, pp. 1081–1097, Dec. 2007, doi: 10.1617/s11527-006-9207-8.

[8] N. Ismail and J. M. Ingham, “In-plane and out-of-plane testing of unreinforced masonry walls strengthened using polymer textile reinforced mortar,” *Engineering Structures*, vol. 118, pp. 167–177, 2016, doi: https://doi.org/10.1016/j.engstruct.2016.03.041.

[9] C. Faella, E. Martinelli, E. Nigro, and S. Paciello, “Shear capacity of masonry walls externally strengthened by a cement-based composite material: An experimental campaign,” *Construction and Building Materials*, vol. 24, no. 1, pp. 84–93, 2010, doi: https://doi.org/10.1016/j.conbuildmat.2009.08.019.

[10] H. Mahmood and J. M. Ingham, “Seismic Vulnerability Assessment of Pakistan Unreinforced Masonry Buildings at a National Scale,” *Seismological Research Letters*, vol. 82, pp. 676–685, 2011.

[11] M. R. Valluzzi, D. Tinazzi, and C. Modena, “Shear behavior of masonry panels strengthened by FRP laminates,” *Construction and Building Materials*, vol. 16, no. 7, pp. 409–416, Oct. 2002, doi: 10.1016/S0950-0618(02)00043-0.

[12] T. C. Triantafillou, “Strengthening of Masonry Structures Using Epoxy-Bonded FRP Laminates,” *J. Compos. Constr.*, vol. 2, no. 2, pp. 96–104, May 1998, doi: 10.1061/(ASCE)1090-0268(1998)2:2(96).

[13] M. ElGawady, P. Lestuzzi, and M. Badoux, “Retrofitting of masonry walls using shotcrete,” presented at the 2006 NZSEE Conference, Paper, 2006.

[14] Y.-W. Lin, L. Wotherspoon, A. Scott, and J. M. Ingham, “In-plane strengthening of clay brick unreinforced masonry wallettes using ECC shotcrete,” *Engineering Structures*, vol. 66, pp. 57–65, May 2014, doi: 10.1016/j.engstruct.2014.01.043.

[15] S. Soleimani-Dashtaki, C. E. Ventura, and N. Banthia, “Seismic Strengthening of Unreinforced Masonry Walls using Sprayable Eco-Friendly Ductile Cementitious Composite (EDCC),” *Procedia Engineering*, vol. 210, pp. 154–164, Jan. 2017, doi: 10.1016/j.proeng.2017.11.061.

[16] S. M. Dehghan, M. A. Najafgholipour, A. R. Kamrava, and M. Khajepour, “Application of Ordinary Fiber-Reinforced Concrete Layer for In-plane Retrofitting of Unreinforced Masonry Walls: Test and Modeling,” *Scientia Iranica*, vol. 0, no. 0, pp. 0–0, Jan. 2018, doi: 10.24200/sci.2018.20164.

[17] M. Deng, Z. Dong, and P. Ma, “Cyclic loading tests of flexural-failure dominant URM walls strengthened with engineered cementitious composite,” *Engineering Structures*, vol. 194, pp. 173–182, Sep. 2019, doi: 10.1016/j.engstruct.2019.05.073.

[18] M. Deng and S. Yang, “Cyclic testing of unreinforced masonry walls retrofitted with engineered cementitious composites,” *Construction and Building Materials*, vol. 177, pp. 395–408, Jul. 2018, doi: 10.1016/j.conbuildmat.2018.05.132.

[19] P. Davy and P. Cobbold, “Indentation tectonics in nature and experiment. 1. Experiments scaled for gravity,” *Bull. Geol. Inst. Univ. Uppsala*, vol. 14, pp. 129–141, 1988.

[20] G. M. Calvi, G. R. Kingsley, and G. Magenes, “Testing of Masonry Structures for Seismic Assessment,” *Earthquake Spectra*, vol. 12, no. 1, pp. 145–162, Feb. 1996, doi: 10.1193/1.1585872.

[21] S. Gao, X. Zhao, J. Qiao, Y. Guo, and G. Hu, “Study on the bonding properties of Engineered Cementitious Composites (ECC) and existing concrete exposed to high temperature,” *Construction and Building Materials*, vol. 196, pp. 330–344, Jan. 2019, doi: 10.1016/j.conbuildmat.2018.11.136.

[22] L. S. Wijanto, “Seismic assessment of unreinforced masonry walls,” 2007.

[23] M. Tomaževič, “Shear resistance of masonry walls and Eurocode 6: shear versus tensile strength of masonry,” *Mater Struct*, vol. 42, no. 7, pp. 889–907, Aug. 2009, doi: 10.1617/s11527-008-9430-6.

[24] M. Tomaževič, *Earthquake-resistant Design of Masonry Buildings*. in Series on innovation in structures and construction. Imperial College Press, 1999. [Online]. Available: https://books.google.kz/books?id=uOhmaZWJ7wIC

[25] G. C. Manos, L. Melidis, L. Kotoulas, and K. Katakalos, “THE BEHAVIOR OF PARTIALLY GROUTED MASONRY WALLS SUBJECTED TO OUT OF PLANE SEISMIC TYPE LOADS. LABORATORY MEASUREMENTS AND NUMERICAL SIMULATIONS,” presented at the 8th International Conference on Computational Methods in Structural Dynamics and Earthquake Engineering Methods in Structural

Dynamics and Earthquake Engineering, Athens, Greece, Athens, Greece, 2021, pp. 2875–2884. doi: 10.7712/120121.8681.19495.

[26] Applied Technology Council and Partnership for Response, *Evaluation of earthquake damaged concrete and masonry wall buildings: Basic procedures manual*. The Agency, 1999.

[27] V. C. Li, "High performance fiber reinforced cementitious composites as durable material for concrete structure repair/Faser verstärkte, Zement gebundene, zusammen gesetzte Hochleistungswerkstoffe für das dauerhafte Instandsetzen von Betontragwerken," *Restoration of Buildings and Monuments*, vol. 10, no. 2, pp. 163–180, 2004.

[28] Y. Lin, D. Lawley, L. Wotherspoon, and J. M. Ingham, "Out-of-plane Testing of Unreinforced Masonry Walls Strengthened Using ECC Shotcrete," *Structures*, vol. 7, pp. 33–42, Aug. 2016, doi: 10.1016/j.istruc.2016.04.005.

[29] H.-K. Choi, B.-I. Bae, and C.-S. Choi, "Lateral Resistance of Unreinforced Masonry Walls Strengthened With Engineered Cementitious Composite," *Int J Civ Eng*, vol. 14, no. 6, Art. no. 6, Sep. 2016, doi: 10.1007/s40999-016-0026-1.

[30] V. W. J. Lin, S. T. Quek, M. P. Nguyen, and M. Maalej, "Strengthening of Masonry Walls Using Hybrid-fiber Engineered Cementitious Composite," *Journal of Composite Materials*, vol. 44, no. 8, Art. no. 8, Apr. 2010, doi: 10.1177/0021998309346186.

[31] Y.-W. Lin, D. Biggs, L. Wotherspoon, and J. M. Ingham, "In-Plane Strengthening of Unreinforced Concrete Masonry Wallettes Using ECC Shotcrete," *J. Struct. Eng.*, vol. 140, no. 11, Art. no. 11, Nov. 2014, doi: 10.1061/(ASCE)ST.1943-541X.0001004.

[32] A. Hanif, Z. Lu, Y. Cheng, S. Diao, and Z. Li, "Effects of different lightweight functional fillers for use in cementitious composites," *International Journal of Concrete Structures and Materials*, vol. 11, no. 1, pp. 99–113, 2017.

[33] F. Aslani, L. Wang, and M. Zheng, "The effect of carbon nanofibers on fresh and mechanical properties of lightweight engineered cementitious composite using hollow glass microspheres," *Journal of Composite Materials*, vol. 53, no. 17, pp. 2447–2464, 2019.

[34] V. C. Li, "Tailoring ECC for Special Attributes: A Review," *Int J Concr Struct Mater*, vol. 6, no. 3, Art. no. 3, Sep. 2012, doi: 10.1007/s40069-012-0018-8.

[35] S. Wang and V. Li, "27 Lightweight engineered cementitious composites (ECC)," presented at the PRO 30: 4th international RILEM workshop on high performance fiber reinforced cement composites (HPFRCC 4), RILEM Publications Michigan, 2003, p. 379.

[36] S. B. Keskin, K. Sulaiman, M. Sahmaran, and I. O. Yaman, "Effect of presoaked expanded perlite aggregate on the dimensional stability and mechanical properties of engineered cementitious composites," *Journal of materials in civil engineering*, vol. 25, no. 6, pp. 763–771, 2013.

[37] B. Nematollahi, R. Ranade, J. Sanjayan, and S. Ramakrishnan, "Thermal and mechanical properties of sustainable lightweight strain hardening geopolymer composites," *Archives of Civil and Mechanical Engineering*, vol. 17, no. 1, pp. 55–64, 2017.

[38] X. Huang, R. Ranade, Q. Zhang, W. Ni, and V. C. Li, “Mechanical and thermal properties of green lightweight engineered cementitious composites,” *Construction and Building Materials*, vol. 48, pp. 954–960, 2013.

[39] Y. Zhou, B. Xi, L. Sui, S. Zheng, F. Xing, and L. Li, “Development of high strain-hardening lightweight engineered cementitious composites: Design and performance,” *Cement and Concrete Composites*, vol. 104, p. 103370, 2019.

[40] Q. Jin and V. C. Li, “Development of lightweight engineered cementitious composite for durability enhancement of tall concrete wind towers,” *Cement and Concrete Composites*, vol. 96, pp. 87–94, 2019.

[41] C15 Committee, “Test Methods for Sampling and Testing Brick and Structural Clay Tile,” ASTM International. doi: 10.1520/C0067_C0067M-21.

[42] H. Zhu, K. T. Wan, E. Satekenova, D. Zhang, C. K. Y. Leung, and J. Kim, “Development of lightweight strain hardening cementitious composite for structural retrofit and energy efficiency improvement of unreinforced masonry housings,” *Construction and Building Materials*, vol. 167, pp. 791–812, Apr. 2018, doi: 10.1016/j.conbuildmat.2018.02.033.

[43] C09 Committee, “Test Method for Compressive Strength of Cylindrical Concrete Specimens,” ASTM International. doi: 10.1520/C0039_C0039M-21.

[44] A. H. Salmanpour, N. Mojsilović, and J. Schwartz, “Displacement capacity of contemporary unreinforced masonry walls: An experimental study,” *Engineering Structures*, vol. 89, pp. 1–16, Apr. 2015, doi: 10.1016/j.engstruct.2015.01.052.

Appendices

Appendix A

Figure A.1: Deformation history of URW wall specimen

	Positive cycles	Negative cycles
Force: 40kN 0% drift	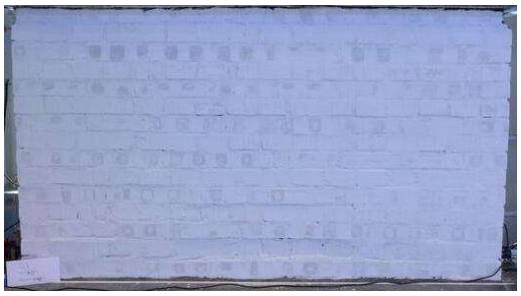	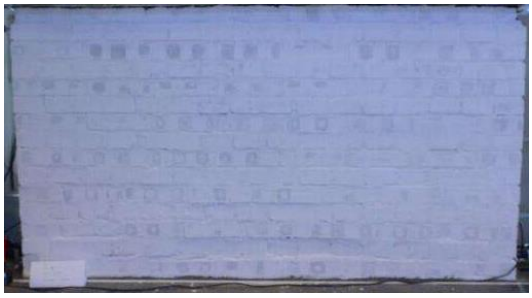
Force: 143.05 kN Drift: 0.15%	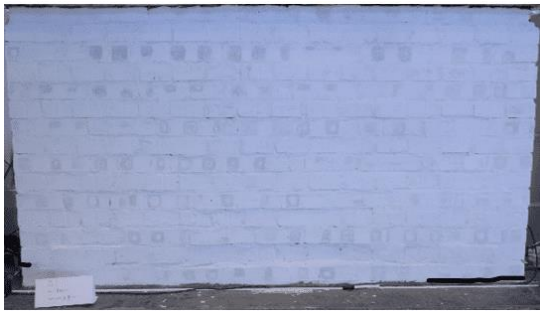	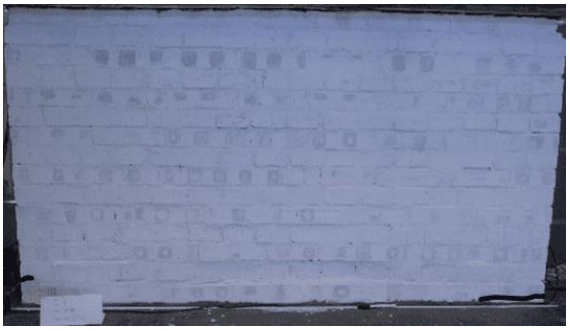
Force: 154.45 Drift: 0.17%	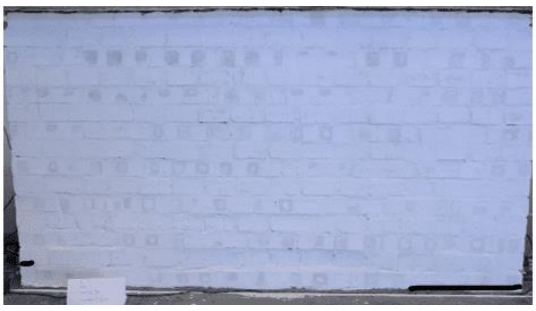	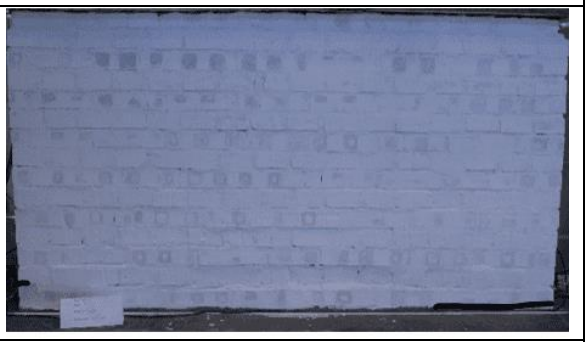
Force: 193.25 kN Drift: 0.25%	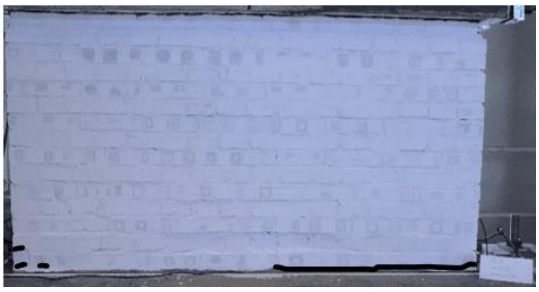	

<table>
<tr><td></td><td> </td></tr>
<tr><td rowspan="2">Force:
210.05 kN

Drift:
3.33%</td><td> 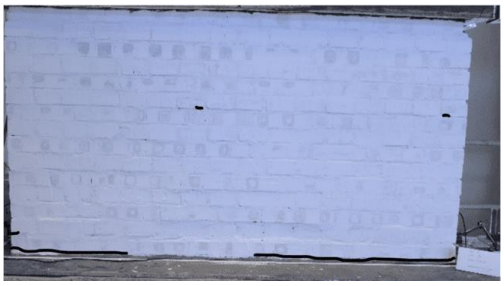 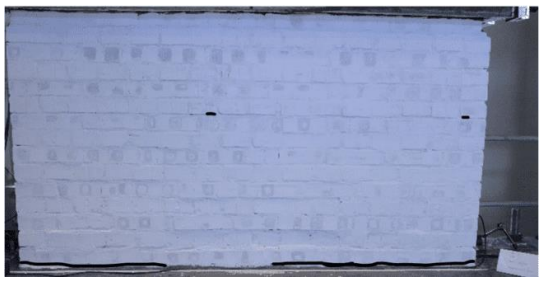 </td></tr>
<tr><td> </td></tr>
<tr><td rowspan="2">Force:
227.8 kN

Drift:
0.42%</td><td> 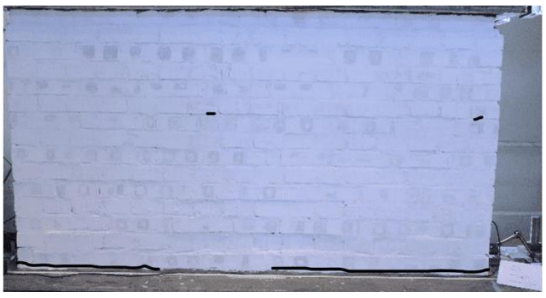 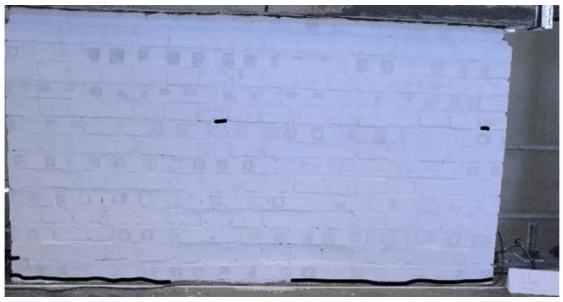 </td></tr>
<tr><td> </td></tr>
</table>

Force: 217.95 kN Drift: 0.50%	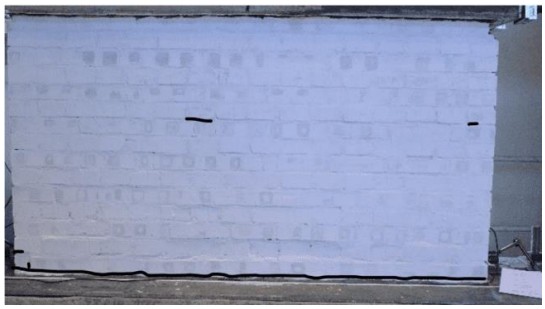 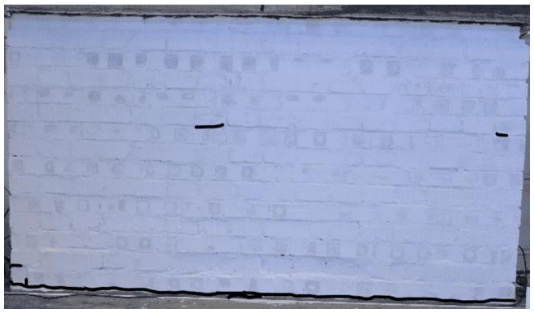 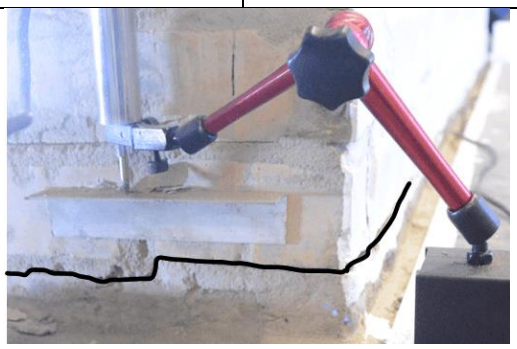
Force: 244.6 kN Drift: 0.58%	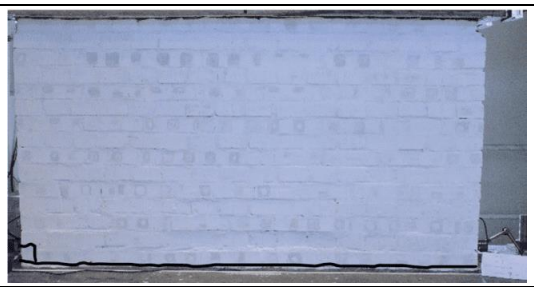 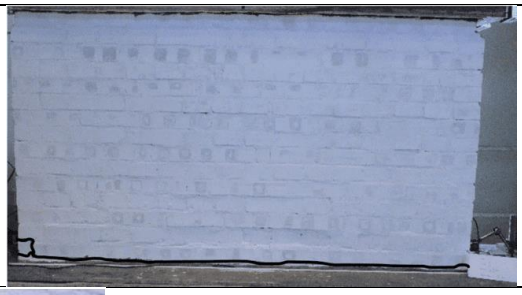 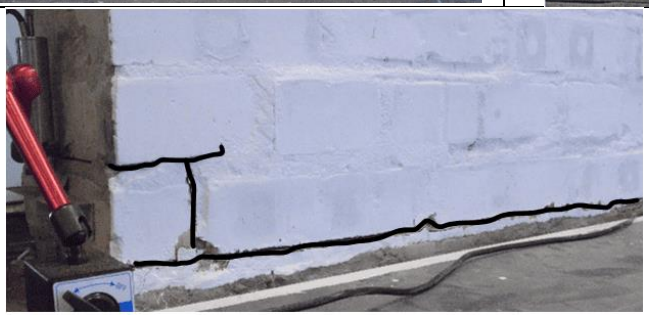
Force: 248.2 kN Drift: 0.67%	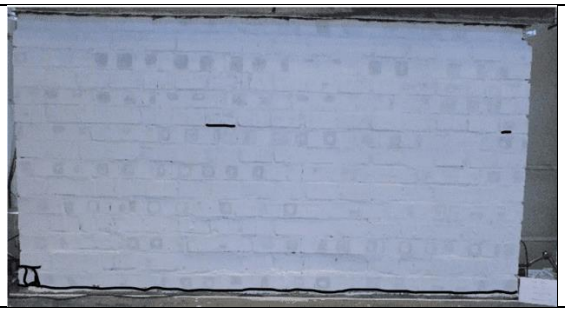 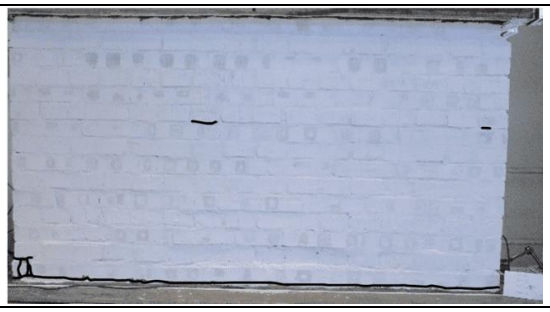

Force: 207.5 Drift: 0.83%	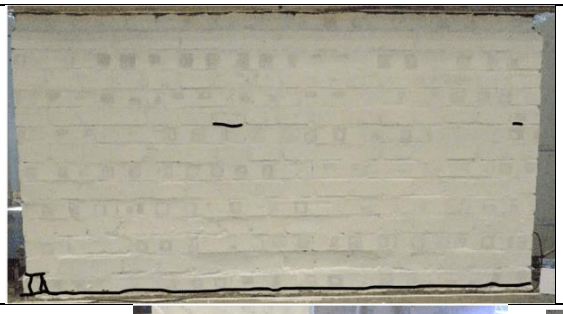 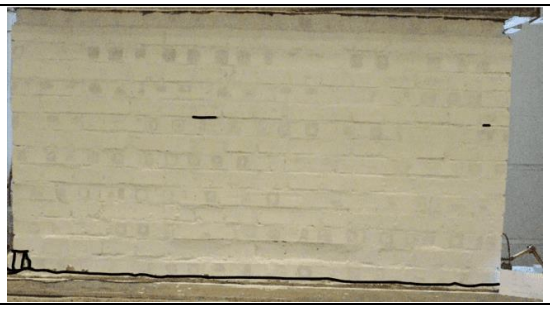

Figure A.2: Deformation history of RW-1 wall specimen

	Positive cycles	**Negative cycles**
Force: 40kN 0% drift		
Force: 182.00 kN Drift: 0.25%		
Force: 214.70 kN Drift: 0.33%		
Force: 233.30 kN Drift: 0.42%		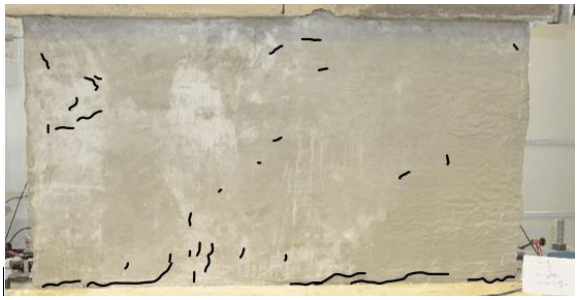
Force: 251.65 kN Drift: 0.50%	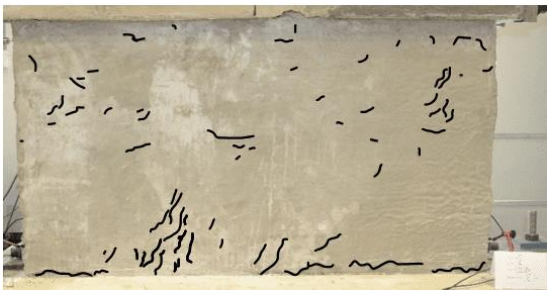	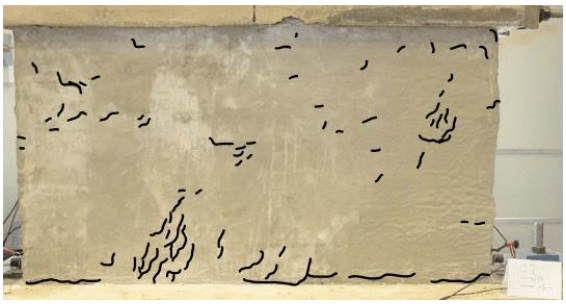

	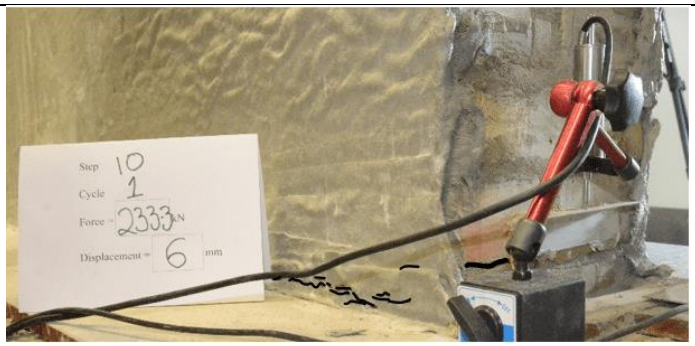
Force: 255.45 kN Drift: 0.58%	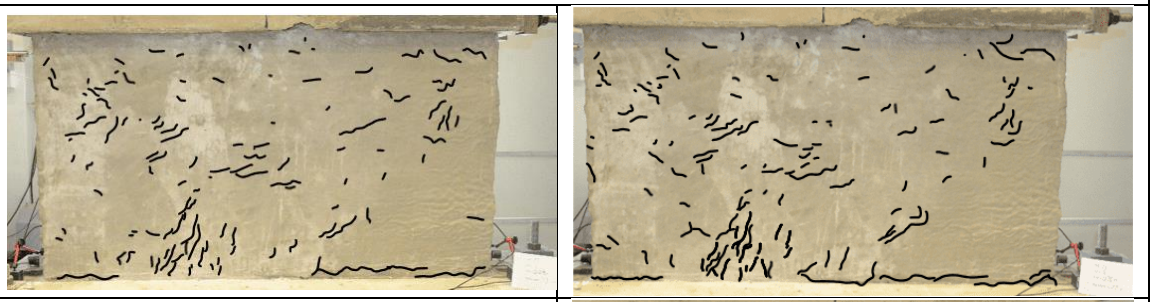
Force: 263.95 kN Drift: 0.67%	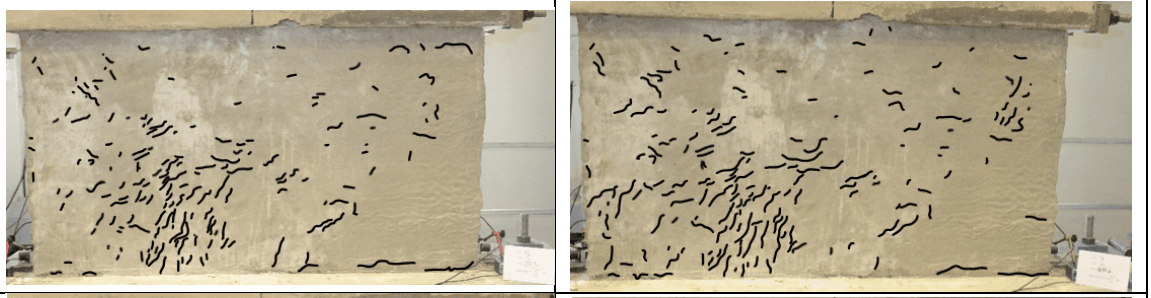
Force: 233.30 kN Drift: 0.83%	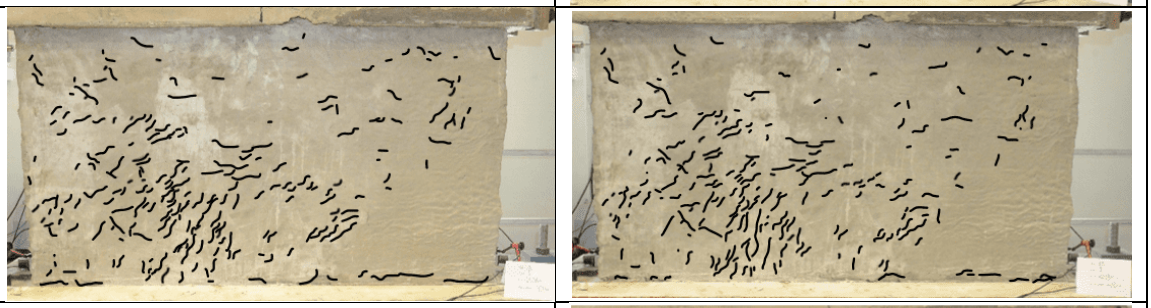
Force: 232.90 kN Drift: 1.00%	

<table>
<tr><td></td><td> </td></tr>
<tr><td>Force:
216.80 kN

Drift:
1.17%</td><td> </td></tr>
<tr><td>Force:
223.70 kN

Drift:
1.33%</td><td> 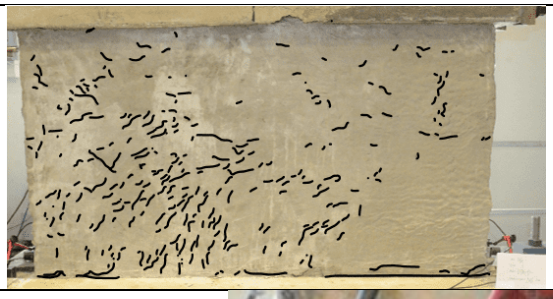 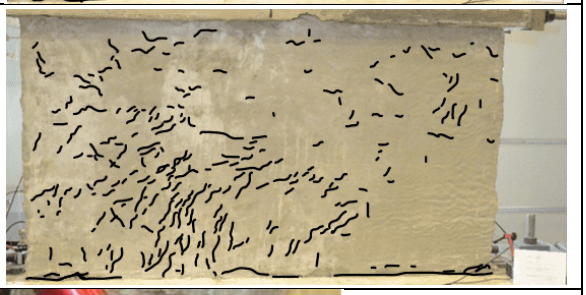 </td></tr>
</table>

Figure A.3: Deformation history of RW-2 wall specimen

	Positive cycles	Negative cycles
Force: 40kN 0% drift		
Force: 173.00 kN Drift: 0.26%	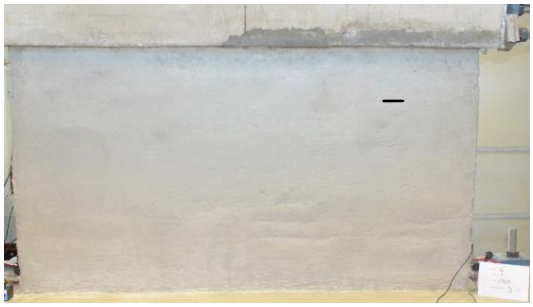	
	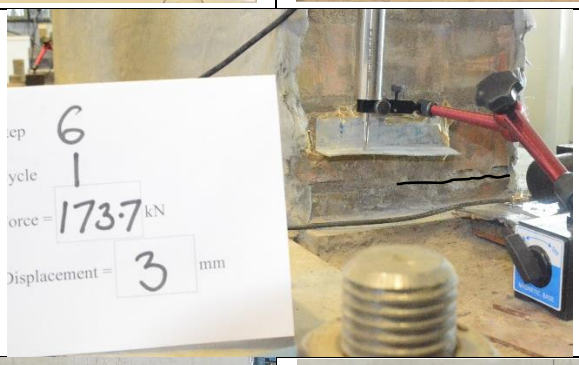	
Force: 198.05 kN Drift: 0.34%		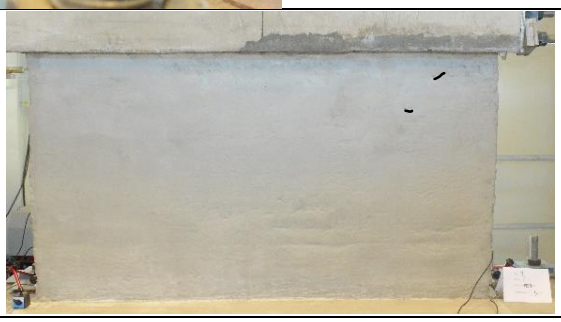
Force: 228.95 kN Drift: 0.42%		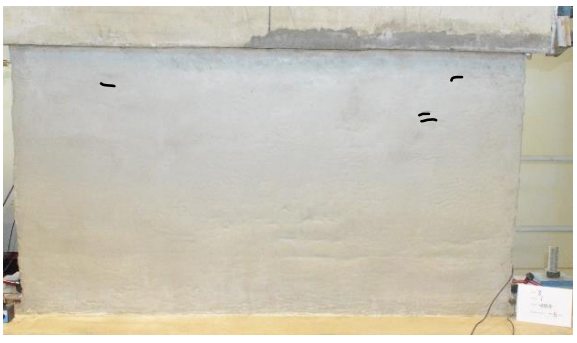

<table>
<tr><td></td><td colspan="2"> 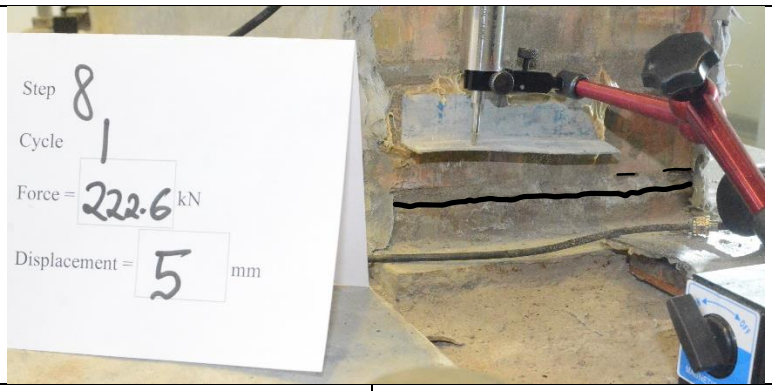
</td></tr>
<tr><td>Force:
247.75 kN

Drift:
0.50%</td><td> </td><td> 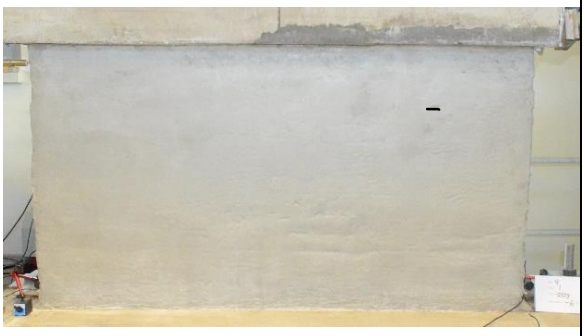 </td></tr>
<tr><td rowspan="2">Force:
259.30 kN

Drift:
0.59%</td><td> 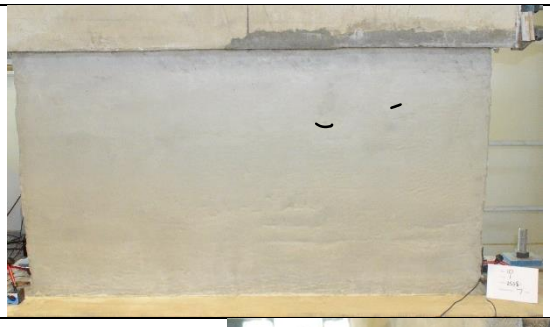 </td><td> 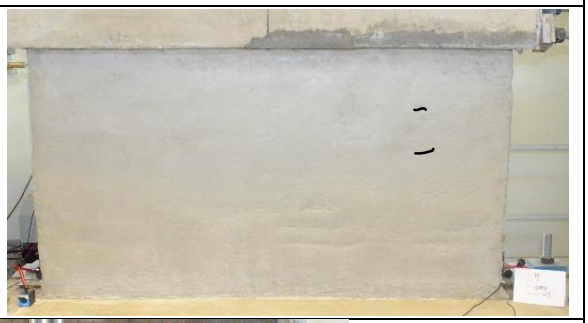 </td></tr>
<tr><td colspan="2">
</td></tr>
</table>

Force: 265.50 kN Drift: 0.67%	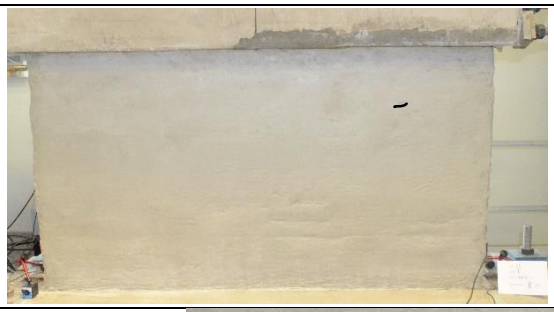 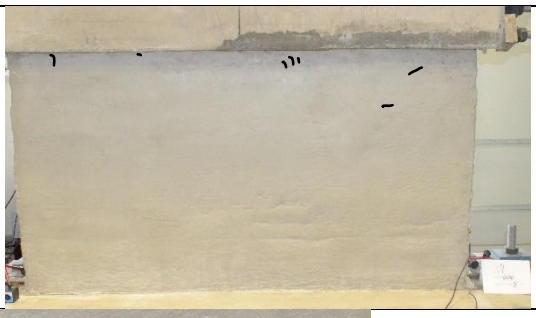 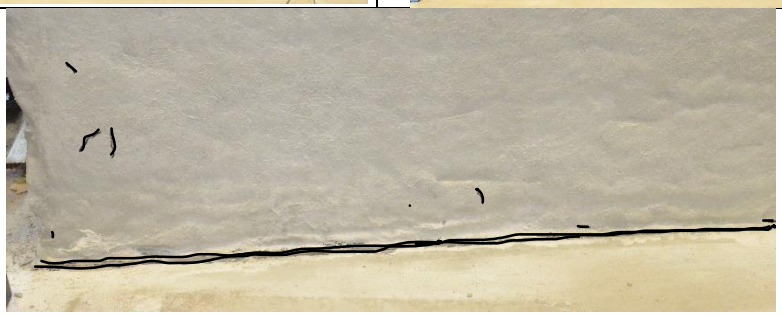
Force: 248.45 kN Drift: 0.84%	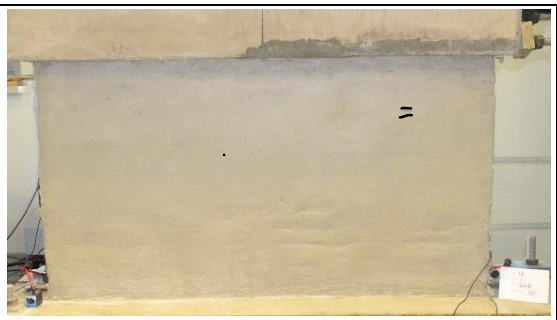 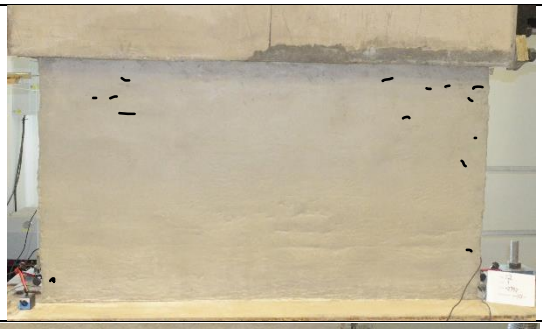 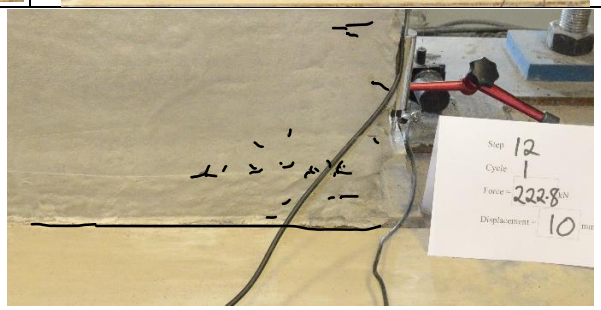
Force: 253.85kN Drift: 1.01%	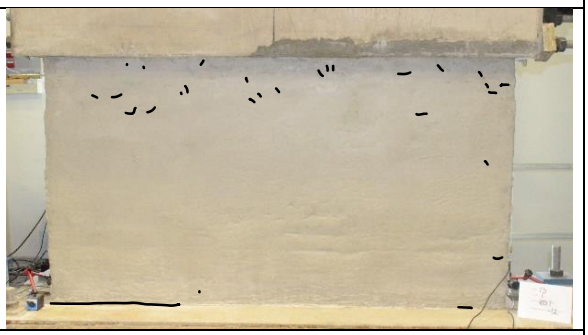

<table>
<tr><td></td><td> 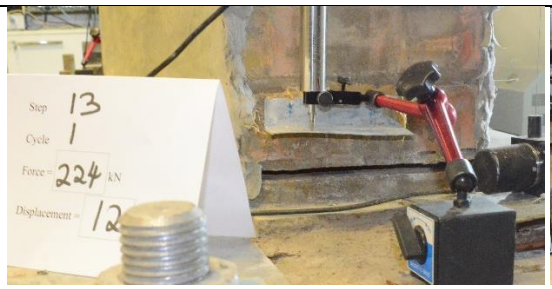

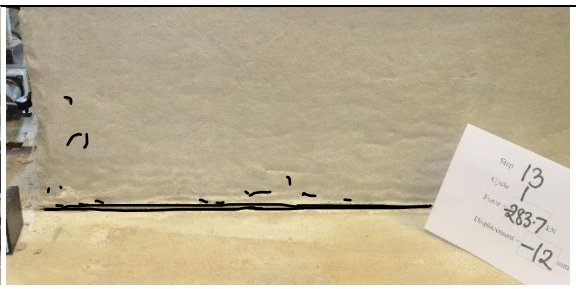
</td></tr>
<tr><td>Force:
257.50kN

Drift:
1.18%</td><td> 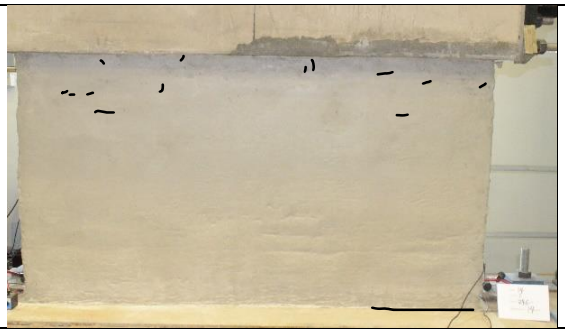
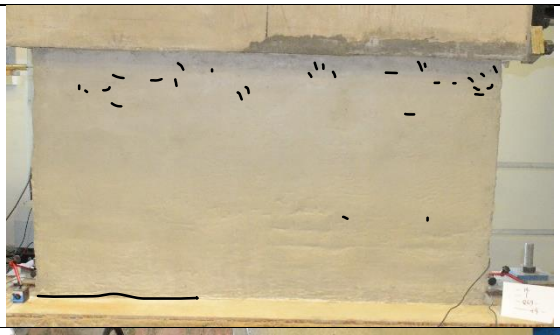
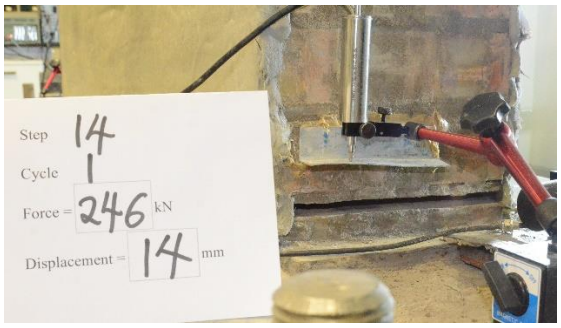

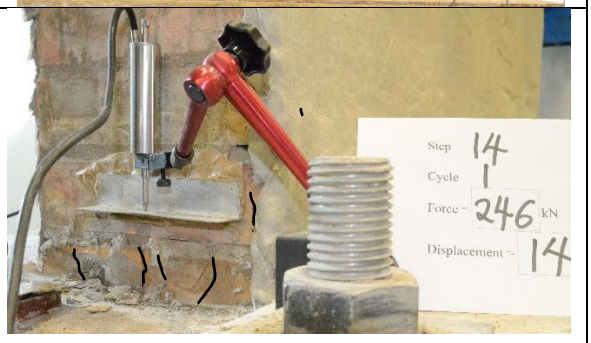
</td></tr>
<tr><td>Force:
232.15 kN

Drift:
1.34%</td><td>
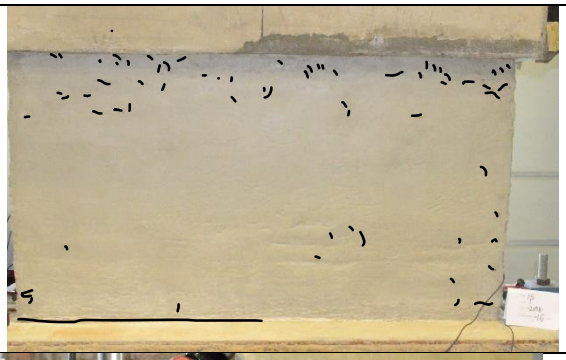

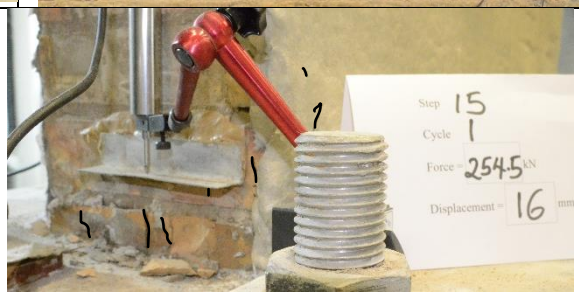
</td></tr>
</table>

Force:
249.50 kN

Drift:
1.51%

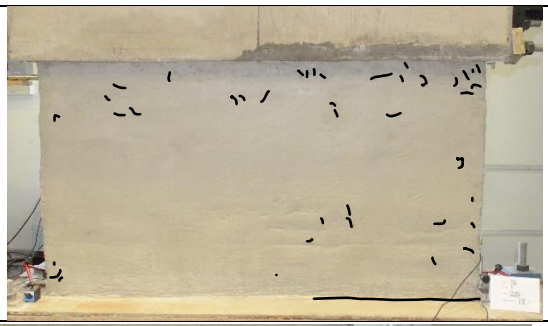
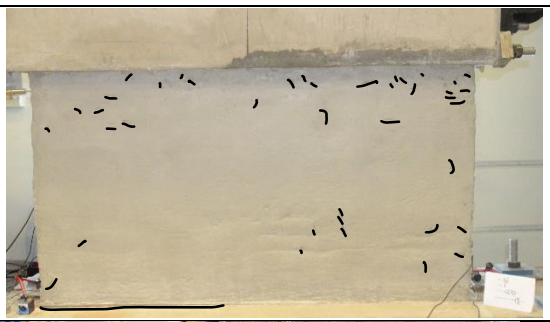
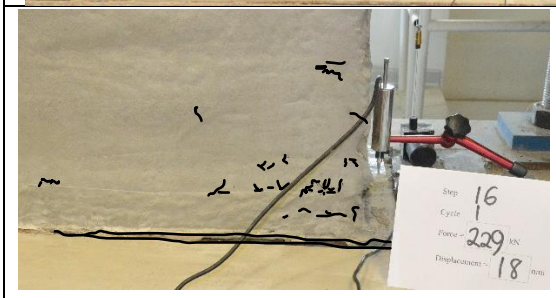

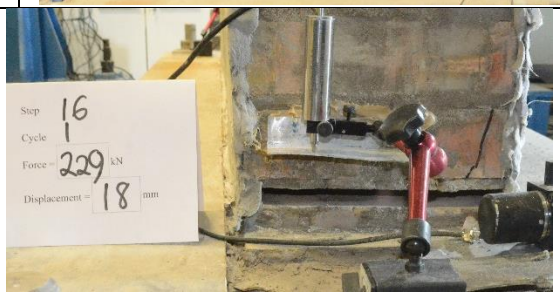

Force:
227.50 kN

Drift:
1.68%

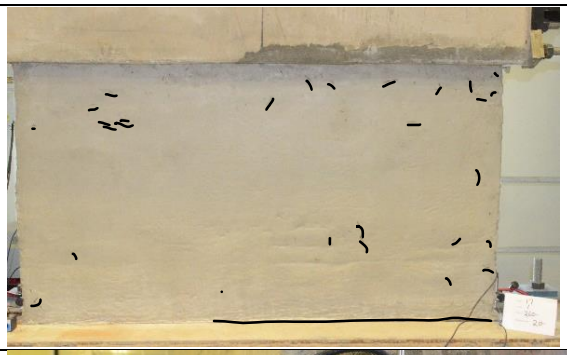
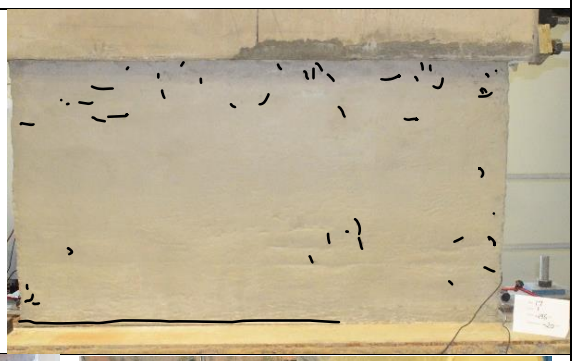

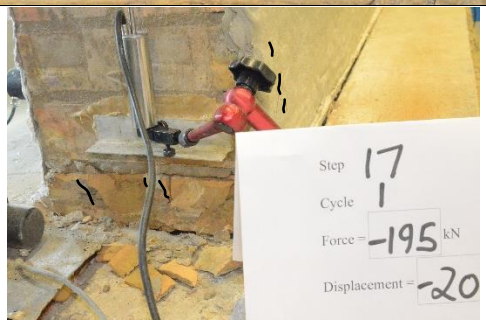

Force:
+214.8kN

Drift:
1.85%

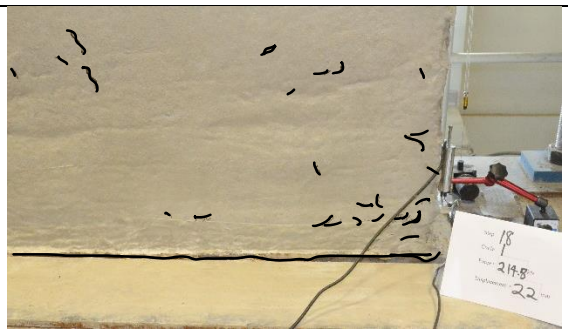

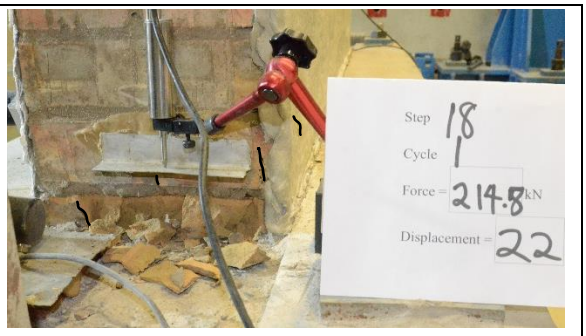
Step 18
Cycle 1
Force = 214.8 kN
Displacement = 22

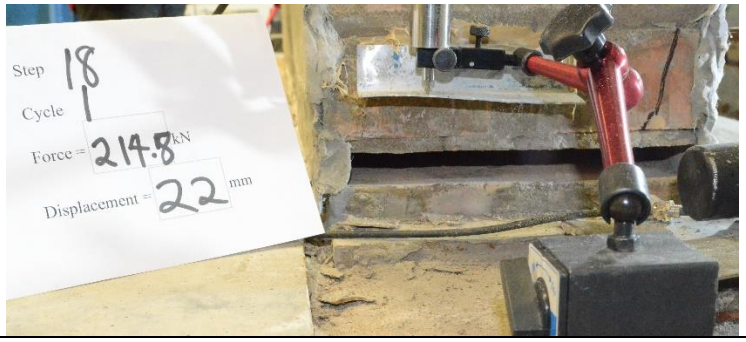
Step 18
Cycle 1
Force = 214.8 kN
Displacement = 22 mm